Long-time evolution of core-collapse supernovae

Witt, Maximilian Rudolf

(2020)

Long-time evolution of core-collapse supernovae

Langzeitentwicklung von Kernkollapssupernovae
Zur Erlangung des Grades eines Doktors der Naturwissenschaften (Dr. rer. nat.)
genehmigte Dissertation im Fachbereich Physik von Maximilian Rudolf Witt aus Regensburg
Tag der Einreichung: 08.04.2020, Tag der Prüfung: 15.06.2020
Darmstadt – D17

1. Gutachten: Prof. Dr. Almudena Arcones Segovia
2. Gutachten: Priv.-Doz. Dr. Michael Buballa

TECHNISCHE UNIVERSITÄT DARMSTADT

Fachbereich Physik
Institut für Kernphysik
Theoretische Astrophysik

Long-time evolution of core-collapse supernovae
Langzeitentwicklung von Kernkollapssupernovae

genehmigte Dissertation im Fachbereich Physik von Maximilian Rudolf Witt

1. Gutachten: Prof. Dr. Almudena Arcones Segovia
2. Gutachten: Priv.-Doz. Dr. Michael Buballa

Tag der Einreichung: 08.04.2020
Tag der Prüfung: 15.06.2020

Darmstadt – D17

Tomorrow massive stars will explode
In the heart of galaxies
Millions and millions of suns
In command of the constellation

Across the core
A vast spiral galaxy
Burning lights
Nothing can ever escape

Towers of black ash
Rip to shreds
Lost in the void
Upon the event horizon

Observe its effects from afar
As the cloud collapses
Outpouring from its core
Evolution and Fate

Sarke - Evolution and Fate

Abstract

The puzzle of core-collapse supernovae (CCSN) remains complicated. New insights from theory and observations bring the pieces together, but we still have to witness the complete picture. Simulations of CCSN are key to understand the mechanisms that drive the explosion. While the explosion itself is nowadays studied in great detail, the long-time evolution has received less attention in studies. This is partly because of the high computational costs for comprehensive long-time simulations. However, the seconds after the initial explosion are nevertheless critical for remnant and ejecta properties, as well as for the nucleosynthesis in a CCSN. In this study, we investigate the influence of neutrino heating and rotation on both the explosion and long-time evolution. We perform axisymmetric CCSN simulations and use adjustable parameters that allow us to study a broad range of possible scenarios. Our results suggest that increased neutrino heating is beneficial for the explosion, which is consistent with previous studies. On the other hand, rotation can be detrimental to it. In the long-time evolution, rotation reduces the mass accretion onto the proto-neutron star and creates favorable conditions for the formation of neutrino-driven winds. We furthermore investigate the trajectories of ejected fluid elements by developing a tracer particle scheme. This scheme allows for a comprehensive study of ejecta properties and an estimation of the nucleosynthesis in CCSN simulations. We test the robustness of our main results with simulations of different progenitor stars. Overall, we conclude that the long-time evolution in CCSN is important for the final explosion energy, remnant and ejecta properties.

Cover picture: Supernova artist's rendition [1]

Zusammenfassung

Das Rätsel der Kernkollapssupernovae (CCSN) bleibt kompliziert. Neue Erkenntnisse aus der Theorie und von Beobachtungen setzen die Puzzleteile zusammen, aber das fertige Bild bleibt noch unvollständig. Simulationen von CCSN sind ein Schlüsselfaktor für das Verständnis der Mechanismen, die die Explosion antreiben. Während die Explosion selbst heute sehr detailliert studiert wird, erhält die Langzeitentwicklung weniger Beachtung in Studien. Dies liegt unter anderem am hohen Rechenaufwand für umfangreiche Langzeitsimulationen. Die ersten Sekunden nach der Explosion sind dennoch entscheidend für die Überreste, die ejektierte Materie, sowie für die Nukleosynthese in der CCSN. In dieser Studie untersuchen wir den Einfluss des Neutrinoheizens und der Rotation auf die Explosion und die Langzeitentwicklung. Wir führen rotationssymmetrische CCSN-Simulationen durch und verwenden variable Parameter, mit denen wir ein breites Spektrum möglicher Szenarien untersuchen. Unsere Ergebnisse legen nahe, dass ein erhöhtes Neutrinoheizen vorteilhaft für die Explosion ist, wie es auch bereits in früheren Studien festgestellt wurde. Auf der anderen Seite kann sich die Rotation nachteilig auf sie auswirken. In der langfristigen Entwicklung reduziert Rotation die Massenakkretion auf den Proto-Neutronenstern und schafft günstige Bedingungen für die Bildung neutrinogetriebener Winde. Des Weiteren untersuchen wir die Trajektorien ejektierter Fluidelemente mit einem eigenen Tracerpartikelverfahren. Dieses Verfahren ermöglicht eine umfassende Untersuchung der Eigenschaften ejektierter Materie und eine Abschätzung der Nukleosynthese in CCSN-Simulationen. Wir testen die Robustheit unserer Hauptergebnisse mit Simulationen verschiedener Vorgängersterne. Insgesamt kommen wir zu dem Schluss, dass die Langzeitentwicklung in CCSN wichtig ist für die endgültige Explosionsenergie, sowie für die Eigenschaften der Überreste und der ejektierten Materie.

Contents

1. Introduction

The stars in the night sky have always had an immeasurable impact on humankind and civilizations. Careful observations of the firmament allow us to locate our position in both space and time. Technologies like the calendar and naval navigation originally depended on this information, and made further advancements of humankind possible. With the observation of the stars, supernovae have already been noticed in ancient times. They can be one of the night sky's brightest objects for a brief amount of time, which appears to the naked eye as a new star ("nova"). The oldest records of observed supernovae date back to Chinese astronomers in the year 185, while later events were also recorded by Oriental and European observers [2]. Tycho Brahe with his observation of SN 1572 was the first to show that these events happen far away from earth in the realm of the fixed stars, instead of being atmospheric phenomena of our planet. The Aristotelian world view, in which the fixed stars never change, was challenged by Johannes Kepler. Observations of SN 1604 led him to the conclusion that even the eternal stars are not as eternal after all.

For the subclass of core-collapse supernovae (CCSN), research also begins with their observations. As luminous objects that are clearly visible in the night sky for several months, astronomers around the world have recorded these events for a long time. The oldest recorded supernova that we can nowadays attribute to the class of Type II supernovae is SN 1054, leaving behind the Crab Nebular and the Pulsar PSR B0531+21 (see Fig. 1.1). Other notable historic CCSN include the supernova of Cas A, which occured around the year 1681 and was unfortunately not recorded by humans [3]. More recently, SN 1987A provided exceptional details with the observation of several telescopes and the detection of neutrinos on earth [4].

The idea that CCSN leave a neutron star behind dates back to Baade & Zwicky (1934) [6], who also introduced the term "Super-Nova". This was only shortly after the discovery of the neutron by Chadwick in 1932 [7]. With the study of Burbidge et al. (1957) [8] began the discussion about the origin of heavy elements, where CCSN instantly became a candidate for the astrophysical site of heavy-element formation. The first attempts to

Figure 1.1.: Combined X-ray (blue) and optical (red) image of the Crab Nebular with its Pulsar (red star in the center). Picture taken from Ref. [5].

simulate the core-collapse mechanism date back to Colgate & White (1966) [9]. They were the first to introduce hydrodynamic simulations as tools to study the collapse and explosion of a heavy star. Since then and with the help of modern computers, the efforts to accurately simulate the CCSN mechanism have improved greatly.

Theoretical considerations about the nature of stars and their deaths also lead to the cosmic origin of the elements. Stars can only resist gravitational collapse by generating energy through nuclear fusion processes [10]. This mechanism is also responsible for their brightness and high temperature spectra, which was first described by Arthur Stanley Eddington in 1920 [11]. The temperatures in the cores of massive stars are extreme enough to fusion elements up to iron [12]. Synthesis of heavier elements requires a different scenario, since iron and nickel have the highest nuclear binding energy per nucleon [13]. They are therefore a natural barrier to energy gains from fusion processes. A mechanism to form elements heavier than iron was proposed in the famous $\mathrm{B^2FH}$ paper by Burbidge et al. in 1957 [8]. Specifically, they proposed neutron capture processes on lighter elements as a way to go up the nuclear chart. The two main processes for this, the s- and the r-process, work on different timescales and require different environments. While the astrophysical site for the slower and less extreme s-process has been identified to be asymptotic giant branch stars [14], the site of the more extreme r-process, which is thought to form the heaviest elements in the universe [15], is still under investi-

gation. Originally, supernovae and neutrino-driven winds were the favourite candidate. However, advanced simulations in the recent decades agree that the conditions are likely not extreme enough for heavy-element formation [16]. Only rapidly rotating, strongly magnetized supernovae can have favorable conditions for r-process nucleosynthesis [17]. Instead, neutron star mergers with their heavily neutron-rich environments are nowadays considered to be the main r-process site. Supernovae still remain an important site for the nucleosynthesis of the so-called lighter heavy elements [16].

The research on supernovae and the nucleosynthesis therein combines physics from a broad variety of different topics. Most obviously, astronomy supplies observational data like light curves [18], neutrino emission [19], ejecta [10], and remnant information [12]. In the near future, multimessenger astronomy with gravitational wave detection may provide additional data [20]. The input from nuclear physics is present at all stages of the explosion, prominently for determining the equation of state at high densities [21], and nuclear reaction rates for nucleosynthesis [22]. Weak interaction processes [23] and neutrino physics [24] have been determined to be crucial for an accurate model of stars and stellar explosions. Simulations of supernovae also require detailed knowledge of hydrodynamic flows and shock propagation. Finally, CCSN leave behind neutron stars and black holes [12], which are the most compact objects in our universe and can only be accurately described with general relativity.

There remain many open questions regarding the mechanism of CCSN. The combined efforts of theory, experiment and observations have brought new insights on the matter. In the recent decades, the onset of sophisticated numerical simulations allowed to study different possibilities for the CCSN mechanism [25, 26]. Furthermore, the impact of individual contributions (e.g., neutrinos [27, 28], magnetic fields [29, 30], turbulence [31]) to this scenario can be quantified and constraints for ejecta [32] and remnant properties [33, 34] can be given. The comparison of these constraints to observational data serves as a back-check for the input physics to simulations and hints to missing links in the supernova puzzle.

The explosion usually sets in within the first second after collapse, and the majority of studies focuses on that time. The long-time evolution, i.e., the subsequent seconds, has received less attention [35]. However, reliable estimates of the nucleosynthesis in a CCSN, the final explosion energy, and remnant properties, require long-time simulations. This comes with increased computational costs, and long-time simulations of current state-of-the-art setups are not feasible yet [36]. Not only does the calculation take longer, but it also requires a larger domain size to follow the fast expanding ejecta. Additionally, a

broader range of the physical quantities needs to be considered, since the larger computational domain includes the outer layers of a progenitor star, where comparably small densities and temperatures are present [37]. Individual simulations can be extended to longer times with the help of simplifications [38, 39], but large-scale studies are yet to be performed.

Here, we aim a investigate the first several seconds of a CCSN in a variety of different scenarios. We use a simplified setup in a two-dimensional domain and vary the neutrino heating and rotation strength with parameters. The shock evolution and ejecta properties are followed for up to ten seconds. While this has been performed in a spherically symmetric geometry (e.g., see Ref. [40]), there are almost no long-time studies with multi-dimensional simulations. However, capturing the multi-dimensional character of CCSN is important for the nucleosynthesis, as it allows for convection, simultaneous presence of accretion and ejection, and large scale mixing of matter. Furthermore, the formation of neutrino-driven winds and the evolution of the proto-neutron star mass and explosion energy critically depends on multi-dimensional effects [41]. We provide a detailed study of long-time effects in multi-dimensional CCSN simulations, and investigate the impact of the first seconds after shock revival on the explosion energy, remnant, and ejecta properties.

This work starts with a CCSN theory overview in chapter 2, and a discussion of our methodological setup in chapter 3. We consider modifications to the neutrino heating mechanism and study their effect in chapter 4. The impact of rotation on the supernova explosion and long-time evolution is considered in chapter 5. We develop a tracer particle method for our simulations that allows us to estimate ejecta properties and nucleosynthesis yields (chapter 6). Finally, we test the robustness of our results by comparing supernovae from different progenitor stars, in chapter 7. We give a summary of our study and an outlook for future investigations in chapter 8.

2. Theoretical background

2.1. Core-collapse supernovae

Core-collapse supernovae (CCSN) mark the end of the lives of massive stars. They are one of the most energetic events in our universe and the birth site of neutron stars. The enormous explosions eject large amounts of matter into the interstellar medium. Additionally, they are a possible site for heavy-element formation.

The exact nature of the explosion mechanism is still under debate. Progress has been made with the help of modern, state-of-the-art simulations of CCSN, but many problems are still unsolved.

In this chapter, we cover the general features of a core-collapse supernova, starting with a short summary of stellar evolution and then explaining the explosion mechanism in detail. Furthermore, we give an overview of the general methods for long-time simulations of CCSN. We follow the references [10, 12, 25, 36, 42, 43].

2.1.1. Stellar evolution

During their lifetime, stars undergo a series of nuclear fusion processes. The energy generated by fusion is necessary to stabilize the star against gravitational collapse. The burning phases in young stars start with the fusion of hydrogen and helium. In massive stars, the main process involved in this is the CNO-cycle. The center of the star accumulates helium and contracts as a consequence of the increased graviational potential. When the temperature in the helium core is sufficiently high, the triple-alpha process begins to convert helium to carbon. Further burning stages only appear in massive stars with more than eight solar masses ($M \gtrsim 8\ M_\odot$) and include neon, oxygen, and silicon, until the star is left with a core consisting of iron-group nuclei (see Fig. 2.1). As iron has

the highest binding energy per nucleon of all elements, no further energy can be generated by nuclear fusion, and the core is instead stabilized by electron degeneracy pressure, similar to a white dwarf.

Stage	Timescale	Fuel or product	Ash or product	Temperature (10^9 K)	Density (gm cm^{-3})	Luminosity (solar units)	Neutrino losses (solar units)
Hydrogen	11 Myr	H	He	0.035	5.8	28,000	1,800
Helium	2.0 Myr	He	C, O	0.18	1,390	44,000	1,900
Carbon	2000 yr	C	Ne, Mg	0.81	2.8×10^5	72,000	3.7×10^5
Neon	0.7 yr	Ne	O, Mg	1.6	1.2×10^7	75,000	1.4×10^8
Oxygen	2.6 yr	O, Mg	Si, S, Ar, Ca	1.9	8.8×10^6	75,000	9.1×10^8
Silicon	18 d	Si, S, Ar, Ca	Fe, Ni, Cr, Ti, ...	3.3	4.8×10^7	75,000	1.3×10^{11}
Iron core collapse*	~1 s	Fe, Ni, Cr, Ti, ...	Neutron star	>7.1	$>7.3\times10^9$	75,000	$>3.6\times10^{15}$

* The pre-supernova star is defined by the time at which the contraction speed anywhere in the iron core reaches 1,000 km s^{-1}.

Figure 2.1.: Burning stages of a $15\ M_\odot$ star. Taken from Ref. [42].

After only a few days of silicon burning, the mass of the iron-core approaches the Chandrasekhar limit of $\sim 1.4\ M_\odot$. As a consequence, the temperatures in the center increase until thermal photons can disintegrate the heavy nuclei back into helium and free nucleons. This lowers the adiabatic index of the matter, leading to a contraction of the core. Eventually, electron-capture on protons sets in and deleptonizes the center of the star, which accelerates the contraction even more because of the reduced degeneracy pressure. The core collapses under its gravitational force at the timescale of a second.

2.1.2. Collapse and bounce

When the densities exceed $10^{12}\ \mathrm{g/cm^3}$, neutrinos become trapped in the core, as the free-fall timescale becomes comparable to their diffusion timescale. Unlike in the innermost part where the density is high, they can diffuse out at the core's outer parts at lower density, and eventually stream away freely from the neutrinosphere at $\rho \approx 10^{11}\ \mathrm{g/cm^3}$. The exact location of the neutrinosphere depends on the flavor and energy of each neutrino and varies within a few kilometers. Collapse stops when the densities reach the nuclear saturation density of $\rho_0 \approx 2.7 \cdot 10^{14}\ \mathrm{g/cm^3}$, where a phase transition to homogeneous nuclear matter stiffens the equation of state. The nucleon gas is highly incompressible because of the repulsive part of the nucleon-nucleon interaction potential at small distances. Further infalling matter eventually bounces back from the stiffened core, creating

pressure waves that accumulate to an outwards moving shock front (Fig. 2.2). The electron fraction in the center, which is the amount of electrons per baryon, has decreased to values of $Y_e \approx 0.25$ as a result of the neutrino losses during collapse. At the point of bounce, the innermost $0.5\ M_\odot$ contribute to the center that will evolve into a proto-neutron star (PNS). Further accretion of matter through the shock will increase its mass over time with a rate depending on the amount of accretion.

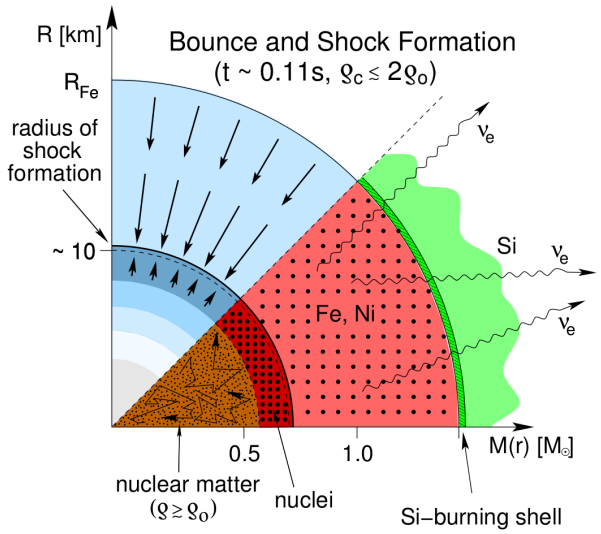

Figure 2.2.: Schematic picture of bounce and shock formation. Taken from Ref. [43].

As the shock propagates outwards, it loses energy by photo-dissociation of iron-group nuclei and neutrino emission. Furthermore, the continued infall of matter from the outer layers acts against the shock expansion. The density behind the shock decreases with growing radius. The reduced densities allow the aforementioned trapped neutrinos to suddenly escape, resulting in the so-called neutrino burst, a luminous event with peak neutrino luminosities of over 10^{53} erg/s. After only a few millisecond and having expanded to roughly 100 km radius, the shock has lost all its kinetic energy and stalls. The mechanism that revives the shock and ultimately leads to a successful explosion, has been the main topic of debate in supernova research for decades now. Several different possibilities, including the aid of magnetic fields, may explain the shock revival. In the following, we focus on the neutrino heating mechanism that we use in this work, which is a current favorite among modern simulations.

2.1.3. Shock revival and explosion

While the stalled shock stays at around 100 km radius, the PNS accretes matter and contracts under its gravitational force. The gravitational energy of a homogeneous sphere with mass M and radius R can be estimated according to Newton's law:

$$E_{\mathrm{grav}} = -\frac{3}{5}\frac{GM^2}{R} \approx -3.1 \cdot 10^{53}\ \mathrm{erg} \left(\frac{M}{1.4\ M_\odot}\right)^2 \left(\frac{R}{10\ \mathrm{km}}\right)^{-1}, \tag{2.1}$$

where G is the gravitational constant. For an iron core ($M = 1.4\ M_\odot$) with an initial radius of $R = 2000$ km that contracts to a PNS of only $R = 30$ km, this results in an energy release of about $10^{53}\ \mathrm{erg} \equiv 100\ \mathrm{B}$. This energy is converted into internal energy of electrons, nucleons and the trapped neutrinos. The energetic neutrinos escape at the neutrinosphere, which leads to an effective cooling of the PNS. With further contraction, the neutrino spectra harden as the neutrinosphere moves inwards to higher temperatures. The amount of neutrinos streaming away from the neutrinosphere as well as their energy increases.

The luminosity L_ν of electron neutrinos (ν_e) and electron antineutrinos ($\bar{\nu}_\mathrm{e}$) can be separated into two contributions. Thermal processes within the hot PNS produce neutrinos that stream away from the neutrinosphere. Additionally, matter accreted through the shock onto the PNS is heated to high temperatures and also radiates neutrinos. This results in an increased luminosity whenever mass accretion is high. The two contributions are called thermal (or diffusion) luminosity and accretion luminosity, respectively.

The neutrinos diffuse through the low-density layer between the neutrinosphere and the shock. A fraction of them eventually interacts with matter right behind the shock. The interaction of neutrinos with matter leads to a net positive energy deposition there. The most important heating processes are the charged-current reactions,

$$\nu_\mathrm{e} + n \longrightarrow p + e^-, \tag{2.2}$$

$$\bar{\nu}_\mathrm{e} + p \longrightarrow n + e^+ . \tag{2.3}$$

The small cross-sections of neutrino interactions with matter have an impact on the efficiency of the neutrino heating mechanism. Of the total 100 B released in gravitational energy, typically only about 1 B contributes to the actual explosion. Heated matter forms plumes and bubbles that move away from the gravitional pull of the PNS, just like bubbles of boiling water flee earth's gravitational field within a pot. Rayleigh-Taylor instabilities

create typical structures that resemble mushroom clouds. Multi-dimensional simulations have shown that standing accretion shock instabilities (SASI) can appear [44], which can enhance convective instabilities and expand the shock radius [45]. Meanwhile, the PNS accretes matter through its high gravitational potential. In the vicininty of the PNS, this matter experiences a higher neutrino flux, which drives a fraction of it outwards again. This boiling cycle increases the entropy behind the shock in the so-called gain layer, where the net neutrino energy deposition is positive (Fig. 2.3). Eventually, this leads to the revival of the shock, and ultimately to a successful explosion.

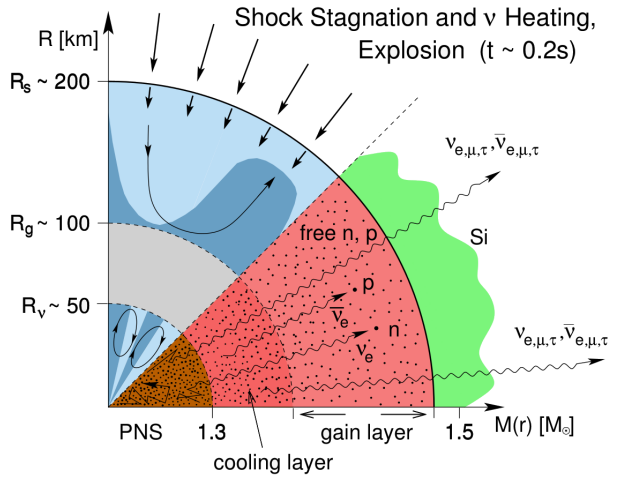

Figure 2.3.: Schematic picture of shock stalling and neutrino heating below the shock front. Taken from Ref. [43].

As the explosion sets in, the shock accelerates up to a few 10^9 cm/s or several percent of the speed of light in vacuum. Considering the multi-dimensionality of the problem, it is possible that it expands not isotropically but in a preferred direction, while accretion from another direction is still present. This can lead to a situation where cold matter is constantly accreted towards the PNS, heated and then expelled into the direction of explosion. Asymmetries between accretion and ejection do not only power the supernova engine and increase the total energy of the explosion, but can also lead to PNS kicks via the so-called tug-boat mechanism [46].

The expanding shock cools down from several 10 GK to under 1 GK ($\equiv 10^9$ K) within a few seconds. Heavy elements can form in the cooling ejecta. The nucleosynthesis outcome can be estimated with the electron fraction of matter, its entropy, and the timescale on

which the matter temperature decreases. Under the typical conditions of the shocked ejecta with comparably slow cooling, the nucleosynthesis is limited to intermediate-mass nuclei and radioactive iron-group elements.

2.1.4. Neutrino-driven winds

Seconds after a successful explosion, the density in-between the PNS and the shock wave decreases, as matter is either accreted onto the PNS or driven outwards with the explosion. Simultaneously, the PNS keeps on contracting and cooling under the ejection of neutrinos. Eventually the density just above the PNS becomes so small that matter can be accelerated to supersonic velocities by neutrino heating. In the absence of accretion, even parts of the PNS surface are blown off, resulting in a (slightly) decreasing PNS mass at late times. The accelerated matter forms a laminar outflow, a so-called neutrino-driven wind (NDW), which can last for several seconds (see Fig. 2.4). The phenomenon was first described by Duncan et al. (1986) [47] and received attention particularly for its possibility to be a site of the astrophysical r-process [48–51]. However, with the advent of sophisticated long-time simulations of CCSN, it became evident that the conditions for r-process nucleosynthesis are not sufficiently extreme in a NDW, but are rather only favorable for the formation of lighter heavy elements up to Argon [16, 40, 52–54].

The NDW is a laminar outflow that has similar properties over a period of several seconds. This suggests that it can be described analytically with a steady-state approach, as performed by Qian & Woosley (1996) [49] and Otsuki et al. (2000) [55]. A steady-state description is a powerful tool that is still relevant for recent parametric studies. For example, it allows to investigate the impact of astrophysical and nuclear physics uncertainties on NDW nucleosynthesis (e.g., see Ref. [56, 57]). Although a steady-state treatment approximates the evolution of density, temperature and entropy as a function of the radius, it lacks the inclusion of hydrodynamic effects such as the wind termination shock [16].

Simulations of CCSN have featured NDWs for a long time, for example in Ref. [48]. One-dimensional simulations can either have accretion or ejection of matter from the PNS, but not both at the same time. As a consequence, neutrino-driven outflows from the PNS are generally present after a successful explosion [40]. In two dimensions like performed in this study, the situation is different. Accretion and ejection can exist at the same time, in different directions. Because of turbulent motions of the PNS, outflows in one direction are usually influenced by the simultaneous accretion, and therefore also consist of matter that does not originate from the PNS, in contrast to the wind ejecta.

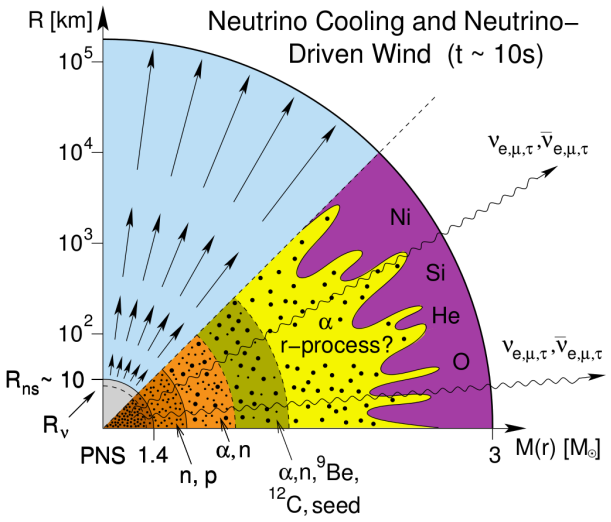

Figure 2.4.: Schematic picture of the neutrino-driven wind and nucleosynthesis therein. Taken from Ref. [43].

In this study, we use the mass accretion rate as the quantity to determine whether a NDW is present. We evaluate the mass accretion through a sphere around the PNS with a radius of 500 km, which is given by

$$\dot{M}_{\mathrm{acc,500km}} = 4\pi \int_{-\pi/2}^{\pi/2} \left(r^2\, \rho(r,\theta)\, |\min(v_{\mathrm{rad}}(r,\theta),0)|\right)_{r=500\mathrm{km}} \mathrm{d}\theta\ , \tag{2.4}$$

where $|\min(v_{\mathrm{rad}}(r,\theta),0)|$ is the radial component of inflowing matter only. Typical maximum values of $\dot{M}_{\mathrm{acc,500km}}$ are of the order of $10\ M_\odot$/s during collapse. After shock revival, the mass accretion rate decreases by several order of magnitude. The simulation features an isotropic NDW when $\dot{M}_{\mathrm{acc,500km}} = 0$, i.e., when there is only ejection and no accretion in all directions.

2.1.5. Remnants

The two main possible outcomes of CCSN are neutron stars and black holes. While neutron stars are born in successful explosions exclusively, black holes can form in a variety of scenarios. If the shock is not revived successfully, continued accretion pushes the PNS

over its mass limit, which results in a prompt black hole formation that produces no detectable electromagnetic signal. In the case of successful shock revival, it is still possible that continued accretion behind the shock front leads to a collapse of the PNS and creates a so-called fallback black hole. Finally, nuclear phase transitions, loss of pressure support through cooling or decelaration of a hypermassive, rotating PNS can also lead to a delayed black hole formation, which can be detectable [58].

One of the main goals of CCSN research is to find a simple criterion, by which a progenitor star will result in either a neutron star or a black hole. Several criteria based on the compactness of the progenitor [59, 60] or its entropy profile [61] seem to be rather successful in predicting the fate of progenitors in simulations. However, simplified analytical models of the CCSN mechanism suggest that a simple one- or two-parameter criterion is not sufficient to accurately predict the fate of a star [62]. Results of these studies include a characteristic gap in the explodability of progenitors within the mass range of $21 \lesssim \mathrm{M} \lesssim 25\ M_{\odot}$, where dominantly black holes are formed.

2.2. Long-time simulations of core-collapse supernovae

In this section, we briefly describe methods and goals of long-time simulations of CCSN. The term "long-time" usually defines simulations that do not only investigate the shock revival mechanism, but also follow the evolution afterwards for several seconds. Main goals of these studies include the investigation of the nucleosynthesis in a CCSN, as well as providing predictions for the final remnant properties and observables, such as light curves. We focus on possibilities to achieve (artificial) shock revival and the necessary ingredients to follow the shock evolution.

2.2.1. Explosion methods

Long-time simulations intend to follow the shock after its revival. However, many models fail to explode self-consistently, which is most apparent in spherically symmetric simulations, with the exception of low-mass progenitor models [52, 53, 63]. The lack of successful shock revival in simulations even led to the question if the neutrino heating mechanism is fundamentally flawed [64]. In the recent years, progress in the accurate modeling of the CCSN physics led to explosions in multi-dimensional simulations, although not all models show successful shock revival [26]. It therefore became necessary to artificially trigger explosions, where otherwise none would be achieved.

Early attempts to solve this issue include the use of a piston [65], which is placed at a given mass shell of the progenitor and then accelerated inwards. The position and kinetic energy of the piston are free parameters that can be tweaked to achieve a given explosion energy and ejecta mass. Another method is the use of a thermal energy bomb [66, 67] that injects a specified amount of energy in a given progenitor region. Typical values that are used to calibrate these models include an explosion energy of 1.2 B and an ejected nickel mass of $0.1\ M_{\odot}$.

Another, more recent method to facilitate artificial explosions is the PUSH method for spherically symmetric models [68]. This method uses the convenience that heavy-lepton neutrinos (i.e., muon and tau neutrinos and antineutrinos) do not directly affect the electron fraction, as electron neutrinos and antineutrinos do. They can therefore be used as an artificially parametric energy source by depositing a fraction of their luminosity as energy in the gain region. The additional heating is deposited in regions where the electron neutrino net heating rate is positive, and where neutrino-driven convection can occur. Furthermore, it is only deposited during a specific amount of time in the first second after bounce. The exact amount and duration of the energy deposition is set by a calibration against observed properties of the supernova SN 1987A. These properties include an explosion energy of 1.1 ± 0.3 B and yields for the ejecta masses of nickel and titanium isotopes. PUSH has been used for a number of studies investigating the explodability of progenitors, remnant properties and nucleosynthesis yields [33, 34, 68, 69].

In this study, we adopt a method that also achieves explosions by altering the efficiency of the neutrino heating mechanism. Specifically, O'Connor & Ott (2010) [70] introduced a heating factor f_{heat} that is multiplied to the neutrino heating rate and allows for an ad-hoc increase of the energy deposition. Because the heating strength of neutrinos determines the evolution of the explosion, this additional factor also influences the explosion energy. The idea was later adopted by Couch & O'Connor (2014) [71] for multi-dimensional simulations with the FLASH code [72, 73], that we use in this study. The heating factor also allows for a quantitative analysis about how much additional neutrino heating is necessary to obtain shock revival. In the study in Ref. [71], it was found that the same progenitor star needs $40 - 45\%$ more neutrino heating for an explosion when calculated in 1D, but only 5% more in 3D. In 2D, even models without additional heating can explode. However, the exact values also depend on the details of the simulation and the cross-sections of neutrino interactions with matter in the gain region. We will present modifications in the heating factor implementation and investigate its impact on the simulation in chapter 4.

2.2.2. Following the shock evolution

Calculating nucleosynthesis yields in the long-time evolution of CCSN requires an accurate and efficient tracking of the shock evolution. An obvious necessity is a simulation domain that is large enough to include the shock front at all times. Observations of SN 1987A inferred ejecta velocities of $\gtrsim 7000$ km/s before colliding with its ring of circumstellar matter [74], and it is sensible to assume even higher velocities in the first seconds after shock revival. Long-time simulations that aim to follow the evolution for several seconds must therefore cover a domain size of several ten- or hundred-thousand kilometers.

The large simulation domain comes with the cost of increased computational resources. It is not trivial to provide a sufficient spatial resolution to capture the comparably small PNS (and potentially its changing position in a multi-dimensional simulation), while still covering the total amount of ejected matter seconds after shock revival. In multi-dimensional simulations, this can be achieved with a variable grid layout. The computational grid in a CCSN simulation typically consists of individual calculation blocks and cells. These can be of different size and change during the course of a simulation. In FLASH, this is realized with the implementation of the PARAMESH toolkit [75].

Another peculiarity of long-time simulations, that results from the increased domain size, is the large range of quantities like the matter density. A single CCSN simulation can have physical conditions spanning across many orders of magnitude, which requires a careful numerical treatment. Figure 2.5 shows the experienced conditions in a typical CCSN simulation. The color indicates at which time relative to bounce the condition was realized. The matter density spreads over a total of 14 orders of magnitude, from ordinary matter up to the high-density regime where effects from nuclear physics have to be taken into account. Extending the domain size also means an extension to even lower densities and temperatures, which are present in the outer layers of the progenitor star.

2.3. Current status of simulations

Simulations of CCSN have progressed greatly in the recent decades and years. While parts of the underlying physics are well-known (hydrodynamics, gravity, ...), there is still research to be done on other fields, especially the microphysics input (neutrinos, equation of state, ...). Additionally, the implementation into numerical treatment is a different

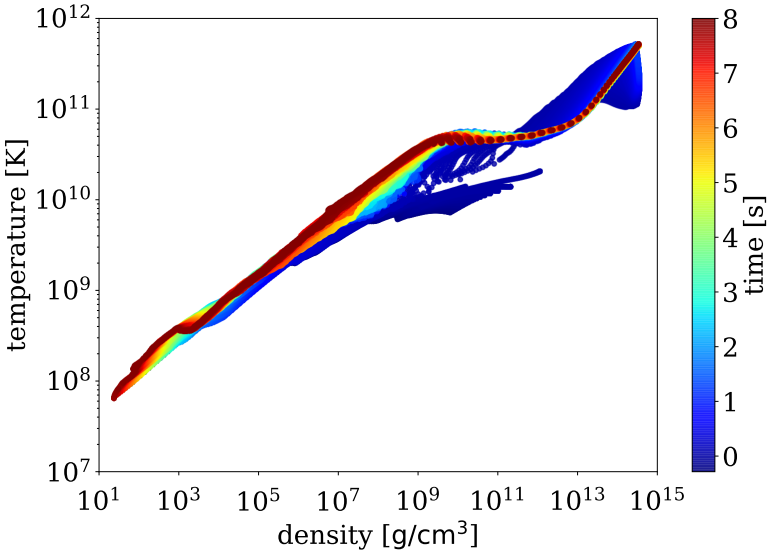

Figure 2.5.: Densities and temperatures over the course of a long-time CCSN simulation. The color indicates the time at which the conditions are realized.

challenge, accompanied by numerical uncertainties and limitations in the computational resources.

It has become evident that a reduced dimensionality misses important physics that can be crucial for the explosion mechanism [26]. However, full 3D simulations with an acceptable grid resolution and input physics are computationally expensive and usually only cover the explosion phase (e.g., see Ref. [76, 77] for some recent simulations of low-mass progenitors that cover the first 1-2 seconds after bounce). Results from a recent study by Nagakura et al. (2019) [78] suggest that the grid resolution might play an equally important role as the dimensionality when determining the explodability of a star.

Regarding the microphysics, efforts have been made to constrain uncertainties and understand their influence on the CCSN mechanism. For example, the influence of various parameters of the nuclear EOS is investigated in Ref. [79, 80]. Important neutrino physics concerning cross-sections and opacities (e.g., Ref. [27, 81]) and the effect of neutrino oscillations [82] are considered.

A recent focus has also been laid on multi-dimensional progenitors, as opposed to the mostly used 1D stellar evolution models. The multi-dimensionality of progenitors and

turbulence effects can have a relevant impact on the explosion behavior (e.g., see Ref. [31, 83–85]. These recent studies suggest that angular-dependent perturbations in the progenitor profile can aid a successful explosion, reducing the necessary neutrino luminosity by up to 20%.

In the case of long-time simulations, efforts have been made to follow the ejecta for a long time to compare with observations. Some recent simulations follow the evolution up to the point of shock breakout, where the ejecta reach the interstellar medium outside of the star, at the timescale of hours and days after bounce [38, 39]. Numerical techniques to achieve such long simulation times include the mapping of the whole simulation state some seconds after shock revival to another code with more simplified physics, such as Newtonian gravity, and neglecting neutrinos. The innermost, high-density part surrounding the PNS is usually cut out and replaced by a boundary criterion, which reduces the computational costs greatly.

3. Simulation methods

Hydrodynamic simulations have proven to be an important tool for core-collapse supernova (CCSN) research. The first simulations of CCSN date back to the 1960s, when techniques from numerical hydrodynamics were introduced to simulate the explosion of a star [9, 86, 87]. These early attempts were performed in a spherically symmetric geometry. The possibility of a prompt explosion mechanism, where the infalling matter directly expands after bouncing off the inner core, had to be discarded very soon [88]. With this, the search for a mechanism that could explain the successful revival of the shock began. It took almost two decades until Bethe & Wilson (1985) [24] introduced the delayed neutrino-heating mechanism into simulations.

Supernova simulations combine many different fields of physics, such as hydrodynamics, gravity, particle and nuclear physics. In the following, we discuss the individual ingredients to a CCSN simulation. We cover the underlying physics as well as assumptions and simplifications that are commonly made, with special focus on the methods that we use in this study.

3.1. Hydrodynamics

Hydrodynamics is the key ingredient for the description of the fluid behavior in CCSN simulations. In the following, we will derive the Euler equations from general assumptions. We follow Ref. [89–92].

An ensemble of particles in the six-dimensional phase-space of space $\vec{x}$ and velocity $\vec{v}$ is described with the distribution function $f(\vec{x}, \vec{v}, t)$ at a given time t. With a fixed number of particles N in the system, we can identify the normalization of the distribution function as

$$\iint f(\vec{x}, \vec{v}, t)\, \mathrm{d}^3x\, \mathrm{d}^3v \;=\; N\ . \tag{3.1}$$

The continuity equation for f reads

$$\frac{\partial f}{\partial t} + \sum_{i=1}^{3} \left(\dot{x}_i \frac{\partial f}{\partial x_i} + \dot{v}_i \frac{\partial f}{\partial v_i} \right) = \left. \frac{\mathrm{d}f}{\mathrm{d}t} \right|_{coll.} . \tag{3.2}$$

Here, $(\mathrm{d}f/\mathrm{d}t)_{coll.}$ is the so-called collision integral, which accounts for particles changing their direction of movement due to interaction with other particles. It has to be defined for the individual context, as interactions may take place because of gravity, electromagnetism or any other force that is relevant on the given scale. Note that $v_i \equiv \dot{x}_i$, and we define the acceleration of a particle as $g_i \equiv \dot{v}_i$. The acceleration $\vec{g}$ may be the result of an external force acting on all particles, such as a gravitational field. Substituting this into equation (3.2) results in the Boltzmann equation,

$$\frac{\partial f}{\partial t} + \sum_{i=1}^{3} \left(v_i \frac{\partial f}{\partial x_i} + g_i \frac{\partial f}{\partial v_i} \right) = \left. \frac{\mathrm{d}f}{\mathrm{d}t} \right|_{coll.} . \tag{3.3}$$

In hydrodynamic applications, the collision integral is usually set to zero. This originates from the idea that the velocity distribution is approximately Maxwellian in a closed system, and velocity changes because of interactions between particles cancel each other out [93].

The Boltzmann equation (3.3) and its collisionless form are generally challenging to solve, as it poses a six-dimensional problem. In general, we do not need the full information of location and velocity of any particle at any time, but rather only the mean density, velocity and energy of a given fluid element. Therefore, it is sufficient for hydrodynamic applications to expand equation (3.3) into moments. We can extract information about the mass density of the fluid by multiplying the Boltzmann equation with the mass m of a particle (for different species one can define separate masses m_{species}, but the calculation will essentially be the same) and integrating over the velocity space:

$$\frac{\partial}{\partial t} \int (mf) \mathrm{d}^3 v + \sum_{i=1}^{3} \frac{\partial}{\partial x_i} \int (m f v_i) \mathrm{d}^3 v + \int \sum_{i=1}^{3} m g_i \frac{\partial f}{\partial v_i} \mathrm{d}^3 v = \int m \left. \frac{\mathrm{d}f}{\mathrm{d}t} \right|_{coll.} \mathrm{d}^3 v \, . \tag{3.4}$$

We identify the mass density $\rho(\vec{x}, t) = \int (m \cdot f(\vec{x}, \vec{v}, t)) \mathrm{d}^3 v$ in the first term and the mean fluid velocity $\vec{u} = \langle \vec{v} \rangle$ in the second term, if we rewrite it as

$$\sum_{i=1}^{3} \frac{\partial}{\partial x_i} (\rho \langle \vec{v} \rangle) \equiv \vec{\nabla} \cdot (\rho \vec{u}) \, . \tag{3.5}$$

The third term vanishes as a result of Gauss's theorem and the assumption that we have a Maxwellian velocity distribution, which implies $\lim_{|\vec{v}|\to\infty} f(\vec{x},\vec{v},t) = 0$. Finally, the collision term is zero by above's argumentation, which in this case is equivalent to local mass conservation, i.e., that particles are neither created nor destroyed in interactions. Altogether, we identify equation (3.4) as the **equation of mass conservation**,

$$\frac{\partial \rho}{\partial t} + \vec{\nabla} \cdot (\rho \vec{u}) \; = \; 0 \; . \tag{3.6}$$

Likewise, one can derive equations for momentum and energy conservation, by multiplying the Boltzmann equation with $m\vec{v}$ and $m\vec{v}^2$, respectively, and again integrating over the velocity space. With the help of Gauss's theorem and the assumed velocity distribution, this results in the **momentum and energy equations**,

$$\frac{\partial (\rho \vec{u})}{\partial t} + \vec{\nabla} \cdot (\rho \vec{u} \otimes \vec{u}) + \vec{\nabla} P \quad = \quad \rho \vec{g} \; , \tag{3.7}$$

$$\frac{\partial (\rho e)}{\partial t} + \vec{\nabla} \cdot (\rho e + P) \vec{u} \quad = \quad \rho \vec{u} \cdot \vec{g} \; . \tag{3.8}$$

Here, we identify the pressure of the fluid P, and define the total specific energy e as the sum of specific internal and kinetic energy, i.e., $e = e_{\text{int}} + 1/2\,|\vec{u}|^2$. Equations (3.6)-(3.8) are the so-called Euler equations of hydrodynamics, which were first derived by Leonhard Euler in the 18^{th} century [94].

It is convenient to separate the acceleration of the fluid at a given point in space and time, $\vec{g}$, into a contribution for gravity and one for additional, model-dependent source terms. In the context of CCSN simulations, gravity is included by substituting $\vec{g}$ with the local gradient of the gravitational potential Φ, which can be solved with Poisson's equation:

$$\vec{g} \quad = \quad -\vec{\nabla}\Phi \; , \tag{3.9}$$

$$\Delta\Phi \quad = \quad 4\pi G \rho \; . \tag{3.10}$$

For the neutrino-driven mechanism, a source term Q_ν is added to the right-hand side of equation (3.8). This additional term accounts for energy transfer by neutrinos. It is calculated as the sum of contributions from several neutrino-matter interactions, which we will discuss in Sec. 3.4. We neglect momentum transfer from neutrinos, i.e., a contribution to equation (3.7), because of the low mass of neutrinos.

3.2. Gravity

Equation (3.10) can be solved with the commonly known Green's function method, which yields

$$\Phi(\vec{x}) \;=\; -G \int \frac{\rho(\vec{x}')}{|\vec{x}-\vec{x}'|} \mathrm{d}^3x' \;, \tag{3.11}$$

for any density distribution $\rho(\vec{x})$. The numerical integration is conveniently performed with a multipole expansion of the form

$$\Phi(\vec{x}) \;\approx\; -G \sum_{l=0}^{l_{\max}} \sum_{m=-l}^{l} \frac{4\pi}{2l+1} Y^{lm}(\vec{x}/r) \left(\frac{1}{r^{l+1}} C^{lm}(r) + r^l D^{lm}(r) \right) \;, \tag{3.12}$$

with $r = |\vec{x}|$ and the spherical harmonic functions Y^{lm} [95]. The advantage of this formulation is the separation of angular and spherical components. The coefficients C^{lm} and D^{lm} depend only on the radial coordinate r, while the angular dependency is contained in the spherical harmonics. Finally, $l_{\max}$ is a cutoff parameter, where for $l_{\max} \to \infty$, equation (3.12) converges to the exact value for $\Phi(\vec{x})$. Following Ref. [96], we set $l_{\max} = 16$ for this study.

3.3. Equation of state

The Euler equations (3.6)-(3.8) are a set of five equations (accounting for the dimensionality of the equation of momentum conservation (3.7)). However, the equations contain a total of six unknown variables (ρ, P, e and $\vec{u}$). To close the system of equations, a sixth relation is necessary. In principle, the inclusion of several particle species introduces additional variables and equations, with source terms from nuclear reactions. This is usually simplified for the purpose of simulations. With knowledge of the fluid composition, one can relate density, pressure and energy (e.g., $P = P(\rho, e)$) in a so-called equation of state (EOS). In general, an EOS can take one of many forms, depending on the matter composition. One of the most common examples is the ideal gas equation, which can be expressed with the properties above as

$$P \;=\; (\gamma - 1)\, \rho\, e \;, \tag{3.13}$$

where γ is the adiabatic index, which is related to the degrees of freedom in an ideal gas. For adiabatic processes, one can write this in the form of a polytropic equation,

$$P = K\,\rho^{\gamma}\ , \tag{3.14}$$

where K is a constant related to the entropy of the system. Polytropic EOSs have been proven to be extremely useful in numerical astrophysics, as they are easy to handle and provide a reasonable approximation for the interior of white dwarves (e.g., the Chandrasekhar limit was derived on this assumption [97]) and neutron stars (e.g, see Ref. [98]).

A more realistic approach towards an EOS for a given composition of matter requires a description with thermodynamic potentials. Consider the internal energy U, which has the total differential

$$\mathrm{d}U = T\mathrm{d}S - P\mathrm{d}V + \sum_i \mu_i \mathrm{d}N_i\ , \tag{3.15}$$

for a given temperature T, entropy S, volume V and particle number N_i for any species i. The chemical potential μ_i is the energy required for one particle of species i to be added to the system. A Lagrange transformation leads to the total differential of the free energy,

$$\mathrm{d}F = \mathrm{d}U - \mathrm{d}(S\cdot T) = -P\mathrm{d}V - S\mathrm{d}T + \sum_i \mu_i \mathrm{d}N_i\ . \tag{3.16}$$

In contrast to the internal energy, which has the natural variables (S, V, N), the free energy depends on (T, V, N). It provides the most convenient description of a system in which the temperature may not change as rapidly as the entropy or pressure, so that an isothermal description is justified. We can relate the volume V to the matter density of a fluid via $\rho = m/V$, and to the particle density, $n_i = N_i/V$. Defining the abundance Y_i of a given species as

$$Y_i = \frac{n_i}{\sum_i n_i}\ , \tag{3.17}$$

we can use the triplet of density, temperature and abundances to gain all other informations about the system in a CCSN with the free energy. Furthermore, the free energy can be used to link the microscopic and macroscopic descriptions via the relation

$$F = -k_B\,T\ln(Z)\ , \tag{3.18}$$

with the Boltzmann constant k_B and the partition function $Z(T, V, N)$. The partition function is the amount of all possible states in a system with given temperature, volume, and particle number.

In CCSN simulations, there are generally two regimes with different matter properties to be considered. Matter at low densities ($\rho \lesssim 10^{10}\,\mathrm{g/cm^3}$) can be found outside of the proto-neutron star (PNS). Because the distances between individual particles are comparably large, the strong interaction can be neglected. Free nucleons are usually bound in ions, which add to the composition of the matter together with electrons, positrons and photons (radiation). The free energy can be expressed as the sum of its individual contributions as (see Ref. [72, 99, 100])

$$F = F_{\mathrm{ion}} + F_{\mathrm{e^-}} + F_{\mathrm{e^+}} + F_{\mathrm{rad}} \,. \tag{3.19}$$

This equation describes the so-called Helmholtz EOS. In this study, we assume the ion contribution to be that of an ideal gas (equation (3.13)) with an adiabatic index of $\gamma = 5/3$. The electron and positron gas is based on the description of an non-interacting Fermi gas, in which the number densities are expressed as

$$n_{\mathrm{e^-}} = \frac{8\pi\sqrt{2}}{h^3} m_e^2 c^3 \beta^{3/2} \left[F_{1/2}(\eta,\beta) + F_{3/2}(\eta,\beta)\right] , \tag{3.20}$$

$$n_{\mathrm{e^+}} = \frac{8\pi\sqrt{2}}{h^3} m_e^2 c^3 \beta^{3/2} \left[F_{1/2}(-\eta - 2/\beta,\beta) + \beta F_{3/2}(-\eta - 2\beta,\beta)\right] . \tag{3.21}$$

Here, m_e is the electron mass, h is Planck's constant, $\beta = k_B T/(m_e c^2)$ is the relativity parameter and $\eta = \mu/(k_B T)$ is the normalized chemical potential energy. $F_{1/2}$ and $F_{3/2}$ are the Fermi-Dirac integrals defined by

$$F_j(\eta,\beta) = \int_0^\infty \frac{x^j}{\exp(x-\eta)+1} \sqrt{1 + \frac{\beta x}{2}}\, \mathrm{d}x \,. \tag{3.22}$$

For computational efficiency, analytic approximations of the Fermi-Dirac integrals for the non-relativistic limit ($\beta \approx 0$) can be found in Ref. [101].

The radiation component in equation (3.19) is assumed to be that of black-body radiation in thermodynamic equilibrium:

$$P_{\mathrm{rad}} = \frac{aT^4}{3} , \tag{3.23}$$

$$e_{\mathrm{rad}} = \frac{3P_{\mathrm{rad}}}{\rho} , \tag{3.24}$$

where $a \approx 7.566 \cdot 10^{-15}\,\mathrm{erg\,cm^{-3}\,K^{-4}}$ is related to the Stephan-Boltzmann constant.

The high-density region within the PNS requires a different approach for the EOS. The strong interaction can not be neglected here and free nucleons exist along with bound nuclei, leptons, and photons. Since a complete solution to the nuclear many-body problem with ab-initio methods is not feasible yet, one has to rely on phenomenological methods like the Skyrme interactions with parameters derived from both theory and experiments. The resulting EOSs are usually tabulated for an efficient use in CCSN simulation codes. In this study, we use the EOS of Lattimer & Swesty (1991) [102] with an incompressibility of $K = 220$ MeV, also termed LS220. The EOS table contains 240 points for the density, 148 for the temperature and 50 for the electron fraction, and is interpolated during the simulation. The LS220 assumes matter to be composed of free nucleons (both protons and neutrons), light nuclei (represented by α-particles), heavy nuclei (represented by a single heavy nucleus N in a so-called single nucleus approximation), electrons, positrons and radiation. The free energy is thus

$$F = F_{\mathrm{nuc}} + F_{\alpha} + F_{\mathrm{N}} + F_{\mathrm{e^-}} + F_{\mathrm{e^+}} + F_{\mathrm{rad}} \,, \tag{3.25}$$

where F_{nuc} denotes the contribution from free nucleons.

The lowest density in the LS220 table is $\rho = 10^3 \ \mathrm{g/cm^3}$. However, for our long-time simulations we use an extended 2D domain with a size of $1.6 \cdot 10^{10}$ cm along the equatorial and each polar directions. At these large radii, the matter density in the progenitor is lower than the LS220 table limit (compare to Fig. 2.5). We therefore use a hybrid EOS approach, where a transition to the Helmholtz EOS (3.19) is performed. We refer to Ref. [103] for the details of this calculation.

3.4. Neutrino treatment

We discussed the importance of neutrinos for the CCSN mechanism and specifically for the revival of the stalled shock in Sec. 2.1.3. Neutrinos are particles of very low mass that only interact via the weak interaction. Current experiments constrain the mass scale of neutrinos to less than 1.1 eV [104], while constraints from cosmological observations predict a value about an order of magnitude lower than that [105, 106]. Furthermore, neutrinos are subject to flavor oscillations, a quantum mechanical result of their mass eigenstates being different from their flavor eigenstates. In the context of CCSN simulations, neutrinos are described with the relativistic form of the Boltzmann equation (3.3),

which can be written as (see Ref. [107])

$$p^\alpha \left(\frac{\partial f_\nu}{\partial x^\alpha} - \Gamma^\beta_{\alpha\gamma}\, p^\gamma \frac{\partial f_\nu}{\partial p^\beta} \right) = \left. \frac{\mathrm{d} f_\nu}{\mathrm{d} t} \right|_{coll.} , \tag{3.26}$$

where p^α is the four-momentum and $\Gamma^\beta_{\alpha\gamma}$ denotes the Christoffel symbol. This is a seven-dimensional equation for all neutrino energies, spatial points and propagation angles, as a function of the time $t = x^0$. The collision term on the right-hand side is crucial for the description of the trapped neutrinos in the PNS, as it dominates the transport terms on the left-hand side. In the optically thin layers outside of the PNS, where neutrinos are streaming freely, the transport terms govern the evolution of the neutrino distribution function. The transition between these two regimes is one of the most challenging tasks in CCSN simulations. The neutrinosphere lies within the transition region and its exact location critically affects the energies of emitted neutrinos [108]. As a complete treatment of equation (3.26) is computationally not feasible without sacrificing resolution, it is common to make simplifications and derive approaches from them (however, see Ref. [109] for an example of 2D simulations with full Boltzmann neutrino transport). These approaches include, among others, the Isotropic Diffusion Source Approximation (IDSA) [110] or the more commonly used two-moment M1 transport scheme with an analytic closure relation. We refer to Ref. [111, 112] for the basics of the moment formalism, Ref. [108, 113–115] for examples of its application, and Ref. [28] for a comparison of IDSA and M1 with a spectral leakage scheme [116]. In the following, we focus on the leakage scheme approach, which we use in this study.

3.4.1. Leakage/heating scheme

Leakage schemes are a comparably easy approximation to incorporate neutrinos in CCSN simulations. They only act locally and do not actually evolve the neutrino distribution function. This reduces the computational costs and provides a certain amount of flexibility. Neutrino leakage schemes are well-known and have been applied to a variety of scenarios, with examples including neutrino emission from stellar cores [117], magnetorotational supernova explosions [118, 119], the impact of progenitor asphericity on CCSN [120], and multimessenger signatures from neutron star mergers [121]. However, they result in luminosities and electron fractions that quantitatively can differ from more sophisticated neutrino transport methods [28, 122]. We explain the construction of the gray (i.e., energy-independent) leakage scheme from Ref. [70, 71], which we also use for the simulations in this study.

In general, a leakage scheme evaluates the local emission rates of energy and lepton number, and directly subtracts these values from the local matter properties. We use $Q_\nu = \mathrm{d}\epsilon_\nu/\mathrm{d}t$ and $R_\nu = \mathrm{d}(Y_e)_\nu/\mathrm{d}t$ as labels for the rate of energy and lepton number emission, respectively. In optically thick matter, neutrinos escape on a diffusion timescale, while in the optically thin region, they are assumed to stream away freely, at a rate based on their emission rate. Between these two regimes, we use an interpolation to calculate the total cooling rate from neutrino emissions. It takes the form

$$Q_{\nu,\mathrm{cool}} = \frac{Q_{\nu,\mathrm{free}} \cdot Q_{\nu,\mathrm{diff}}}{Q_{\nu,\mathrm{free}} + Q_{\nu,\mathrm{diff}}} \,, \tag{3.27}$$

and likewise for R_ν. The "free" and "diff" subscripts indicate the contribution from the optically thin and thick regions, respectively. The leakage scheme from Ref. [70, 71] calculates the free emission rates based on nuclear processes that emit neutrinos. Specifically, we include contributions from electron and positron capture on nucleons, electron-positron annihilation, nucleon-nucleon bremsstrahlung and plasmon decay. For the diffusive counterparts of each contribution, we have to account for the mean free path of the neutrinos, in relation to the length of the way out of the dense matter. In the leakage scheme, the optical depth for the emission point of a neutrino is calculated by integrating the local opacities on its way to infinity. While this is trivial in one dimension, where there is only the radial coordinate, this method introduces difficulties in simulations in two and three dimensions.

The leakage scheme uses on a so-called ray-by-ray approach, where we assume neutrinos to diffuse out of the PNS along radial rays from the center of the PNS to infinity. For our two-dimensional simulations, we use 37 rays ($\sim 5^\circ$ spacing), each composed of 1000 radial zones (linear spacing in 0.5 km steps up to 150 km, then logarithmic), up to a maximum radius of 3000 km. Each calculation cell can be assigned one of the 37 rays and one radial zone, depending on its position. The local opacities are calculated by taking into account elastic scattering of neutrinos on nucleons and absorption of electron neutrinos and antineutrinos on neutrons and protons, respectively.

A basic leakage scheme only accounts for the local emission of neutrinos. It does not calculate the absorption and resulting heating rate of the emitted neutrinos at a radius further out. However, since the CCSN explosion mechanism crucially depends on neutrino heating, one has to introduce heating source terms for a successful explosion. With a given number of emitted neutrinos along the radial direction, we can calculate luminosities for each simulated ray. The energy luminosity $L_\nu(r)$ is obtained by integrating the local values of Q_ν from the center of the PNS up to the desired radius r. The dominat-

ing heating process is neutrino absorption on nucleons, to which only electron neutrinos and antineutrinos contribute. Heating contributions from heavy-lepton neutrinos are neglected. The total heating rate is then determined from the absorption cross-section and the number of available targets and incoming neutrinos:

$$Q_{\nu,\mathrm{heat}} = \frac{L_{\nu_i}(r)}{4\pi r^2}\,\sigma_{\nu_i}\,\frac{\rho X_{n/p}}{m_n}\left\langle\frac{1}{F_{\nu_i}}\right\rangle e^{-2\,\tau_{\nu_i}}\,. \tag{3.28}$$

Here, $\rho X_{n/p}/m_n$ is the number density of possible absorbers with the fluid density, neutron/proton mass fraction and the neutron mass. The ν_i subscripts indicate the contributions from both electron neutrinos and antineutrinos, which are absorbed by neutrons and protons. The mean inverse flux factor $\left\langle F_{\nu_i}^{-1}\right\rangle$ accounts for neutrinos that are not ejected strictly in the radial direction, as we assume in the ray-by-ray approach. Realistically, a fluid element can be reached by neutrinos that originate from different locations in the PNS. Following O'Connor & Ott (2010) [70], this factor is approximated as $4.275\ \tau_{\nu_i} + 1.15$. The optical depth τ_{ν_i} is calculated following Ref. [123]. The last term in equation (3.28) suppresses additional heating in the PNS, where charged current reactions are already taken into account for calculating the emission rates. Finally, the absorption cross-sections σ_{ν_i} are computed analogously to Ref. [124], as

$$\sigma_{\nu_i} = \frac{1+3\,g_A^2}{4}\sigma_0\left(\frac{\epsilon_{\nu_i}}{m_e c^2}\right)^2 B_{\nu_i}\,, \tag{3.29}$$

where $g_A = -1.25$ is the coupling constant for the charged-current axial vector, and $\sigma_0 = 1.76\cdot 10^{-44}\ \mathrm{cm}^2$. The neutrino energies ϵ_{ν_i} are calculated at the neutrinosphere (which we define at $\tau_{\nu_i} = 2/3$). The lepton blocking factor B_{ν_i} depends on the chemical potential of electrons and the respective neutrino species and is defined analogously to Ref. [123, 124]. The resulting heating term from equation (3.28) and the emitted energy from equation (3.27) are applied as source terms to the hydrodynamic equation of energy conservation (3.8), which then becomes

$$\frac{\partial(\rho e)}{\partial t} + \vec{\nabla}\cdot(\rho e + P)\vec{u} = \rho\vec{u}\cdot\vec{g} + (Q_{\nu,\mathrm{heat}} - Q_{\nu,\mathrm{cool}})\,. \tag{3.30}$$

Leakage schemes can not account properly for the deleptonization of the collapsing core prior to bounce. We therefore rely on an additional deleptonization scheme that is applied in the simulation before bounce. We use the parametric scheme of Liebendörfer (2005) [125], which was derived on the basis of data from a general relativistic, spherically symmetric CCSN simulation with accurate neutrino Boltzmann transport.

3.5. Rotation

Stars commonly rotate, with the most prominent example being our own sun, whose rotation was discovered all the way back by Galileo Galilei. In the context of CCSN, rotation can play an important role. When the iron core with a radius of a few thousand kilometers collapses to a PNS with a radius of only a few tens of kilometers, conservation of angular momentum yields an increase of the spin frequency of the order $\sim 10^4$. If a PNS is (rapidly) rotating, this can in turn influence its shape due to centrifugal forces, which leads to anisotropies in the neutrino emission and thus also in the explosion morphology. The impact of a rotating progenitor star on the supernova explosion and long-time evolution of the ejected matter has been under discussion almost as long as the CCSN mechanism itself. The first simulations were performed by LeBlanc & Wilson in 1970 [126], who calculated three configurations (non-rotating progenitor, rotating progenitor, rotation with magnetic fields) in an axisymmetric domain.

Whether or not a rotating progenitor is beneficial or detrimental for shock revival, has been debated for a long time now. The answer seems to depend very much on the details of the respective simulation, its dimensionality, the actual spin period of the progenitor, and the inclusion of magnetic fields. Fryer & Heger (2000) [127] found in their 2D study that rotation limits convection in the gain region during the explosion phase, and reduces neutrino luminosities and energies, thus leading to weaker explosions. Thompson et al. (2004) [128] (1D simulation) also reported a reduced neutrino luminosity as a consequence of rotation, but noted that magneto-rotational instabilities can enhance the explosion greatly. It was hinted by Mösta et al. (2014) [129] that 3D simulations might be necessary to capture the full effects of rotation, especially when including magnetohydrodynamics. Other studies showed that in 2D, rapidly rotating models may not explode [130], while in 3D rotation can actually aid the explosion [131]. Additionally, the grid resolution has a big impact on the efficiency of angular momentum transfer [29]. More recently, a detailed 2D steady-state study of Fujisawa et al. (2019) [30] investigated the effect of rotation on the standing accretion shock in CCSN. They found that rapid rotation might lower the critical neutrino luminosity that is necessary to obtain a successful explosion. In this study, they derived a critical angular momentum criterion for successful explosions.

In general, the inclusion of rotation in a CCSN simulation introduces an interplay of two main effects (we neglect magnetic fields here), of which one acts in favor of a successful explosion, while the other one acts against it. Advantageous for shock revival are the centrifugal forces that influence the matter before the shock and reduce its infall velocity.

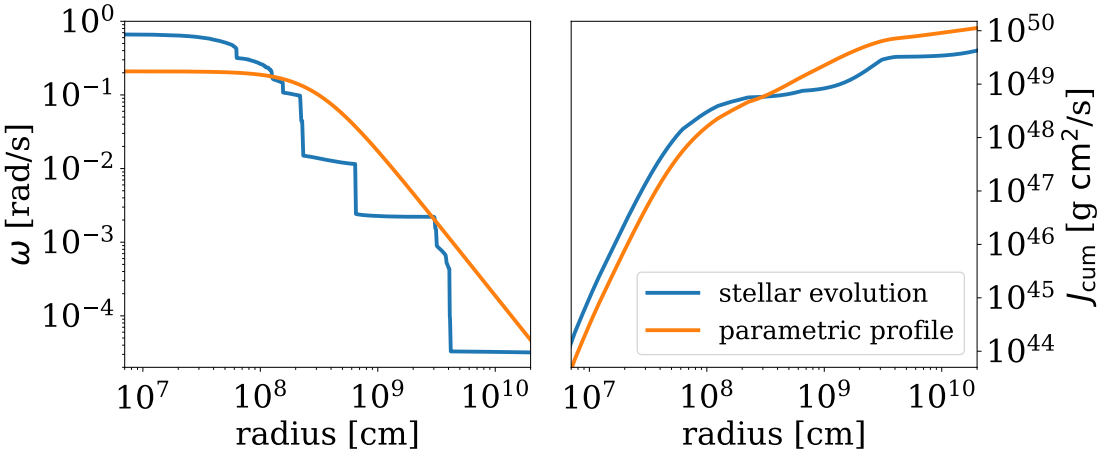

Figure 3.1.: Rotational profile in angular velocity (left) and cumulative angular momentum (right) for the E15 progenitor from Ref. [132] and the parametric profile following equation (3.31).

As a consequence, the mass accretion and ram pressure on the stalled shock are lowered, allowing for an easier revival. On the other hand, a reduced mass accretion leads to lower neutrino (accretion) luminosities and reduced convection, therefore providing less energy for the shock. Which of these effects is the dominant one seems to depend on simulation details and the angular momentum of the progenitor. Given the somewhat disagreeing studies on this topic that we mentioned above, it seems that currently there is no definite answer to this question.

Simulations with rotating progenitors can either begin with an already rotating progenitor, i.e., that rotation and angular momentum transport were already considered during the stellar evolution calculations, or with a static progenitor and a super-imposed rotational profile. We show a comparison of the two possibilities in Fig. 3.1, with the angular velocity profile in the left panel and cumulative angular momentum profile in the right panel. The progenitor displayed is the rotating E15 model from Heger et al. (2000) [132]. The parametric profile follows the relation

$$\Omega(r) \;=\; \Omega_0 \cdot \frac{1}{1 + (r/r_A)^2}\,, \tag{3.31}$$

where we set $r_A = 3000$ km as the characteristic radius (approximately the size of the iron core). We chose $\Omega_0 \approx 0.21$ rad/s such that the total angular momentum enclosed

in a sphere with $r = r_A$ is the same as in the E15 model. The shell structure from the rotating stellar model is not reproduced in the parametric profile. However, the general trend is qualitatively similar. Furthermore, recent studies on multi-dimensional effects in the progenitor evolution also suggest that important effects are missing in the calculation of 1D progenitors (e.g., see Ref. [83, 133] for examples of 3D progenitor calculations and Ref. [134] for a discussion on the effect of internal gravity waves on angular momentum transport prior to collapse).

3.6. Simulation setup in FLASH

We close this chapter by giving an overview of our general simulation setup, which we use to obtain the results in the next chapters. We employ the multiphysics FLASH code, version 4.2.2 [72, 73], for all CCSN simulations in this study. We perform 2D simulations in a cylindrical geometry. The domain size for all simulations is $3.2 \cdot 10^{10}$ cm along the cylindrical axis and $1.6 \cdot 10^{10}$ cm perpendicular to it. Our setup is similar to previous core-collapse supernova studies with FLASH (see, e.g., Ref [31, 71]). We solve the Euler equations in a directional-unsplit fashion with a piecewise parabolic method hydrodynamics scheme [135]. Near shocks, we employ an HLLE Riemann solver and an HLLC solver everywhere else. We calculate self-gravity with a multipole approximation [96] of Poisson's equation up to the 16th Legendre order, but omit the use of an effective general relativistic potential, using purely Newtonian gravity. More details on the simulation setup with an example parameter file can be found in the appendix A.

The cylindrical axis is treated as a reflective boundary, where the normal vector components of hydrodynamic fluxes change sign. The other three boundaries are set up for inflow/outflow of matter, by enforcing a zero gradient condition there. The grid structure in FLASH is managed by the adaptive mesh refinement (AMR) toolkit PARAMESH [75]. Computational block are refined and derefined, based on density, pressure, and entropy criteria. We use a total of 40 (20) initial blocks along (perpendicular to) the cylindrical axis, and a maximum refinement level of 11. Each block consists of 16×16 cells. The maximum resolution in our simulations is therefore ≈ 488 m. We show an example of the AMR grid structure in Fig. 3.2. The individual boxes correspond to computational blocks, and we overplot them with entropy gradients of the simulation. The refinement level of the blocks is also determined by the radius, in addition to criteria based on hydrodynamic quantities.

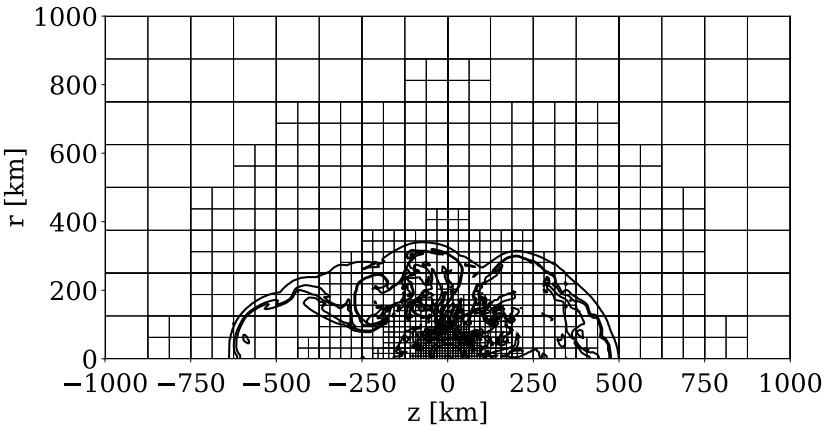

Figure 3.2.: Grid structure of the AMR with underlying entropy gradients.

We use the “s15.0” progenitor of Woosley et al. (2002) [37] for all simulations in chapters 4 & 5. This model has been employed in various other CCSN simulation studies (e.g., see Ref. [64, 136, 137]). It is a non-rotating progenitor with solar metallicity and a zero-age main sequence mass of $15\ M_\odot$. We investigate two more progenitors, namely the “s11.2” and the “s27.0” models of the same series, in chapter 7.

All simulations are performed on the Lichtenberg high performance computer of the TU Darmstadt, with 24 parallel MPI processes per model.

4. Core-collapse supernova simulations with varied neutrino heating

In the following chapter, we investigate the impact of different explosion energies by artificially varying the energy deposited by neutrinos. We use the heating factor in FLASH and explore its effect on simulations. We consider changes to the default implementation and discuss their suitability and long-term effects. With a fixed setup that emerges from this discussion, we then conduct long-time simulations of core-collapse supernovae (CCSN). The results discussion is divided into two sections by first evaluating the explosion phase right after bounce, and afterwards the long-time evolution of the successfully exploding models.

4.1. The heating factor in FLASH

4.1.1. General definition

The current implementation of a gray neutrino leakage/heating scheme in FLASH 4.2.2 [70, 71] as described in Sec. 3.4.1 does not yield self-consistent explosions for many progenitors in 2D simulations. In the following, we use this scheme, which consists of an energy-independent leakage of neutrinos with a ray-by-ray approximation, plus absorption terms for the heating contribution. A simple approach to obtain successful explosions is an artificial increase of the energy deposition rate by neutrinos. In order to have a variable handle on the neutrino heating rate, a "heating factor" f_{heat} was introduced into the FLASH leakage implementation for the studies in Ref. [31, 70, 71]. In its standard implementation, the heating factor affects the energy deposition rate via

$$Q_{\mathrm{net},f} \;=\; f_{\mathrm{heat}} \cdot Q_{\mathrm{heat}} - Q_{\mathrm{cool}} \;, \tag{4.1}$$

where we omitted the ν subscripts for the energy deposition rates in contrast to Sec. 3.4.1. For values $f_{\mathrm{heat}} > 1$, this actively increases the energy source terms from neutrinos. Depending on the simulation setup, a specific critical value is necessary to deposit enough energy to revive the shock and achieve an explosion. Specifically, the critical f_{heat} highly depends on the progenitor and the dimensionality, where 2D models usually do not need as much additional heating as their 1D and 3D counterparts [71]. The value is much higher for 1D simulations, where convection of matter during the explosion phase, which is beneficial for shock revival in multi-dimensional simulations, cannot happen. For low-mass progenitors, the heating factor is often not necessary in 2D because these stars are more readily explodable, as we will see in chapter 7. The enhanced explodability of low-mass stars also emerges from parametric models of CCSN, where no black hole formation is predicted below progenitor masses of $\approx 15\ M_{\odot}$ [59, 61, 62].

In the original implementation, equation (4.1) is applied everywhere. The neutrino luminosities are calculated from the difference of cooling and heating rates, which means that not only the energy deposition rate, but also the luminosities are affected by the heating factor. Close to the neutrinosphere, where $Q_{\mathrm{cool}} > Q_{\mathrm{heat}}$, the luminosities are reduced for $f_{\mathrm{heat}} > 1$.

4.1.2. Implementation methods

Restricting the heating factor to the gain region

The original implementation of equation (4.1) as used in Ref. [31, 70, 71] is valid everywhere in the computed domain. In that way, not only the heating behind the shock is altered, but also the neutrino emission from the proto-neutron star (PNS), as the luminosities are calculated from the local difference of cooling and heating rates. However, the artificial change of the luminosities is not necessary and can also be detrimental at times where the explosion would actually suffer from a decreased neutrino flux. We therefore choose another implementation method, where the heating factor is applied only in the gain region, i.e., where $Q_{\mathrm{heat}} - Q_{\mathrm{cool}} > 0$:

$$\widetilde{Q}_{\mathrm{net},f} = \begin{cases} Q_{\mathrm{heat}} - Q_{\mathrm{cool}}, & \text{if } Q_{\mathrm{heat}} - Q_{\mathrm{cool}} \leq 0\ , \\ f_{\mathrm{heat}} \cdot Q_{\mathrm{heat}} - Q_{\mathrm{cool}}, & \text{if } Q_{\mathrm{heat}} - Q_{\mathrm{cool}} > 0\ . \end{cases} \tag{4.2}$$

The gain region can be seen in Fig. 4.1 as the red area for a simulation around 100 ms after bounce. The PNS still contracts and cools by emission of neutrinos, where the cooling-

dominated region is marked by the blue area. By restricting the heating factor to the gain region we make sure that only the heating is amplified, while the cooling contribution from the PNS remains the same. It shall be noted, however, that the luminosities measured by an observer at infinity will still be reduced, as the increased heating in the gain region leads to a higher absorption rate of neutrinos and consequently to a decreased neutrino flux beyond the gain region.

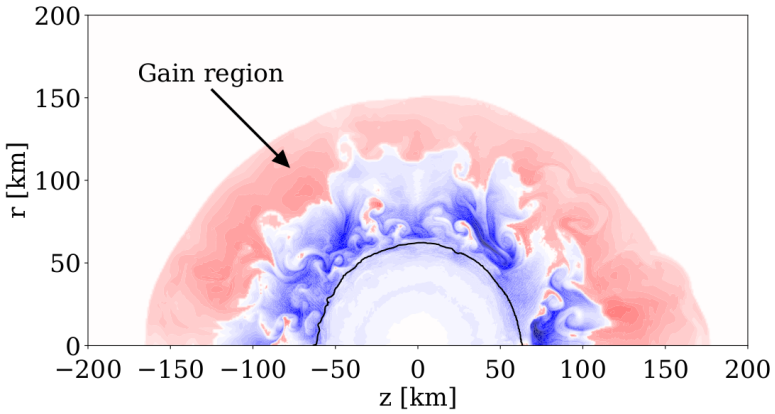

Figure 4.1.: Regions of net neutrino heating (red, gain region) and cooling (blue) in a simulation at 100 ms after bounce. Displayed is the specific heating/cooling rate of the neutrino scheme. The black solid line marks the PNS contour.

The different effect that the two implementations have on the neutrino emission is displayed in Fig. 4.2, where we show the electron neutrino and electron antineutrino luminosities, energies and neutrinosphere radii during the first 200 ms after bounce for a simulation with $f_{\mathrm{heat}} = 1.5$. With the implementation of equation (4.2), both luminosities are increased as expected. The effect is higher for electron neutrinos, as they decouple closer to the gain radius. This more efficient cooling process also leads to a faster contraction of the PNS during the explosion phase, which results in the neutrinospheres being located several kilometers more inside. Neutrino energies are not instantaneously affected but also increase for the new implementation after ~ 40 ms, as a result of the reduced PNS radius and therefore higher temperatures at the neutrinosphere.

Although the neutrino luminosities are increased, applying the heating factor only in the gain region leads to weaker explosions. In general, we now apply less heating to the matter surrounding the PNS and the gain region is smaller than before, where $Q_{\mathrm{net},f}$ could be positive even when the difference of Q_{heat} and Q_{cool} was negative. Taking an

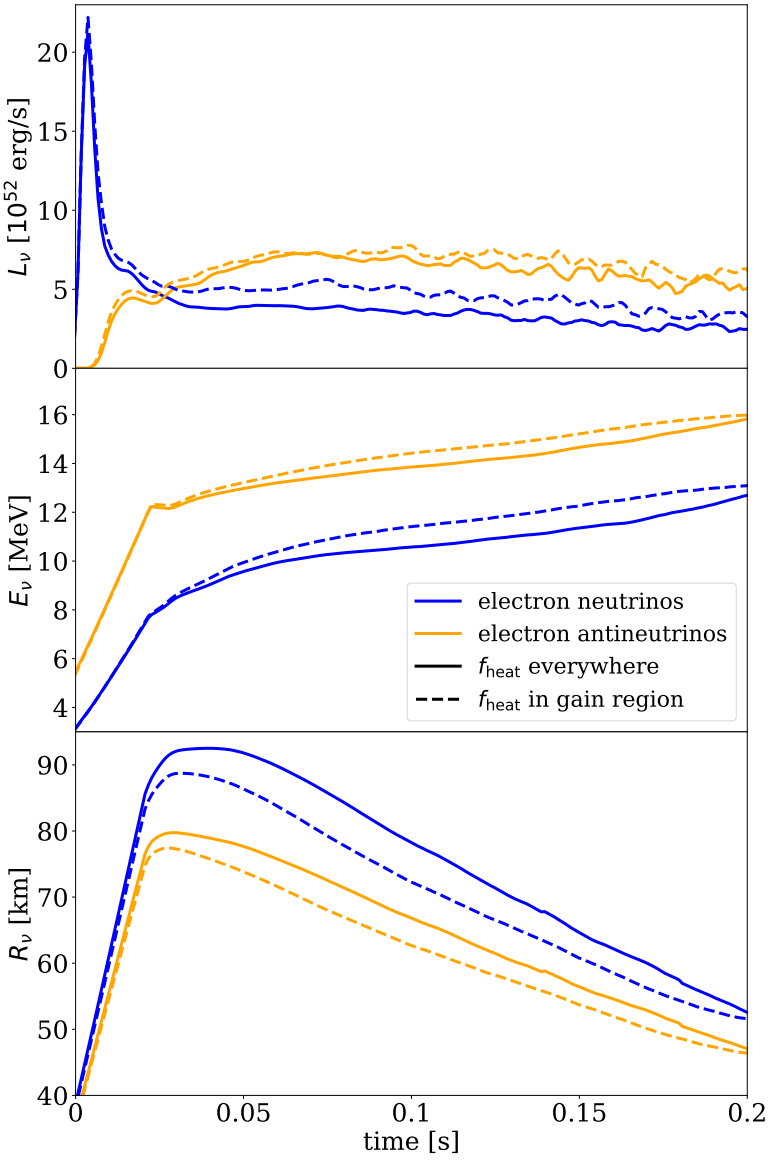

Figure 4.2.: Neutrino luminosities (top), energies (middle) and neutrinosphere radii (bottom) for the original implementation in equation (4.1) and for the restriction to the gain region, as in equation (4.2). In both cases we set $f_{\mathrm{heat}} = 1.5$.

average over the first 100 ms after bounce, we find that the mean entropy between the gain radius of the new implementation and $r = 3000$ km is reduced by 7 %. With the same example as before, we see in Fig. 4.3 that the shock radius is reduced and the explosion sets in at a later time. We define the explosion time t_{exp} as the time when the maximum shock radius reaches 600 km, i.e., $R_{\mathrm{shock,max}}(t_{\mathrm{exp}}) = 600$ km. For $f_{\mathrm{heat}} = 1.5$, the explosion time increases from previously 154 ms to now 170 ms.

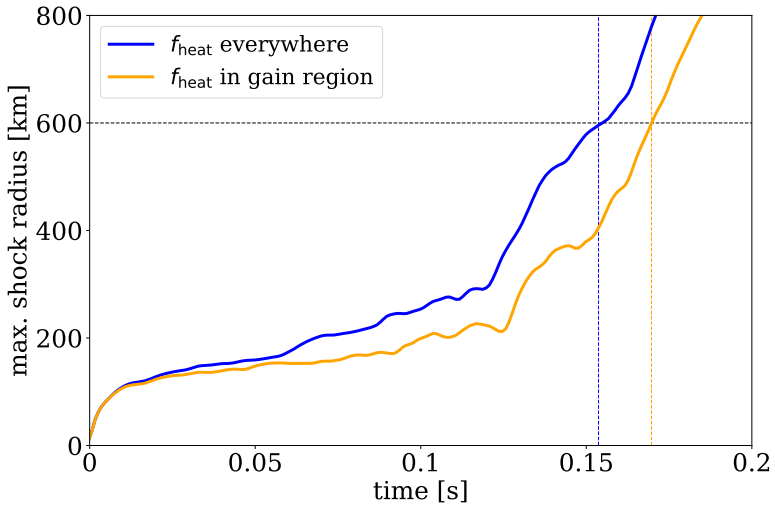

Figure 4.3.: Shock radii for the original implementation in equation (4.1) and for the restriction to the gain region, as in equation (4.2). In both cases we set $f_{\mathrm{heat}} = 1.5$. The dashed lines indicate the explosion times.

Additionally, the threshold above which explosions generally occur, in contrast to having a failed supernova without successful shock revival, increases from $f_{\mathrm{heat}} = 1.05$ to $f_{\mathrm{heat}} = 1.08$ in our setup.

Decreasing the heating factor after shock revival

Once the explosion sets in and the shock is revived successfully, there is no further need for additional heating. Artificially increased energy deposition by neutrinos would, however, impact the long-time evolution in an unphysical way and also bias the explosion energy. We therefore disable the heating factor by decreasing it from its original value to unity. There is a number of ways to smoothly transition from the increased heating regime

during the explosion phase to the phase without additional heating. We shall highlight a few possibilities and their implications for the simulation.

The easiest way to decrease the heating factor is by setting it to 1.0 after a given time, for example 1 s after bounce. This step-function approach can cause numerical artifacts, when a large fraction of heating suddenly vanishes. As a consequence, the neutrino luminosities and energy deposition rates also change in a non-continuous way. It is a smoother method to decrease the heating factor continuously over a given time interval, for example by a linear function. In Fig. 4.4, we show different ways of decreasing the heating factor from an original value of $f_{\mathrm{heat}} = 1.3$. Additionally to the step function approach, we also investigate a linear decrease over 100 or 500 ms, and a decrease following a cosine function over the same time interval.

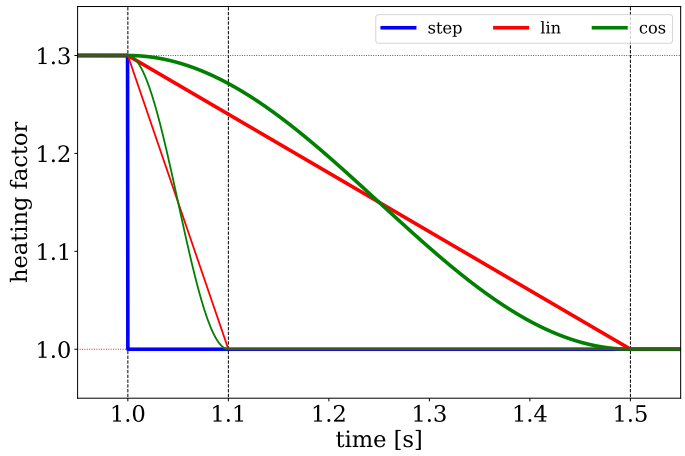

Figure 4.4.: Different ways to decrease the heating factor after 1 s. The thick colored lines show a decrease over 500 ms, while the thin ones decrease the heating factor over 100 ms. The dotted lines indicate the start and end times of the decrease (black) and the original and final values of f_{heat} (red).

In the following, we start all test models with $f_{\mathrm{heat}} = 1.3$ and decrease to $f_{\mathrm{heat}} = 1.0$. For the step-function approach we see an instantaneous decrease in the neutrino energy deposition rate within the gain region by ≈ 30 %, which matches the additional heating that was applied there before by the heating factor. Meanwhile, the integrated heating rate Q_{heat} for the whole simulation domain, both in the cooling and the gain region, is

reduced by $\approx 4\ \%$. This is consistent with the change in the total luminosity of electron neutrinos and electron antineutrinos, which show an increase by $4\ \%$, as a consequence of energy conservation. We note that the respective percentage generally depends on the details of the simulation at that moment, for example on the extent of the gain region.

Although we do not see artificial shock waves or other critical, unintended effects on the hydrodynamics in our example, we cannot exclude this for other simulations. A generally more appropriate method is the use of a continuous decrease function. We therefore run test simulations with the cases shown in Fig. 4.4. Figure 4.5 shows the impact of different methods on both the total neutrino luminosity and the diagnostic explosion energy. We define the latter as the sum of the energy of all fluid cells with a positive total energy,

$$E_{\mathrm{dia}} = \sum_{e_{\mathrm{tot},i}>0} m_i\, e_{\mathrm{tot},i}\,, \tag{4.3}$$

$$e_{\mathrm{tot},i} = \frac{1}{2}|\vec{v}_i|^2 + e_{\mathrm{int},i} + e_{\mathrm{gra},i}\,, \tag{4.4}$$

where $e_{\mathrm{int},i}$ is the specific internal energy, $e_{\mathrm{gra},i}$ the gravitational potential and m_i and $\vec{v}_i$ the mass and fluid velocity of the i-th cell. The black solid line in Fig. 4.5 indicates the reference case where the heating factor is kept constant for the whole time. The instantaneous increase in the luminosity for the step-function case can be seen from the dashed gray line, as well as the resulting impact on the explosion energy, which almost saturates immediately for a few hundred milliseconds.

The continuous functions are labeled “lin_11” and “lin_15” for the linear decrease from $t = 1.0$ s to $t = 1.1$ s and $t = 1.5$ s, respectively, and likewise for the cosine-like functions. As expected, the continuous functions result in an accordingly continuous decrease or increase of the neutrino energy deposition rates and the neutrino luminosities, respectively. While the duration of the decrease plays an important role for the actual change in the neutrino quantities, we see no notable differences when using either the linear or the cosine-like decrease function. In fact, the biggest differences between those two methods appear only after the heating factor has reached unity, as seen for the decrease time of 100 ms.

The criterion of reducing the heating factor always at one second after bounce introduces a bias, as some models explode earlier than others. Depending on the explosion time, in some simulations the shock might not be affected at all by the change, while in others there is an impact on the still evolving explosion. It is therefore more accurate to fix the begin of the decrease function not relative to bounce, but relative to the explosion time.

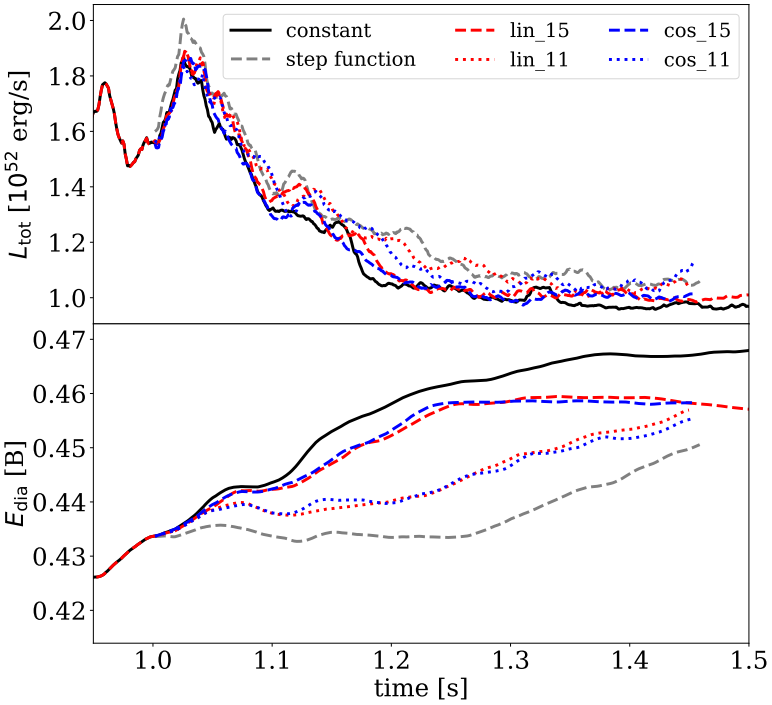

Figure 4.5.: Total neutrino luminosity (top) and explosion energy (bottom) for the different ways to reduce the heating factor displayed in Fig. 4.4.

In the following, we begin to reduce the heating factor when the shock reaches a radius of 1000 km. This happens at a slightly later time than where we define our explosion energy (at 600 km radius) and makes sure that the explosion is already well under way and will not be halted by the loss of additional heating energy. With the considerations mentioned above, we choose the method to reduce the heating factor with a linear function within an interval of 100 ms, as this is the most straightforward approach which does not produce any numerical artifacts.

We conduct three test simulations with different initial heating factors to benchmark the validity of our new implementation and its effect on the explosion energy. As expected, there are no changes to the simulation compared to the case with a constant heating factor, before the shock reaches a radius of 1000 km. After that we see an impact also on the shock profile as a consequence of the now reduced neutrino heating. However, because the shock is already far outside, these differences are small compared to those

between runs with different initial heating factors. We show the evolution of the heating factor for these models in Fig. 4.6, along with that of a non-exploding reference case without additional heating. While the simulation starting with $f_{\mathrm{heat}} = 1.1$ explodes only late (since it is close to the explosion threshold of $f_{\mathrm{heat}} = 1.08$), the models with higher additional neutrino heating both explode within the first 300 ms after bounce. Consequently, the heating factor decreases earlier for these simulations. We see no artificial effects emerging from the different slopes of the heating factor decrease functions.

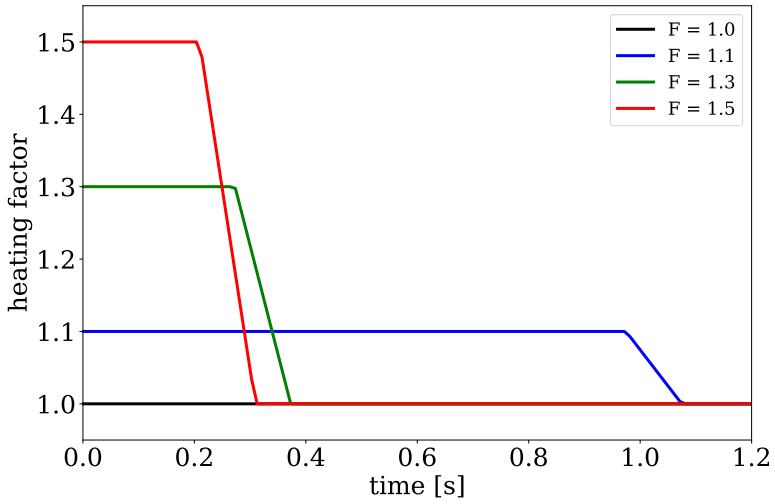

Figure 4.6.: Evolution of the heating factor in simulations with different initial values.

While the impact of the reduced heating factor at late times on the shock evolution is rather small, the explosion energy is much more affected. Once the shock has been revived, the further growth rate of the explosion energy is mainly governed by an interplay of accretion and ejection of matter towards and from the PNS. A higher heating factor allows for a more efficient energy deposition in accreted matter, which is subsequently ejected with higher energy, thus contributing more to the explosion energy. As it could be seen in Fig. 4.5, the impact of a reduced heating factor on the growth of the explosion energy is clearly visible. We continue the new test runs for longer time and show the evolution of the explosion energy in Fig. 4.7. The shock revival leads to a prominent increase shortly after the explosion time, adding already up to 0.3 B for the case with $f_{\mathrm{heat}} = 1.5$. With a constant heating factor, this increase continues for a longer time. When we decrease the heating factor, the growth rate decreases and the explosion energy

almost saturates at values of 0.3 B and 0.45 B for $f_{\mathrm{heat}} = 1.3$ and $f_{\mathrm{heat}} = 1.5$, respectively. It is evident that keeping f_{heat} constant results in a large fraction of the explosion energy being artificial, and therefore to biased values at late times. In the case of $f_{\mathrm{heat}} = 1.1$, the differences are not as big because the artificial heating adds only 10 % instead of 30 % or even 50 %. The explosion energy does not grow as fast in this case because the shock revival is not as energetic as in the other cases.

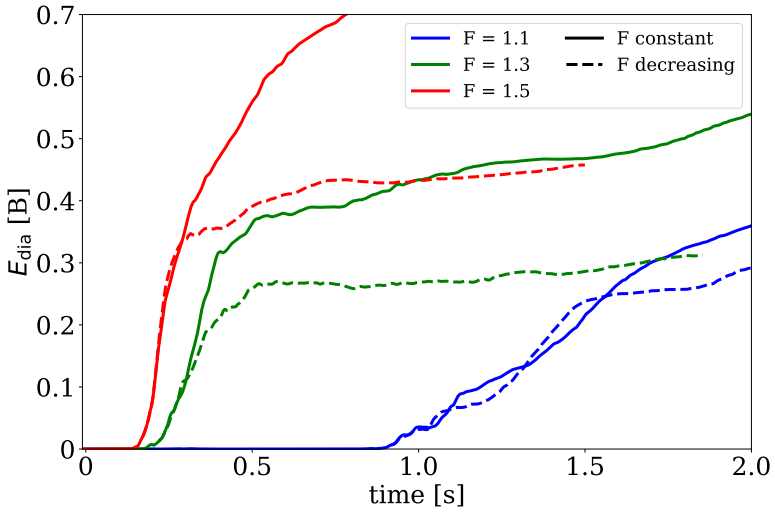

Figure 4.7.: Diagnostic explosion energy for three different initial heating factors with and without decreasing it after shock revival.

4.2. Long-time simulations with varied neutrino heating

In the following, we use the setup described above with a linear decrease of the heating factor within 100 ms, after the shock has reached a radius of 1000 km. We conduct long-time simulations with a total of eight different initial values for f_{heat}. In six of these models the increased neutrino heating leads to a successful explosion, while the two lowest heating factors show no signs of shock revival before their final simulation times of $t_{\mathrm{end}} \approx 1.55$ s after bounce. All other simulations are continued until the shock approaches the domain barrier at a radius of $1.6 \cdot 10^{10}$ cm. In Tab. 4.1, we show the explosion time

and the final simulation time, as well as the explosion energy 100 ms after shock revival and at the end.

f_{heat}	name	t_{exp} [s]	$E_{\mathrm{dia,100ms}}$ [B]	$E_{\mathrm{dia,final}}$ [B]	t_{end} [s]
1.00	F100	-	-	0.00	1.55
1.05	F105	-	-	0.00	1.54
1.08	F108	1.07	0.04	1.16	8.96
1.10	F110	0.93	0.04	1.41	8.14
1.15	F115	0.92	0.04	1.34	9.25
1.20	F120	0.28	0.14	1.21	7.89
1.30	F130	0.23	0.15	0.79	9.26
1.50	F150	0.17	0.30	1.21	7.96

Table 4.1.: Overview of models with different heating factors. The columns show the explosion time (when the shock reaches 600 km radius), the diagnostic explosion energy 100 ms after t_{exp} and at the final time t_{end}.

4.2.1. Explosion phase

From Tab. 4.1 we can distinguish three different explosion behaviors that we cover within our range of different heating factors:

- $f_{\mathrm{heat}} \leq 1.05$: No explosion
- $1.08 \leq f_{\mathrm{heat}} \leq 1.15$: Late explosion
- $f_{\mathrm{heat}} \geq 1.20$: Early explosion

The different explosion times of each group make it possible to separate them clearly. In the following, we investigate why there are these distinct groups and what makes one model fall into one of them.

We show the evolution of the (average) shock radius in Fig. 4.8. For the non-exploding reference model F100, the shock stalls 55 ms after bounce at a radius of 130 km, and subsequently falls back to the PNS down to a minimum radius of 66 km. The models that explode within the first 300 ms revive the shock already before its radius decreases again. For all models, the hierarchy of the explosion time and shock radius evolution

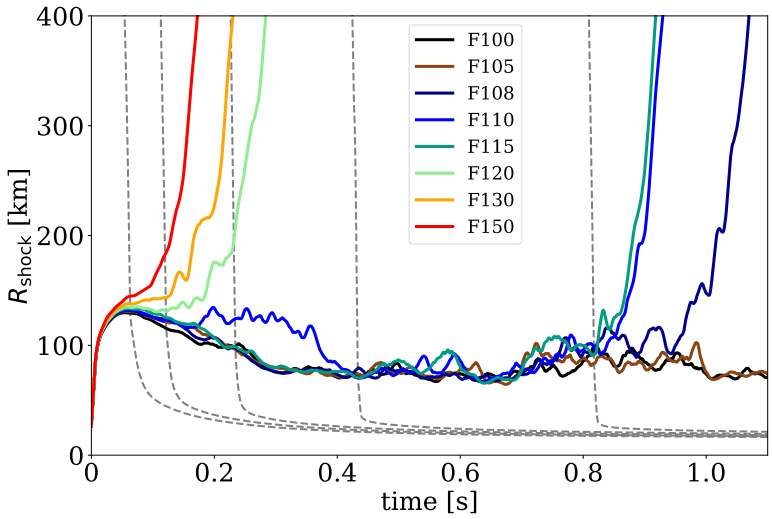

Figure 4.8.: Average shock radii for all models over time. The dashed gray lines indicate infalling progenitor mass shells with $M/M_{\odot} \in \{1.4, 1.5, 1.6, 1.7, 1.8\}$, from left to right, as calculated from the late exploding models.

follows that of the heating factors, as a higher heating factor leads to an earlier and stronger shock revival. The influence of f_{heat} and the subsequently increased neutrino heating rate becomes clear when we compare the characteristic timescales that it takes to advect matter and to heat matter within the gain region, as shown in Fig. 4.9. The significance of these two timescales has been proven by various studies and the condition $\tau_{\mathrm{adv}}/\tau_{\mathrm{heat}} > 1$ is a necessary ingredient for successful shock revival [25]. Our definition of the advection and heating timescales is similar to the one in Ref. [128, 138] (there is a certain ambiguity in the definition, see for example Ref. [139]):

$$\tau_{\mathrm{heat}} = \frac{\mid E_{\mathrm{tot,gain}} \mid}{\dot{Q}_{\mathrm{tot,gain}}}, \tag{4.5}$$

$$\tau_{\mathrm{adv}} = \frac{M_{\mathrm{gain}}}{\dot{M}_{500\mathrm{km}}}. \tag{4.6}$$

Here, $E_{\mathrm{tot,gain}}$ and $\dot{Q}_{\mathrm{tot,gain}}$ correspond to the total energy and total energy deposition rate by neutrinos within the gain region, respectively. The advection timescale is calculated as the mean dwell time of matter in the gain region, analogous to Ref. [130]. M_{gain} denotes the total mass within this region and $\dot{M}_{500\mathrm{km}}$ the mass accretion rate through a radius of

500 km around the PNS. We choose a constant radius for evaluating the mass accretion, as this yields a smoother profile of the resulting timescales and is also applicable at late times, when the shock has traveled so far outwards that the mass accretion through its surface becomes independent of the matter close to the PNS.

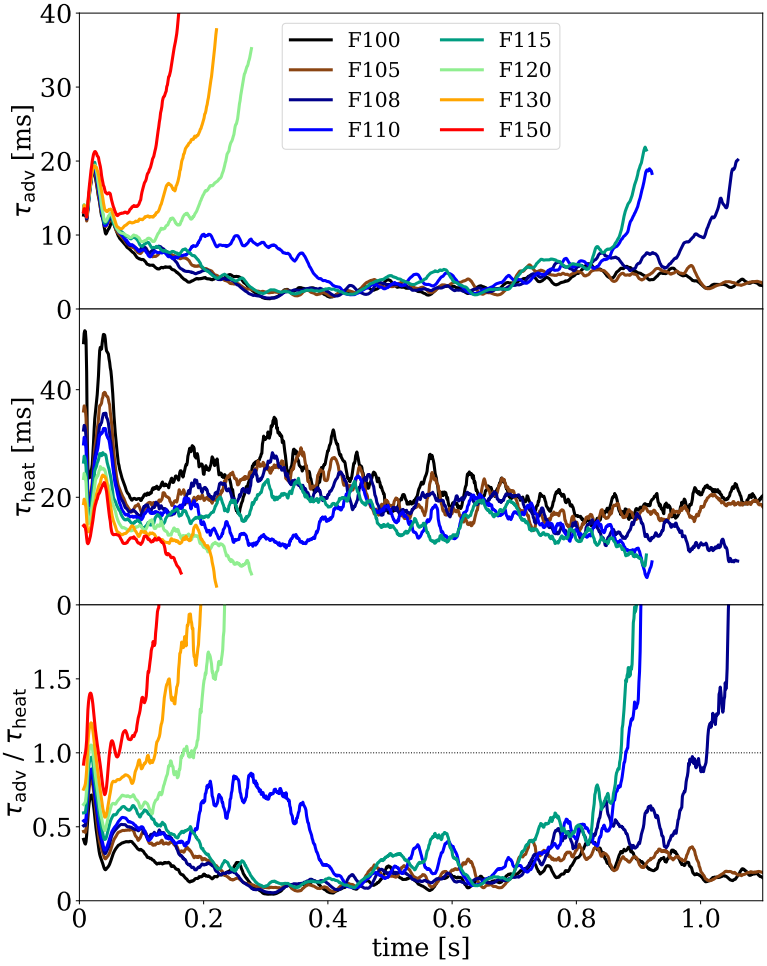

Figure 4.9.: From top to bottom: Timescales of advection, heating and the ratio of both. The dotted horizontal line in the third panel marks where the ratio exceeds 1, signifying favorable conditions for shock revival. The timescales are calculated up to $t = t_{\mathrm{exp}}$ for each model. All curves are smoothed with running averages of 5 ms time windows.

The advection timescale shows similar trends as the shock radius, as it is proportional to the mass in the gain region. Exploding models have an increased τ_{adv} because both the gain region increases and the mass accretion decreases as soon as the shock reaches 500 km. The heating timescale exhibits less drastic changes shortly before an explosion, but generally decreases a bit because the expansion leads to cooling and a loss of internal energy in the gain region. The heating factor enters in the term for $\dot{Q}_{\mathrm{heat}}$ and therefore directly influences τ_{heat}. The ratio of these timescales provides a measure of how fast matter can be heated during its dwell time in the gain region. For values $\tau_{\mathrm{adv}}/\tau_{\mathrm{heat}} > 1$, the neutrino energy deposition rate is enough to push the shock outwards against the infalling matter. Shortly after bounce, all simulations exhibit a local maximum which is related to the neutrino burst. With the heating factor we can push this maximum above 1 for $f_{\mathrm{heat}} \geq 1.20$, i.e., in models of the early explosion category.

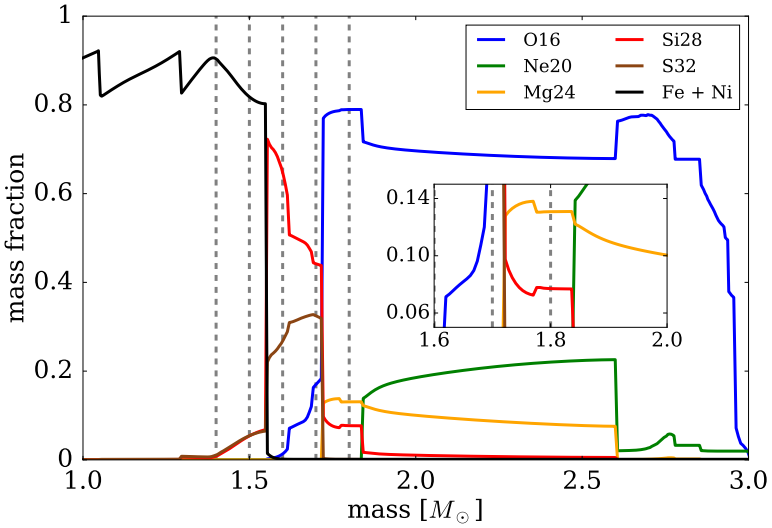

Figure 4.10.: Shell structure (nuclear mass fraction over enclosed mass) with selected isotopes of the "s15.0" progenitor star from Ref. [37]. The "iron core" (black line) is the sum of all iron and nickel isotopes. The dashed gray lines indicate mass shells of the same masses as in Fig. 4.8. The inset plot highlights the region where the shock revival of the late exploding models sets in.

The second group of models with late explosions behaves similar to the non-exploding ones. This provides some hints about these explosions. The shock radius and timescale

ratio (Fig. 4.8 & 4.9) increase after $t \approx 0.7$ s for all models that have not exploded yet. However, the neutrino luminosities do not change significantly during this time. We therefore investigate the structure of the progenitor star as a possible reason for the increasing shock radius. We show the shell structure of the progenitor star in Fig. 4.10 and overplot the same mass shells as in Fig. 4.8 for comparison.

We can identify two major shell interfaces that are accreted onto the PNS within the explosion phase, namely the Fe/Si interface at $M \approx 1.55\ M_\odot$ and the Si/O interface at $M \approx 1.72\ M_\odot$. According to Fig. 4.8, they pass through the shock of the yet not exploded models around $t = 0.2$ s and $t = 0.5$ s, respectively. However, the second shell interface is followed by a small drop in the density of the infalling matter (Fig. 4.11). The increase in shock radius and timescale ratio occurs around the infall time of the $M \approx 1.78\ M_\odot$ mass shell. This is coincident with a change in the mass fractions of Mg and Si, which we show in the inset plot of Fig. 4.10, and an increase in entropy of the accreted matter (Fig. 4.11).

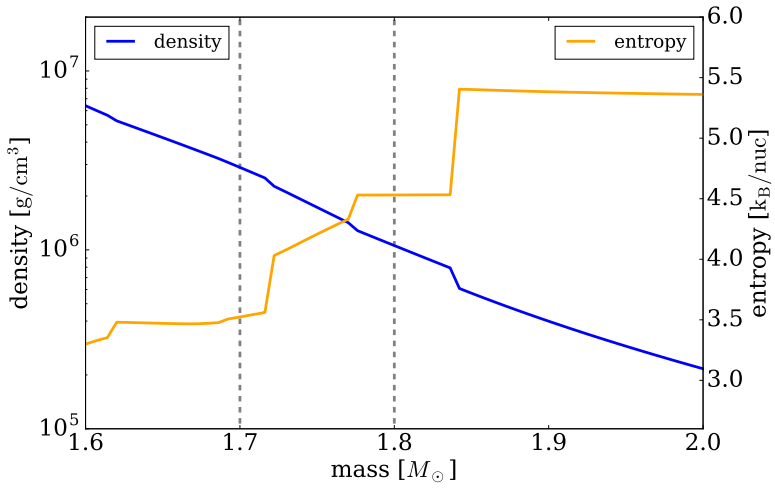

Figure 4.11.: Density (blue, left axis) and entropy (orange, right axis) profiles of the "s15.0" progenitor star from Ref. [37]. The dashed gray lines correspond to the $1.7\ M_\odot$ and $1.8\ M_\odot$ mass shells in Fig. 4.8.

We investigate the impact of this density drop by calculating the pressure on the shock front both from the inside and the outside (ram pressure). Following a similar approach as in Ref. [31] (but neglecting turbulence pressure), we calculate the total pressure on

the shock front as the sum of a ram pressure term and the fluid pressure via

$$P_{\mathrm{tot}} \;=\; \rho \cdot u_{\mathrm{r}}^2 + P_{\mathrm{fluid}}\,, \tag{4.7}$$

where u_{r} is the scalar velocity component perpendicular to the shock front. We approximate u_{r} as the radial velocity, as the shape of the stalled shock is roughly spherical. We evaluate equation (4.7) both closely before and after the shock, while a higher contribution from inside the shock (post-shock) than from outside (pre-shock) signifies favorable conditions for its revival.

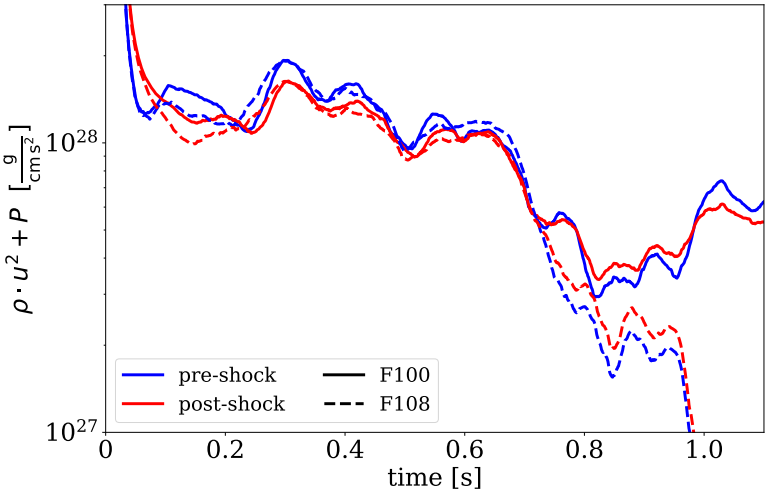

Figure 4.12.: Total pressure on the shock front from both inside and outside according to equation (4.7) for the simulations F100 and F108. The curves are smoothed with running averages of 25 ms time windows, as both the shock position and the local pressure and density are subject to fast changes.

In Fig. 4.12, we show the results for the non-exploding reference case F100 and for the late exploding model F108. The total pressure from the inside dominates up to $t \approx 0.1$ s after bounce, corresponding to the initial shock expansion. When the shock stalls, the ram pressure from outside becomes the dominant component for the subsequent 600 ms. After $t \approx 0.7$ s, both components drop as a result of the density and pressure drop in the progenitor structure. This leads to a period of time where the outwards directed pressure exceeds that of the infalling matter. In the non-exploding case this happens in the time interval $0.8\,\mathrm{s} < t < 1.0\,\mathrm{s}$, and corresponds to the phase where the shock radius

increases above 100 km. For model F108 this possible explosion window is enough to revive the shock. Here, the pressure from inside the shock exceeds that of the outside by up to 30 %. The total pressure from both sides decreases greatly before the actual explosion time (1.07 s), since the shock expands into the lower-density regions a few hundred kilometers away from the PNS. We conclude that the progenitor structure and the accretion of shell interfaces plays an important role in the explosion behavior. This is in agreement with previous studies with different simulation setups and progenitors that highlight the importance of the Si/O interface for the explosion [130, 140–145].

Neutrino characteristics

The heating factor affects the neutrino luminosities until we decrease it after shock revival. A higher heating factor increases the energy deposition rate and therefore reduces the neutrino flux for an observer at infinity. The peak luminosity of the neutrino burst decreases linearly with f_{heat}. In the standard case with no additional heating, the neutrino burst peaks at a value of $2.6 \cdot 10^{53}$ erg/s, while in the model with the highest heating factor, F150, this is reduced to $2.4 \cdot 10^{53}$ erg/s. We note that this is a consequence of the increased absorption in regions with a positive net neutrino heating. At the time of the neutrino burst, there is a few kilometers wide region between the neutrinosphere and the shock, where $Q_{\mathrm{heat}} - Q_{\mathrm{cool}} > 0$ and the heating factor is applied. If measured at the neutrinosphere, the luminosities are similar for all heating factors.

Additionally to this direct influence on the luminosities, the heating factor acts also indirectly on them in the subsequent evolution. The larger shock radius in models with higher f_{heat} (Fig. 4.8) reduces accretion onto the PNS and thus limits accretion luminosity. We show the evolution of electron neutrino and antineutrino luminosities in Fig. 4.13. After the initial burst, the electron neutrino luminosity drops to $5.0 - 5.5 \cdot 10^{52}$ erg/s by the time of shock stalling, and subsequently decreases with further cooling of the PNS. The luminosity of the electron antineutrinos increases up to around $8 \cdot 10^{52}$ erg/s at 100 ms after bounce, before decreasing in a similar trend as that of the electron neutrinos. In the early exploding models, the lack of accretion luminosity is noticeable especially after shock revival. The late exploding models show a similar trend as the failed models F100 and F105.

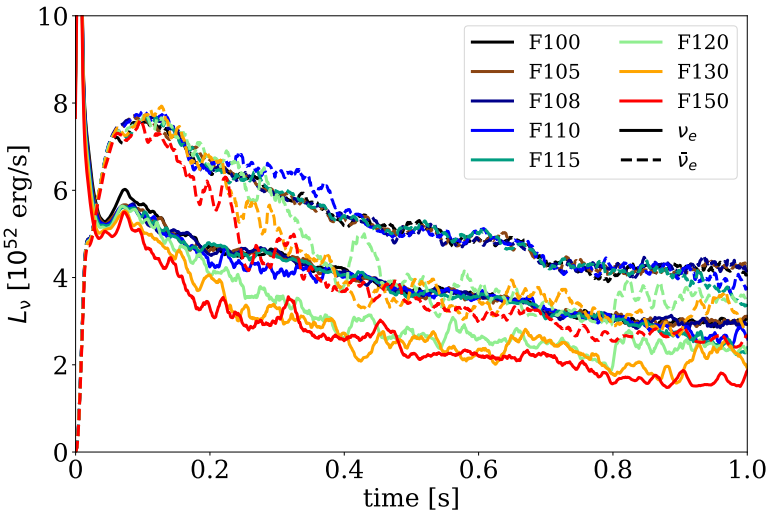

Figure 4.13.: Energy luminosities of electron neutrinos (solid lines) and electron antineutrinos (dashed lines) during the first second after bounce.

After about 200 ms, a ratio of the luminosities of $L_{\bar{\nu}_e}/L_{\nu_e} \approx 1.3 - 1.4$ establishes for the simulations before shock revival. This ratio increases further after a successful explosion to values around $L_{\bar{\nu}_e}/L_{\nu_e} \approx 1.5 - 1.8$. The electron fraction of the early ejecta during the first few hundred milliseconds after shock revival is on average $Y_e \approx 0.44 - 0.46$, with entropies of $s \approx 16 - 18\,k_B/\mathrm{nuc}$.

We can compare the neutrino quantities to the study in Ref. [146], which also uses the FLASH code in 2D and the LS220 equation of state, paired with a $15\ M_\odot$ progenitor (although from Woosley & Heger (2007) [147] instead of this study's progenitor from Woosley et al. (2002) [37]). The main difference to the setup presented here is the use of an effective general relativistic potential and the more sophisticated M1 neutrino transport scheme, instead of the gray neutrino leakage scheme. The evolution of the electron neutrino luminosity is comparable, with values of $L_{\nu_e} \approx 5 \cdot 10^{52}$ erg/s after the neutrino burst and a subsequent decrease to $L_{\nu_e} \approx 3 \cdot 10^{52}$ erg/s in the first second after bounce. However, there are major differences in the values for the electron antineutrinos. While in Ref. [146] both luminosities are quantitatively similar, we see from Fig. 4.13 that the antineutrino luminosities of the gray leakage are substantially higher. This large difference is also responsible for the highly neutron-rich ejecta in our simulations.

4.2.2. Long-time evolution

After a successful explosion, we continue to run the models F108-F150 until the shock comes close to the domain barrier ($R_{\mathrm{shock,max}} > 0.9 \cdot R_{\mathrm{domain}} = 1.44 \cdot 10^{10}$ cm) or the post-bounce time exceeds 9 s. The multi-dimensional nature of the simulations allows for an anisoptropic shock expansion and different ejecta velocities in different directions. Moreover, asymmetric neutrino emission, PNS movement and non-radial ejecta velocities can lead to large differences between the maximum and average shock radius. A consequence of this is that the hierarchy of the shock position at a given time for two different models might not follow their heating factor hierarchy. Therefore, a simulation with a lower heating factor can have a larger shock radius some seconds after bounce compared to a simulation with a higher heating factor. We show the evolution of maximum and average shock radii for all exploding models in Fig. 4.14. As already seen in Fig. 4.8, the two distinct groups of early and late exploding simulations emerge during the first second after bounce. However, after a few seconds the shock radii of both groups can become similar and by the end of the simulation the early exploding model F130 has the lowest average shock radius. In contrast, the hierarchy of shock radii in simulations in a spherically symmetric geometry strictly follows that of the heating factors, as we could see in 1D test runs with the same neutrino setup.

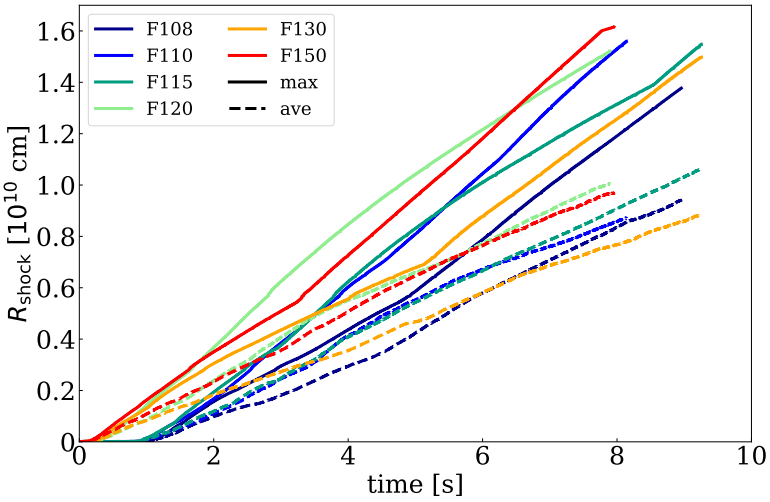

Figure 4.14.: Maximum (solid lines) and average (dashed lines) shock radii for the exploding models over time.

The direction in which the shock preferably expands is important for the long-time evolution of the supernova. An asymmetric explosion might lead to long-lasting downflows from the opposite direction of shock expansion, which in turn influences the matter surrounding the PNS and the neutrino emission. This has consequences for the evolution of the explosion energy and the PNS mass. Accreted matter from downflows is heated to much higher temperatures compared to matter that is ejected with the shock, which influences the nucleosynthesis. We distinguish three categories of possible shock morphologies in a simulation, namely monopolar, bipolar and spherical (isotropic) explosions. Both monopolar and bipolar explosions typically show long-lasting downflows from either the equatorial plane (bipolar) or the south or north pole direction (monopolar). Models with long-lasting downflows typically have a larger remnant mass, larger luminosities and a higher explosion energy. In contrast, spherical explosions usually feature only weak downflows and have a higher possibility to form a neutrino-driven wind (NDW), which results in a smaller PNS mass, smaller luminosities and a rather slowly growing explosion energy. Additionally, the strength and duration of downflows also influences the amount and nucleosynthesis of ejected matter. In the following, we show a representative case for both a monopolar explosion with long-lasting downflows and a spherical explosion and compare some basic features.

We choose the models F108 and F130 as they are representatives of monopolar and spherical explosions, respectively. The plots displayed in Fig. 4.15 show 2D snapshots of the innermost 8000 km for both simulations, taken at the same time at $t = 6.7$ s after bounce. We plot the entropy and the radial fluid velocity in units of the speed of light in the upper and lower half domain, respectively. For the fluid velocity, gray colors indicate negative values and therefore correspond to downflows, while red colors signify positive values, i.e., ejected matter. At this point in the simulation, model F130 features an isotropic NDW. By using the criterion to define a wind phase whenever the accretion rate through a sphere of 500 km around the PNS is zero ($\dot{M}_{\mathrm{acc,500km}} = 0$), this is the only NDW we see in non-rotating models. The wind phase displayed in Fig. 4.15 starts at $t = 6.23$ s and lasts for 1.74 s until the wind collapses because of strong downflows. The wind reaches its maximum size around $t = 7$ s after bounce, when the mean radius of the wind termination shock extends to about 3000 km. In the subsequent second, accretion of matter from the outer layers presses on the wind termination shock front and causes it to decrease in size. Eventually, the downflows reach the PNS and the wind collapses. At the time displayed in Fig. 4.15, the NDW is highly supersonic with radial velocities exceeding the local speed of sound by up to a factor of 5. The matter properties in this phase are determined by the neutrino-driven ejection only and are independent from the influence of downflows. As a consequence of this, the electron fraction within the wind drops to

very neutron-rich values of $Y_e \approx 0.35$. It shall be noted that these extremely neutron rich conditions are a consequence of our gray neutrino leakage scheme. Simulations with more sophisticated neutrino transport methods predict a much higher electron fraction, even up to the proton-rich regime [35].

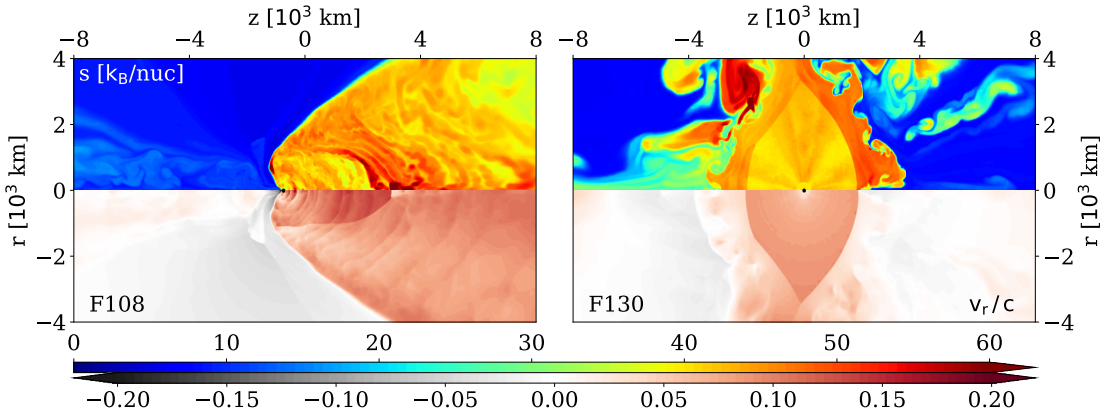

Figure 4.15.: Snapshots of the models F108 (left) and F130 (right) at $t = 6.7$ s after bounce. The upper half of the domain shows the entropy and the lower one the radial velocity in units of the speed of light. The upper and lower colorbars correspond to entropy and radial velocity, respectively. The black dot near the center represents the PNS.

In contrast, model F108 shows a very different picture at the same time. Here, a strong downflow from the left polar direction occurs, while ejection of matter takes place in the opposite direction. The continued accretion adds to the mass of the PNS, which at that time has reached $2.14\,M_\odot$ and keeps on growing, while the PNS in the case of F130 has a saturated mass of $1.76\,M_\odot$. The impact of the lack of accretion luminosity in model F130 can be seen in Fig. 4.16, where we show the angle-averaged values for both electron neutrinos and antineutrinos. After about 2 s, the ejection of matter in model F130 outgrows the accretion so that almost all of the radiated neutrinos originate from the PNS instead of from accretion luminositiy. The luminosities then stabilize at values of $1.1 \cdot 10^{52}$ erg/s and $2.1 \cdot 10^{52}$ erg/s for electron neutrinos and antineutrinos, respectively. In comparison to model F108, where accretion luminosity contributes, the mean luminosities (taken during the wind phase of model F130) are reduced by 37 % (ν_e) and 25 % ($\bar{\nu}_e$). In the direction of the downflow in model F108, the reduction is even higher with 65 % (ν_e) and 49 % ($\bar{\nu}_e$), which highlights the impact of accretion luminosity at late times.

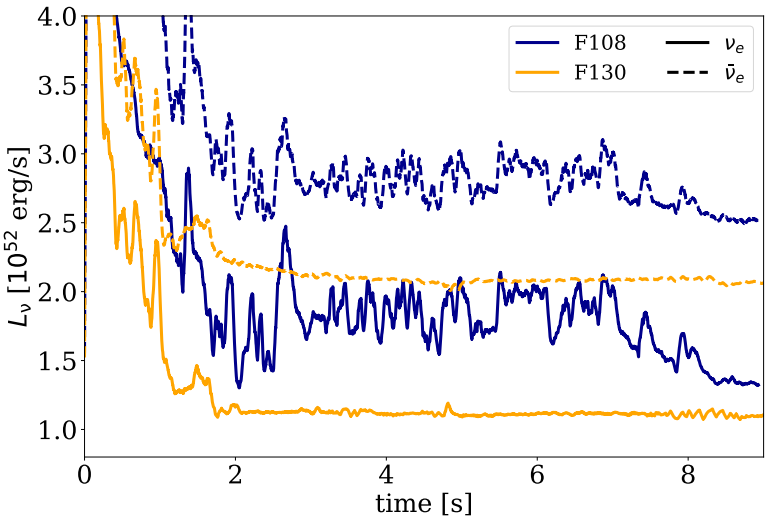

Figure 4.16.: Angle-averaged luminosities of electron neutrinos (solid lines) and antineutrinos (dashed lines) over time for the models in Fig. 4.15.

Explosion energy

The interplay of post-explosion accretion and ejection largely determines the growth rate of the explosion energy at late times. After shock revival, the explosion energy initially seems to saturate (Fig. 4.7), but with the onset of strong downflows it increases again, although at a much lower rate than in the first 100 ms after $t_{\rm exp}$. The time at which $E_{\rm dia}$ saturates and its final value have been under discussion for a long time, yet most studies do not reach the point of this saturation (e.g., see Ref. [146, 148–150]). Studies by Bruenn et al. [148, 149] also take the outer shells of the progenitor into account that the shock has to overcome for a successful breakout, otherwise the explosion material can still fall back onto the PNS to form a black hole. Because we perform long-time simulations in a large domain, this "overburden" energy is typically $\ll 0.1$ B in our case at the end of each model and we therefore neglect it in further considerations. We see that the explosion energy crucially depends on the post-explosion evolution and that the long-time behavior generally has to be taken into account for its final value. The evolution of $E_{\rm dia}$, as calculated from equation (4.3), is displayed in Fig. 4.17. All models exhibit a growth in the explosion energy until the end of the simulation while the hierarchy, likewise to the evolution of the shock radius, does not follow the heating factor hierarchy. Model F110 comes out with the highest explosion energy, while model F130 has the lowest. These

two simulations are also the ones with the lowest ratio (0.29) and highest ratio (0.44) of the shock radius in the equatorial direction divided by the maximum shock radius, respectively. This highlights the importance of the shock morphology and its effect on the explosion energy through large-scale downflows, which are persistent throughout the simulation for all models with generally high explosion energies. Occasional kinks in the evolution of E_{dia} are caused by sudden changes in the accretion/ejection configuration near the PNS, when for example a new downflow comes close to the PNS, shifts its direction of the funnel or is expelled by ejected matter. In all of these cases, large amounts of newly heated matter leave the vicinity of the PNS and contribute to the explosion energy.

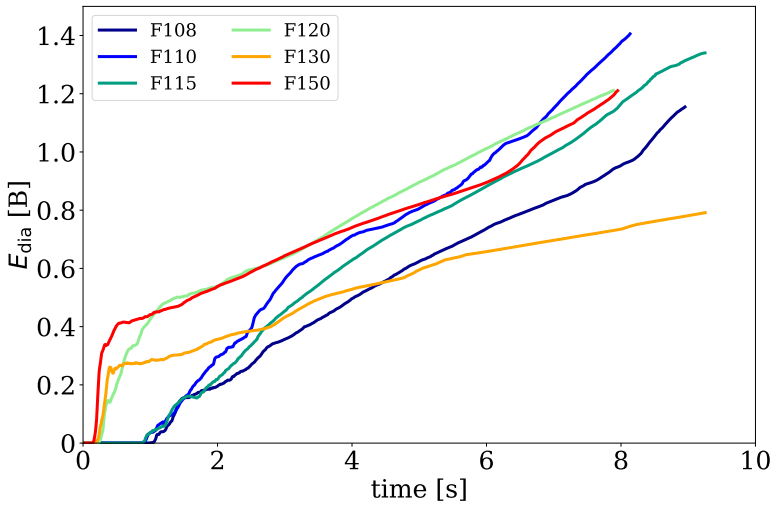

Figure 4.17.: Diagnostic explosion energies over time for all exploding models.

Even in the absence of accretion as during the wind phase in model F130, the explosion energy still keeps on growing. We can attribute this to ejection of PNS matter during the wind. Typically, this matter was exposed to neutrinos for a long time in the PNS and is ejected with high entropies, it therefore has a higher total energy per mass compared to the average of ejected matter. The PNS mass in model F130 decreases from its maximum value of $1.77\,M_{\odot}$ to $1.75\,M_{\odot}$ at the end of the simulation, with a rate of $-2.7 \cdot 10^{-3}\,M_{\odot}/\mathrm{s}$. Meanwhile, the explosion energy increases at an almost constant rate of 0.04 B/s as a result of this wind contribution. In comparison to the steep increase after the initial explosion of 0.15 B during just 0.1 s (see Tab. 4.1) this is not much, but during a long-

time simulation can add up to several tens of Bethe. We will elaborate more on how the explosion energy growth depends on mass accretion and wind phases in the next chapter.

5. Rotation in core-collapse supernovae

In this chapter, we discuss the effect that rotation has on a core-collapse supernova (CCSN). There is an ongoing discussion about whether rotation is advantageous or disadvantageous for shock revival and how it impacts the long-time evolution. Numerous studies in the last decades have pointed to a variety of possible effects emerging from rotation (e.g., see Ref. [30, 35, 64, 127, 129–131, 139, 151–154]). We explore this question in our framework of long-time 2D simulations with variable heating factors with the same setup as described in chapter 4. Additionally to the eight non-rotating models calculated there, we now expand our parameter space with a variable angular momentum profile of the progenitor and use this to calculate rotating counterparts of the same models as described before. After introducing and categorizing the considered rotation strengths, we explore their effect on both the explosion phase and the long-time evolution, with special focus on explodability and the impact on neutrino-driven winds (NDW).

5.1. Model overview

We investigate the effect of rotation in CCSN by imposing an artificial rotational profile on our non-rotating progenitor model. We use the radius-dependent angular velocity profile defined by equation (3.31), with a fixed value for the characteristic radius of $r_A = 3000$ km. The parameter Ω_0, which corresponds to the angular velocity at the center of the star, then allows us to tweak the rotation of the progenitor star. For $r \to \infty$, the specific angular momentum approaches the constant value of $j(r = \infty) = \Omega_0 \cdot r_A^2$. Because we use the same progenitor for all simulations, we can calculate the total angular momentum within our domain to be $J_{\mathrm{tot}} = \Omega_0 \cdot 2.55 \cdot 10^{50}\,\mathrm{g\,cm^2}$.

We consider a total of six different values for Ω_0 on top of the non-rotating case (Tab. 5.1). For convenience, we give all values in units of 2π rad/s. In the following, we label models as before with the heating factor classification, but now also add a label indicating the rotation. For example, the label F130_R006 refers to a model with $f_{\mathrm{heat}} = 1.3$ and $\Omega_0 = 0.06 \cdot 2\pi$ rad/s. Following previous studies and results from stellar evolution calculations (e.g., see Ref. [153, 155, 156]), we divide our rotating models into two classes, namely moderately rotating (i.e., resembling stellar evolution rotational frequencies) and rapidly rotating models. We consider models with $\Omega_0 \,/\, (2\pi\,\mathrm{rad/s}) \in \{0.01, 0.03, 0.06\}$ to belong to the first, and those with $\Omega_0 \,/\, (2\pi\,\mathrm{rad/s}) \in \{0.10, 0.20, 0.30\}$ to belong to the second group. The inclusion of rotational frequencies that exceed the values suggested by stellar evolution calculations allows us to investigate the effects of rotation in a broader parameter study.

	no rotation	moderate rotation			rapid rotation		
Ω_0 [2π rad/s]	0.00	0.01	0.03	0.06	0.10	0.20	0.30
name	R000	R001	R003	R006	R010	R020	R030

Table 5.1.: Considered values for Ω_0 in the rotation law of equation (3.31) with their classifications and labels.

5.2. Collapse phase

During collapse, the conservation of angular momentum leads to a spin-up of the center of the star. The contraction of the rigidly rotating iron core and the further accretion of matter with angular momentum increases the rotational frequency by several orders of magnitude. We show this in Fig. 5.1, where the "pre-collapse" line corresponds to the initial profile imposed by equation (3.31), and the "bounce" line is taken right before bounce (after a simulation time of 286 ms). Both lines show the angular velocity Ω as a function of the radius for a model with $\Omega_0 = 0.20 \cdot 2\pi$ rad/s (R020). As we switch on the neutrino leakage only after bounce, this is independent of the heating factor. During this time, the innermost few thousand kilometers collapse to less than a hundred kilometers, increasing the angular velocity in the center by a factor of ≈ 250.

Rotation affects the hydrodynamic flows through centrifugal forces. This additional force component pushes matter away from the rotational axis, which is in our geometry identical with the cylindrical axis. During collapse, this slows down the gravitational acceler-

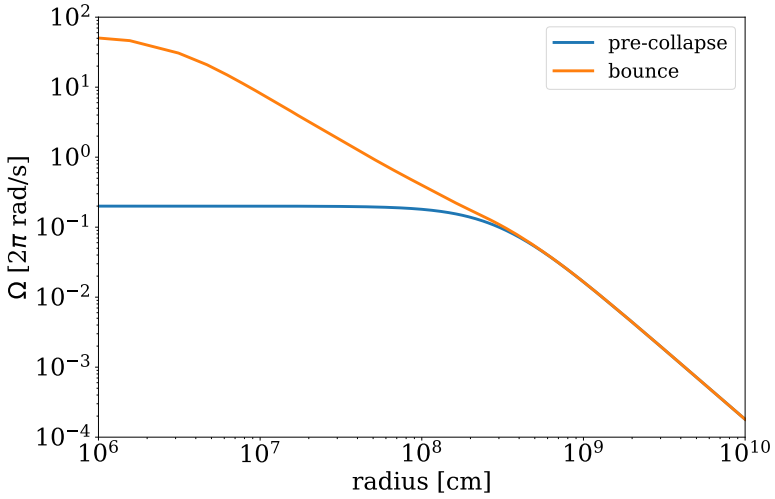

Figure 5.1.: Rotational profile (angular velocity vs. radius) at the beginning of the simulation (blue) and right before bounce (orange) for a R020 model.

ation of matter towards the center of the star, which leads to smaller infall velocities and can delay the time of bounce. In our models, we can see that core bounce occurs up to 1 ms later for the most rapidly rotating case R030, compared to the non-rotating counterpart. Similarly, the smaller infall velocities also translate to a smaller mass accretion rate in the collapse phase. By the time of bounce, we can see a deficit in the sum of the accreted mass of up to $4 \cdot 10^{-3}\ M_\odot$, again for the most rapidly rotating case. We will see later that this effect has consequences not only during collapse, but also for the explosion phase and the long-time evolution.

5.3. Explosion phase

After bounce, the effects of rotation on the stalled shock, the downflows, and the neutrino emission can play an important role for shock revival. Continued accretion of matter with angular momentum and the contraction of the proto-neutron star (PNS) cause it to spin-up further with time. Simultaneously, matter from the outer layers experiences increasing centrifugal forces as it moves from larger to smaller radii and approaches the shock front.

We can see a redistribution of the local matter density as a consequence of this effect in our models, which we display in Fig. 5.2. Here, we compare a rapidly rotating R020 model with its non-rotating R000 counterpart and show the relative change in the local matter density. The values have been interpolated to the respective bounce times. The red areas indicate an increased density in the presence of rotation, while blue parts have a density deficit. As the rotation axis is equivalent to the horizontal z-axis in the plot, the vector of the centrifugal force points towards positive values of the vertically displayed r-coordinate. This additional force component shifts matter away from the rotational axis. The effect can be best explained by looking at progenitor matter that initially lies in the polar directions ($|z| \gg 0$, $r \gtrsim 0$), which is accelerated to positive r-values as it approaches the center of the star (later the PNS) and therefore does not end up exactly at the poles of the PNS, but slightly more towards the equatorial plane. Consequently, the density at the poles of the PNS is reduced for rotating models. As there are no other non-radial forces before bounce, this has a considerable effect even for the moderately rotating models with lower angular momentum.

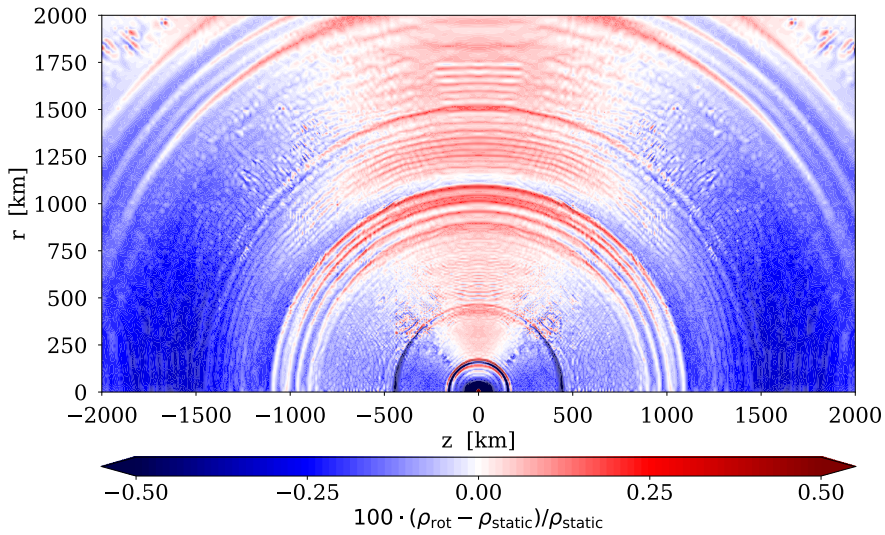

Figure 5.2.: Changes in the local matter density at bounce because of centrifugal forces. Red and blue areas indicate increased and decreased densities, respectively. The values are given in percentage of relative change for a R020 model compared to the non-rotating R000 case.

The reduced matter density at the poles for rotating models has direct consequences for the neutrino emission [139]. A considerable fraction of neutrinos originates from accretion luminosity, which is proportional to the local density at the emission points. We show the neutrino luminosities during the first second after bounce in three different directions (north pole, south pole and equatorial plane), in Fig. 5.3. The line colors correspond to different variations of the initial rotation period (non-rotating, moderately and rapidly rotating) and we show the luminosity for two different heating factors ($f_{\mathrm{heat}} = 1.3$ and 1.5) to prove the robustness of the results.

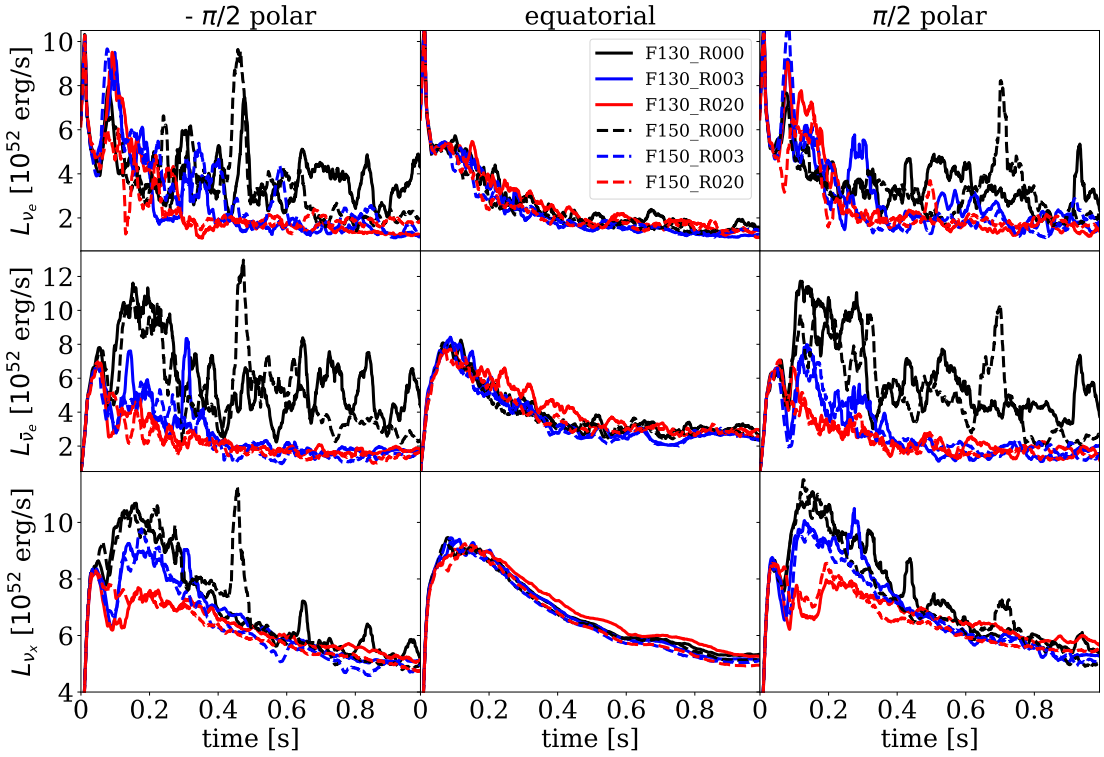

Figure 5.3.: Neutrino luminosities for non-rotating (black), moderately (blue) and rapidly rotating (red) models of two different heating factors as seen from an observer in the direction of the poles (left and right panels) or the equatorial plane (center panels). The different rows show the luminosity for the different neutrino flavors, for electron neutrinos (top), antineutrinos (middle) and heavy-lepton neutrinos (bottom). Note the different scalings on the y-axes.

In the direction of the poles, the luminosity is reduced for rotating models. The effect is most pronounced for the electron antineutrino luminosity and we discuss some key features of it in the following. While the non-rotating configuration exhibits peak values of around $12 \cdot 10^{52}$ erg/s and usually stays above $4 \cdot 10^{52}$ erg/s after that, the presence of rotation reduces the peak luminosity to $\approx 8 \cdot 10^{52}$ erg/s with values around $2 \cdot 10^{52}$ erg/s at later times. This significant reduction is the lack of accretion luminosity at the poles because of the redistribution of accreted matter as displayed in Fig. 5.2. In 2D simulations, this is a well-known effect (e.g., see Ref. [64, 127, 139, 152]), while in 3D the angular dependence is not as prominent, yet the total luminosities are reduced as well in rapidly rotating models [130]. When increasing the rotation from the moderate to the rapid regime, a further reduction, especially during the first 400 ms, takes place. However, we see a saturating behavior of this effect, as the differences towards faster rotating models up to R030 become smaller.

In the direction of the equatorial plane, the situation is different. Here, we see no significant change in the luminosity due to the presence of rotation. One might expect an increased luminosity from Fig. 5.2, because also the matter density is increased at the equator of the PNS. However, the progenitor material that drifts from the poles to the equator has a small radial component in the velocity and usually passes by the PNS closely, but comes not as close as the infalling matter from the equatorial plane. It thus does not become as hot and provides only a small contribution to the accretion luminosity.

The integral value of the luminosity, i.e., the sum of the contributions from all angles, is therefore also reduced. Depending on the rotation strength and considered heating factor, the total energy carried away by the leakage electron antineutrinos during the first second after bounce is reduced by up to 15 % compared to the non-rotating case. This has considerable consequences for the explodability of rotating models. On the one hand, the reduced matter density around the PNS lowers the ram pressure on the stalled shock, but the lack of accretion luminosity takes away the energy support for shock revival (similar to, e.g., Ref. [139]). In our simulations, we see that the overall effect that rotation has on the stalled shock is negative, as it can delay the explosion time or even prevent shock revival altogether. While the change in the ram pressure, which is proportional to the density, is at the order of 1 %, the energy deposition by neutrinos is reduced by a larger value (because of the reduced luminosity), which explains the overall detrimental effect on shock revival.

We summarize the explosion behavior of models with different heating factors and varying strength of rotation by showing the explosion times of all exploded models in Fig. 5.4. The rows correspond to the heating factors (for all simulations with $f_{\mathrm{heat}} \geq 1.08$) and the

columns to the imposed rotation strengths (Ω_0 in units of 2π rad/s). Explosion times are given in seconds within the respective cells and are also color-coded (green for early and yellow for late exploding models), while the cells for non-exploding simulations are shown in black. The first column ($\Omega_0 = 0$) is identical with the values displayed in Tab. 4.1.

As a general picture, we see that imposing rotation on the progenitor can delay or even prevent shock revival. For late exploding simulations with shock revival only after the passing of the Si/O interface (F108, F110 and F115), no rotating models show a successful explosion. The reduction of the neutrino luminosity is already significant for the slowest rotation R001, so that neutrinos do not provide a sufficient amount of energy for the stalled shock. Until the time of shock revival in the non-rotating models ($t_{\rm exp} \approx 1$ s), the continued spin-up of the PNS and its surroundings amplifies this effect even more.

heating factor	$t_{\rm exp}$ [s] \ Ω_0 [2π rad/s]	0.00	0.01	0.03	0.06	0.10	0.20	0.30
1.08		1.07	no explosion					
1.10		0.93						
1.15		0.92						
1.20		0.28	0.30	0.36	0.38			
1.30		0.23	0.22	0.23	0.24	0.28	0.32	0.36
1.50		0.17	0.17	0.21	0.17	0.21	0.22	0.21

Figure 5.4.: Table with the explosion time in seconds for all models with $f_{\rm heat} \geq 1.08$. The different heating factors are displayed vertically and the rotation strengths (Ω_0 in units of 2π rad/s) horizontally. Black cells indicate a failed shock revival in these models.

Increasing the heating factor further eventually leads to successfully exploding models with rotation. For $f_{\rm heat} = 1.20$, simulations with moderate rotation revive the shock, although at considerably later times than in the non-rotating case. The enhanced effect of rotation in the rapidly rotating models ($\Omega_0 \geq 0.10 \cdot 2\pi$ rad/s) can still prevent the explosion. We obtain successful explosions in rapidly rotating models only for $f_{\rm heat} \geq 1.30$. However, shock revival is significantly delayed in these cases. There are no late explosions (i.e., shock revival after the passing of the Si/O interface) for rapidly rotating models. We

attribute this to the increased angular velocity at late times due to contraction and spin-up of the PNS, and the likewise increased effect on the neutrino emission at the infall time of the shell interface.

5.4. Long-time evolution

Rotation plays an important role in the long-time evolution of the explosion. Continued accretion and PNS contraction lead to a further spin-up for seconds and an increased imprint on the neutrino emission. The interplay of matter ejection and downflows plays an important role for the evolution of the explosion energy and the PNS mass, as already discussed in chapter 4. Both are affected by the increasing centrifugal forces, which especially impact accretion from the equatorial plane.

When the stalled shock is revived, a large amount of matter is ejected with it. In the case of an anisotropic shock expansion, accretion still takes place from regions that are less powerfully accelerated at revival. The initial expansion direction of the shock therefore determines the accretion and the behavior of downflows at later times. We discuss the early shock morphology as an indicator for the long-time evolution and show that rotation plays a crucial role for this. As a measurable quantity for how spherical, oblate or prolate a shock front is, we use the shock deformation parameter introduced by Scheck et al. (2006) [157]. It uses the shock radius R_s as a function of the polar angle θ and is given by

$$d_\mathrm{shock} = \frac{\max[R_\mathrm{s}(\theta)\cos(\theta)] - \min[R_\mathrm{s}(\theta)\cos(\theta)]}{2 \cdot \max[R_\mathrm{s}(\theta)\sin(\theta)]} - 1\,. \tag{5.1}$$

The parameter is equivalent to the ratio of the maximum shock diameters parallel and perpendicular to the cylindrical axis. It can have positive and negative values, for a prolate and an oblate shock deformation, respectively. In the case of a spherical shock expansion, d_shock becomes zero.

We show the evolution of the shock deformation parameter during the first two seconds of the simulation in Fig. 5.5. We use similar linestyles and colors as in Fig. 5.3, but instead of only showing two representative rotation strengths (apart from the non-rotating one), we summarize all moderately rotating (R001, R003, R006) and rapidly rotating (R010, R020, R030) cases by taking their mean values.

Shortly after bounce, the shock expands in a spherical shape. By the time of explosion ($t = t_\mathrm{exp}$), the non-rotating models show a strong prolate deformation ($d_\mathrm{shock} = 0.59$ and

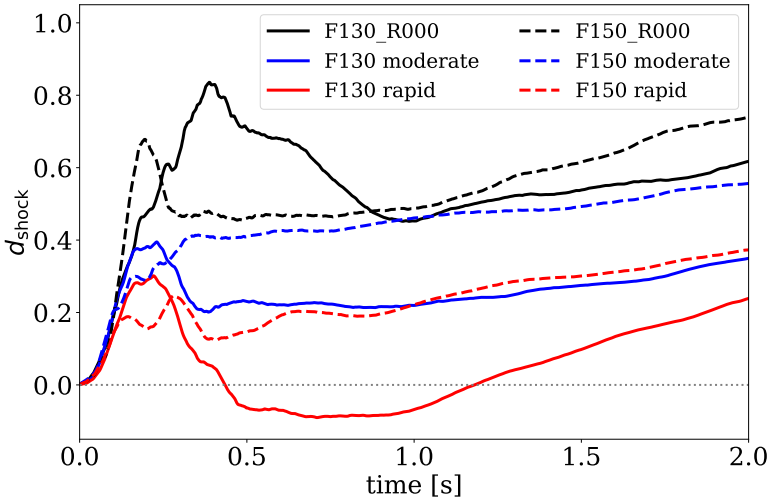

Figure 5.5.: The shock deformation parameter according to equation (5.1) for the first two seconds of models with $f_{\mathrm{heat}} = 1.30$ (solid) and $f_{\mathrm{heat}} = 1.50$ (dashed). The black lines show the non-rotating R000 cases, the blue ones the average of all moderately rotating (R001, R003, R006) and the red ones the average of all rapidly rotating (R010, R020, R030) cases. The dotted gray line indicates where a spherical shock morphology can be found.

0.64 for $f_{\mathrm{heat}} = 1.30$ and 1.50, respectively), since the shock expands in a bipolar fashion towards both polar directions. In contrast to this, the moderately rotating models are much less deformed ($d_{\mathrm{shock}} = 0.33$ and 0.37) and the rapidly rotating models explode almost spherically ($d_{\mathrm{shock}} = 0.02$ and 0.06). The typically prolate shock expansion in non-rotating 2D simulations is a known feature of this geometry, seen for example in Ref. [41, 136, 145, 146, 149, 150]. However, the resulting accretion along preferred directions has also been observed in 3D simulations [76, 158].

In the following seconds, there is a clear correlation of d_{shock} with the rotation strength. Fast rotating models usually show a more spherical shock front, the rapidly rotating cases of the F130 series even show a slightly oblate deformation during $0.4\ \mathrm{s} \leq t \leq 1.2\ \mathrm{s}$. At later times, all models tend to become more prolate which is again a consequence of the cylindrical geometry which favors this shape. However, at these times the shock is too far out to impact the downflows, which is why we focus on the shock morphology only during the first two seconds. Comprehensive studies in 3D that evaluate the impact of rotation at late times and would allow for a more in-depth comparison, are yet not feasible.

5.4.1. Proto-neutron star deformation

The centrifugal forces affect not only the accreted and ejected matter, but also the PNS in the center, which in term has consequences for the neutrino emission at late times. We show the PNS contours (defined at $\rho = 10^{11}$ g/cm^3) of the six different models discussed before, and their deviation from a spherical shape, in Fig. 5.6. Compared to a perfect sphere (dashed orange line in the plot), there are only minor variations in the non-rotating cases, which originate from enhanced ejection or accretion in these regions. By increasing the rotation, the PNS deformation becomes more significant and can lead to several hundred meters (moderate rotation) or even kilometers (rapid rotation) difference when measuring the radius in projection or perpendicular to the rotational axis.

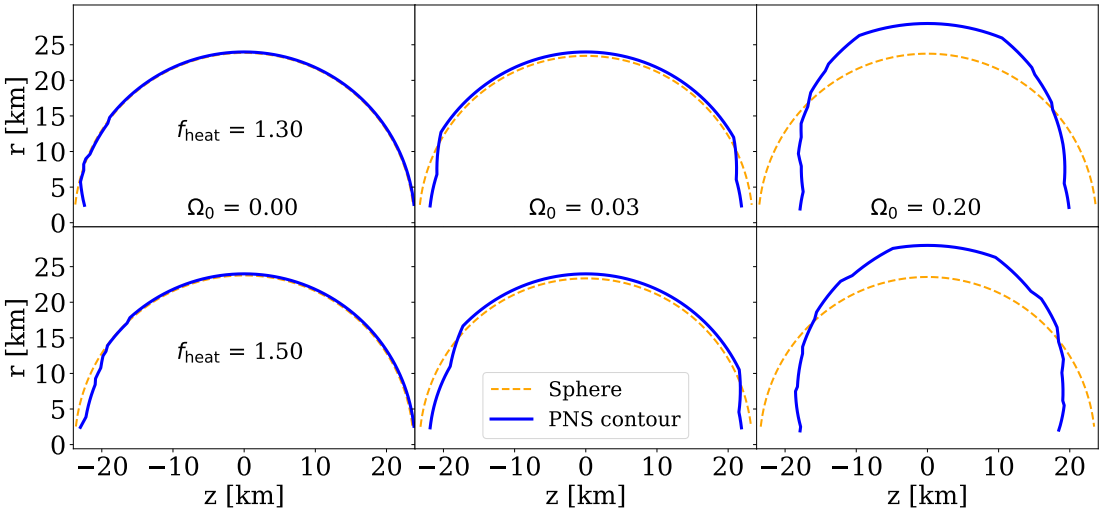

Figure 5.6.: Deformation of the proto-neutron star because of rotation. The panels show the shape of the PNS contour (defined at $\rho = 10^{11}$ g/cm^3, solid blue) relative to a perfectly spherical case of the same mean radius (dashed orange) for each a non-rotating (left), moderately (center) and rapidly rotating (right) case with $f_{\mathrm{heat}} = 1.30$ (top) and 1.50 (bottom) at the end of the simulation.

The deformation of the PNS has consequences for the neutrino emission, as the neutrinospheres follow the shape of the density-defined contour in Fig. 5.6, and a more outwards lying neutrinosphere typically has lower temperatures. When taking the average

neutrino energy along different directions during the last second of the simulation for the most rapidly rotating models F130_R030 and F150_R030, we see differences of several MeV. Specifically, the energy of neutrinos emitted in the direction of the equatorial plane is reduced by $2.1 - 2.8$ MeV (depending on the heating factor and neutrino flavor) compared to the energy of neutrinos emitted at the poles. Because of overall high fluctuations, the difference is only significant for the rapidly rotating models.

5.4.2. Explosion energy

The different shock morphologies in the first seconds as seen in Fig. 5.5 have consequences for the inflow/outflow balance at later times. Typically, more spherically exploding models push more matter in the direction of the equatorial plane, which leads to less and weaker downflows from this region. We see in our simulations with non-rotating progenitors that downflows commonly originate from there, as the shock initially expands mostly in the other directions. As continued accretion is a major energy source for the supernova engine, the long-time evolution must not be neglected when evaluating the explosion energy.

In Fig. 5.7, we show the evolution of E_{dia} for the six models already discussed above. The black lines representing the non-rotating cases are identical to the F130 and F150 labeled lines in Fig. 4.17. The explosion energy is affected both by the heating factor and the rotation strength. We can distinguish the two different heating factors (solid and dashed linestyles) and variations therein because of different rotation strengths with runs of the same heating factor. As a consequence of the increased neutrino heating, the F150 runs have a higher explosion energy than the F130 ones, with a difference already established at the explosion time. Throughout the simulation, the non-rotating and moderately rotating cases have similar explosion energies, while the rapidly rotating models have slightly lower values. This is again a result of the more spherical explosion morphology and the weaker downflows in rapidly rotating models.

In the following, we investigate the growth rate of the explosion energy and why we see no saturating behavior. With the exception of model F150_R000, all simulations shown in Fig. 5.7 form a NDW at some time. Notice that even during these phases, the explosion energy keeps on growing because of the ejected PNS matter. The slope of the explosion energy changes during different phases of the simulation, which can be characterized by their mass accretion rates. We therefore look for a robust pattern that aims to explain the non-existent saturation and whether this is consistent throughout all models. In order to correlate the explosion energy growth rate with the mass accretion rate, we use data

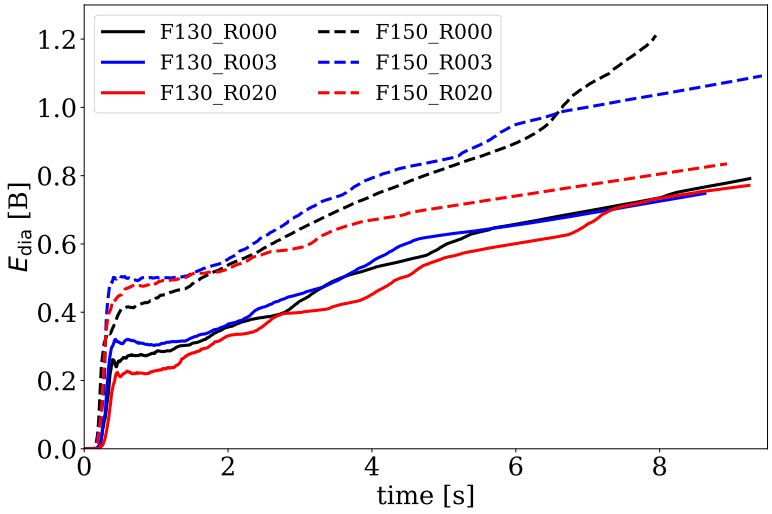

Figure 5.7.: Explosion energy evolution for models of the F130 (solid) and F150 (dashed) series with no rotation (black), moderate (blue) and rapid (red) rotation.

points from all our 21 exploding simulations and put them in a $\dot{M}_{\rm acc} - \dot{E}_{\rm dia}$ plane. This results in a global trend of how accretion powers the explosion energy, indepedent of the heating factor or rotation strength.

We show the result in Fig. 5.8. Here, each gray dot represents a data point (1 ms) from one of the exploding models and the blue line is an interpolation of all these points. As the spread is rather large, especially at higher mass accretion rates, we show the $0.675\,\sigma$ confidence interval which contains 50 % of all points. In agreement with previous studies (e.g., see Ref. [41, 62]), we see an increased growth rate for $E_{\rm dia}$ whenever the mass accretion is large. When we go to phases of less accretion (coincident with later times for some simulations), a saturating behavior sets in which levels the explosion energy growth rate at 0.04 B/s, a value consistent with the slope of the lines in Fig. 4.17 and Fig. 5.7 of models during a NDW phase.

The saturation sets in for $\dot{M}_{\rm acc} \lesssim 2 \cdot 10^{-3}\ M_\odot/{\rm s}$, when the accretion rate decreases to lower values than the matter ejection rate of the PNS during wind phases. The smaller confidence interval towards lower mass accretion rates points to a consistent behavior that is responsible for the continued growth of $E_{\rm dia}$ in some models. We identify this to be the ejection of highly-energetic PNS matter in phases of low accretion. For larger mass accretion rates we also see a larger spread in $\dot{E}_{\rm dia}$ because of the variety of con-

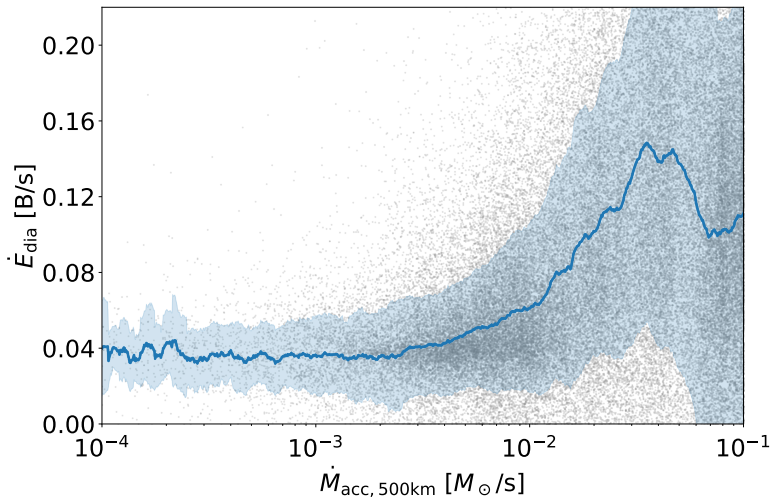

Figure 5.8.: Growth rate of the explosion energy vs. mass accretion rate. The gray dots represent data points from all 21 exploding simulations with one point for each 1 ms simulation time. The blue line is an interpolation of all these points and the blue shaded area the respective $0.675\,\sigma$ confidence interval.

tributing downflows there. With sufficiently high mass accretion rates, which correspond to persistent downflows onto the PNS, the growth rate of the explosion energy increases to $\dot{E}_{\rm dia} \approx 0.12 - 0.16$ B/s. Even higher mass accretion rates (not displayed in the plot) appear shortly after shock revival, where $E_{\rm dia}$ suddenly jumps by up to a few 0.1 B, and therefore the growth rate amounts to several Bethe per second.

5.5. Formation of neutrino-driven winds

In this section, we investigate the occurrence of NDWs in our simulations and its correlation with the rotation strength. The necessary condition for wind formation is the absence of all accretion, $\dot{M}_{\rm acc} = 0$, which we use as a criterion to define wind phases. As discussed in the previous sections, we see that imposing rotation on the progenitor can shift matter from the poles to the equatorial plane. This results in a reduced accretion luminosity at the poles and a more spherical shock morphology at early times. At later times, the centrifugal forces still act on the surrounding matter and actively contribute to pushing downflows away from the PNS.

We quantify the impact of these centrifugal forces on the mass accretion rate by calculating the amount of accreted mass through a sphere at $r = 500$ km around the PNS. The variety of different rotation strengths then allows us to look for a correlation between rotation and the late-time accretion. As the high accretion rates shortly after shock revival overshadow the late-time contribution, we sum the total accretion in a five second time interval ($2.5\ \mathrm{s} < t < 7.5\ \mathrm{s}$) well after shock revival. The results are shown in Fig. 5.9, where we plot the accreted mass in this time interval over the rotation strength. For each Ω_0, we take the mean value of all exploding simulations (evolved to at least $t = 7.5$ s) corresponding to that, while the error bars are due to the several different models per Ω_0. We note that different amounts of models contribute to each data point, for example we have six exploding non-rotating simulations but only two for each of the rapid rotations.

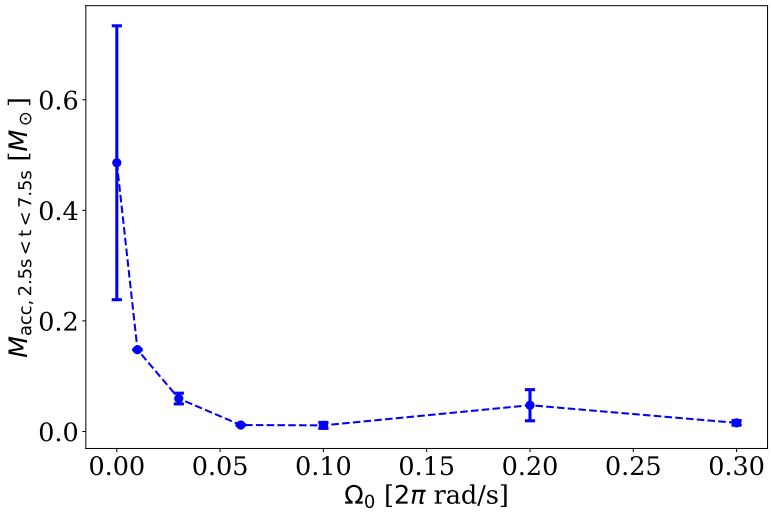

Figure 5.9.: Total mass accreted through a sphere at $r = 500$ km around the PNS for different variations of the rotation strength. We only consider exploding models that are evolved past $t = 7.5$ s. The error bars correspond to the spread because of several models with the same rotation, while the points show the mean values for each variation of Ω_0.

For the non-rotating reference case, the total mass accreted in this time amounts to $(0.49 \pm 0.25)\ M_\odot$. Out of this, $(0.12 \pm 0.07)\ M_\odot$ end up within the PNS and contribute to its mass, while the rest is ejected again after a brief dwell time in the vicinity of the PNS. When introducing rotation, the late-time accretion drops significantly. Already for the slowest rotation strength we see a reduction in the mean accreted mass by 70 %, and a drop of 88 % for models of the R003 series. With the exception of the R020 models, the mass accretion for stronger rotation is reduced by $97 - 98$ %, compared to the non-rotating reference. In the case of F130_R020, a short but massive downflow around $t = 4.5$ s contributes to the data, which results in the higher value for $M_{\rm acc}$ in the plot and is also responsible for the larger error bar, as the accreted mass in the corresponding F150_R020 model is four times smaller and more aligned with those of the R010 and R030 simulations. From Fig. 5.9 we deduce that strong rotation limits the mass accretion also at late times and prevents the occurrence of persistent downflows. As this is a necessary ingredient for the formation of winds, we therefore expect a larger probability for NDWs in rotating simulations. We stress that this result might be sensitive to the simulation dimensionality. While our simulations show this trend in 2D, comprehensive studies on NDWs in 3D are yet to be performed.

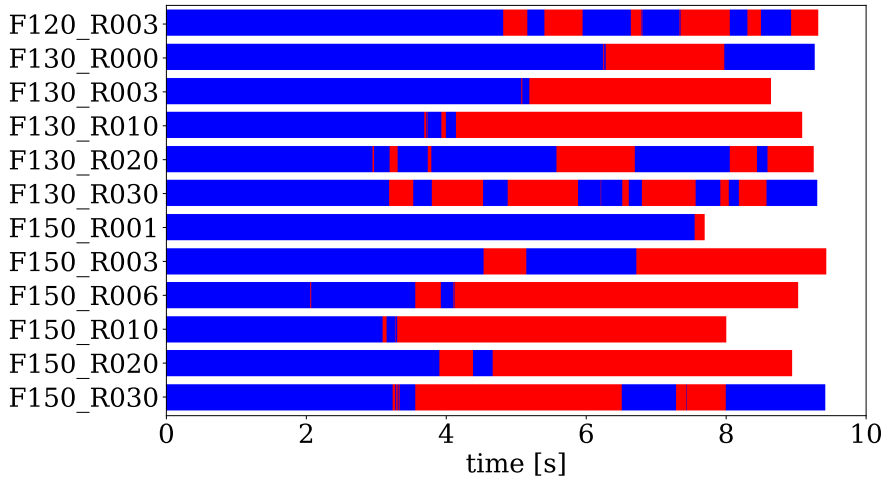

Figure 5.10.: Timelines of all models where a wind phase ($\dot{M}_{\rm acc} = 0$) occurs at least once during the simulated time. Red areas mark the presence of a NDW with at least 10 ms duration.

In agreement with our findings, we see a higher occurrence rate of NDWs in rotating models. In Fig. 5.10, we show a timeline of each model that experiences a wind at some

point during the simulated time. Red areas mark the presence of a wind phase, defined by $\dot{M}_{\mathrm{acc}} = 0$, if it lasts for at least 10 ms, continuously. The earliest wind phases start developing at about 3 s after bounce (a very brief period happens in model F150_R006 at around 2 s), when the accretion of progenitor material has sufficiently subsided.

We see that some wind phases last for several seconds, while others are terminated after a brief time. The termination of a NDW is usually initiated by larger accumulations of matter beyond the wind termination shock, where they are not affected by neutrinos. These accumulations can have negative radial velocities and are accelerated by the gravitational pull of the PNS, through which they gain kinetic energy. On their path towards the PNS, they put a dent in the wind shock front and cause it collapse. The neutrino luminosities throughout a wind phase are almost constant as they consist only of neutrinos originating from the PNS. However, the collapse of a wind results in a luminosity spike because of the sudden contribution from accretion luminosity. Other models, for example F130_R010 and F150_R006, show a long-lived wind that does not collapse.

For long-lasting wind phases, the wind termination shock can stretch out to a considerable radius. We show this at the example of model F150_R020 in Fig. 5.11. This snapshot is taken at the end of the simulation at $t = 8.93$ s after bounce, where the wind phase has been continuously active for 4.29 s. The PNS in this simulation has experienced a kick and at the time of the picture, resides at $z = 5186$ km. The wind termination shock has reached a radius of up to $20\,000$ km, depending on the direction, which allows for the density in the wind to become as low as $42\ \mathrm{g/cm^3}$, with temperatures dropping to 0.24 GK (and again increasing to up to 0.75 GK within the shock). The entropy within the wind is fairly constant and reaches up to $50\ \mathrm{k_B/nuc}$, and exceeds $100\ \mathrm{k_B/nuc}$ in the wind termination shock in the polar directions. We see high velocities of almost 20 % the speed of light in the wind, which corresponds to mach numbers of up to 7. A significant amount of matter also stays supersonic beyond the wind termination shock. The mean expansion timescale, which we calculate as the radius divided by the velocity at a temperature of $T = 5.8$ GK, is 20 ms.

We further investigate our previous claim that rotation can enhance the possibility for the formation of NDWs. As a measurable quantity for the wind probability, we calculate the total time spent within a wind phase for each model, which corresponds to summing all red areas in Fig. 5.10. We only use the simulation times up to $t = 7.5$ s in order to avoid the bias introduced by having different final simulation times for different models. Similar to Fig. 5.9, we use this data to calculate mean values for each variation of Ω_0. Additionally, we perform the same calculation for all different values of f_{heat}, which gives

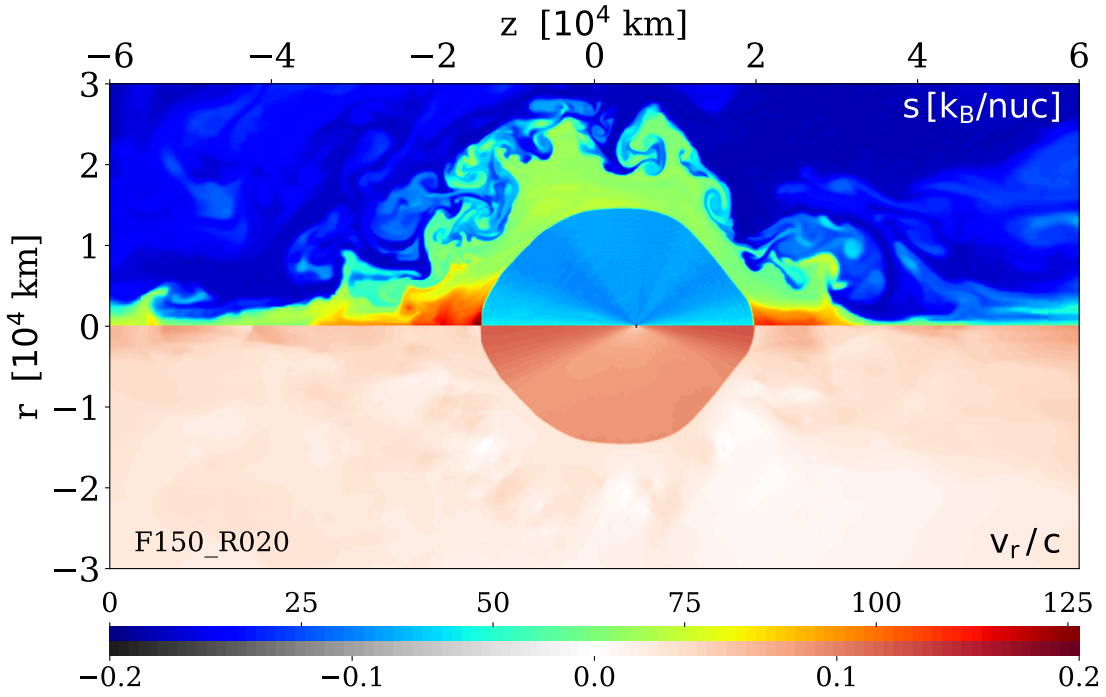

Figure 5.11.: Snapshot of model F150_R020 at the end of the simulation ($t = 8.93$ s). As in Fig. 4.15, the upper half of the domain shows the entropy and the lower one the radial velocity in units of the speed of light. The upper and lower colorbars correspond to entropy and radial velocity, respectively.

an indicator as to how much an increased neutrino heating during the explosion phase contributes to the probability to form a wind at late times.

We show the results in Fig. 5.12, where we summarize the dependence of the wind time on both rotation and neutrino heating in a shared vertical axis plot. There are no winds appearing in models with $f_{\mathrm{heat}} < 1.20$. By further increasing the heating, the first NDWs appear in model F120_R003 at $t = 4.41$ s. However, the individual wind phases in this model are unstable and only last for a few 100 ms each. For heating factors of 1.30 and 1.50, the average duration of a wind is almost the same at $t_{\mathrm{wind}} = 2.3$ s, which corresponds to 31 % of the total simulated time from bounce to $t = 7.5$ s. Because of the (almost) non-existent wind phases in F150_R000 and F150_R001, the error bar is larger for the F150 series. If only the rapidly rotating models with $f_{\mathrm{heat}} = 1.50$ would be taken into

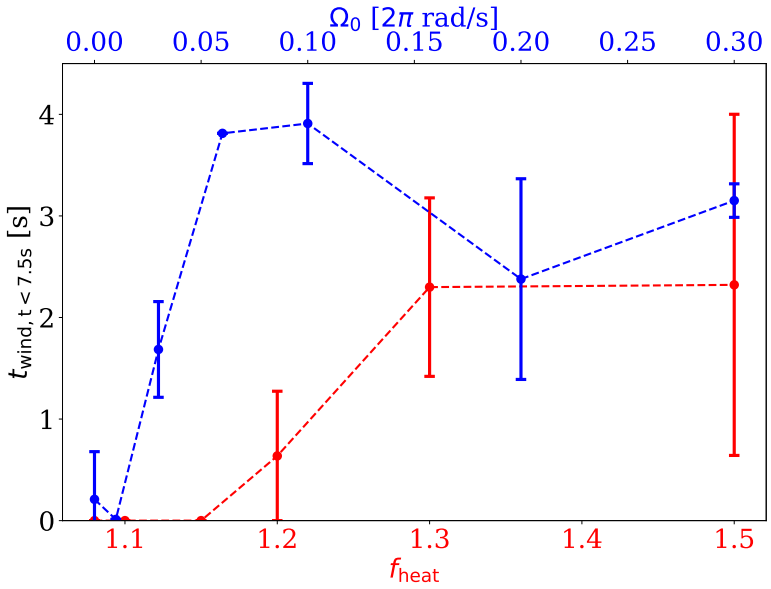

Figure 5.12.: Time spent in a wind phase as a function of f_{heat} (red) and Ω_0 (blue). As in Fig. 5.9, we consider all exploding models with $t_{\mathrm{end}} > 7.5$ s and take mean values with error bars corresponding to the spread due to different models with the same heating factor or rotation strength.

account, the average wind time would be 3.66 s, with a much smaller uncertainty of only 0.45 s.

The correlation of the wind time with Ω_0 is not as monotonic as the one with f_{heat}, but it still shows a trend. For the non-rotating cases, we only have one model (F130_R000) that features a NDW. The same situation appears for the slowest rotating case, where only F150_R001 shows a (very brief) wind phase towards the end of the simulation. When enhancing the rotation further, the wind time eventually increases to values which deviate significantly from zero, and throughout all rapidly rotating models this trend stays robust. This indicates that increased rotation leads to a higher average duration of the wind, with some values of Ω_0 leading to more than half of the 7.5 s simulation time spent in a NDW.

The similarity of the dependence of the late-time accretion (Fig. 5.9) and the wind time (Fig. 5.12) on the rotation suggests a connection between the amount of accreted matter and the average wind duration. We therefore compare these two quantities for all the simulations taken into account in the previous figures, by showing them in a

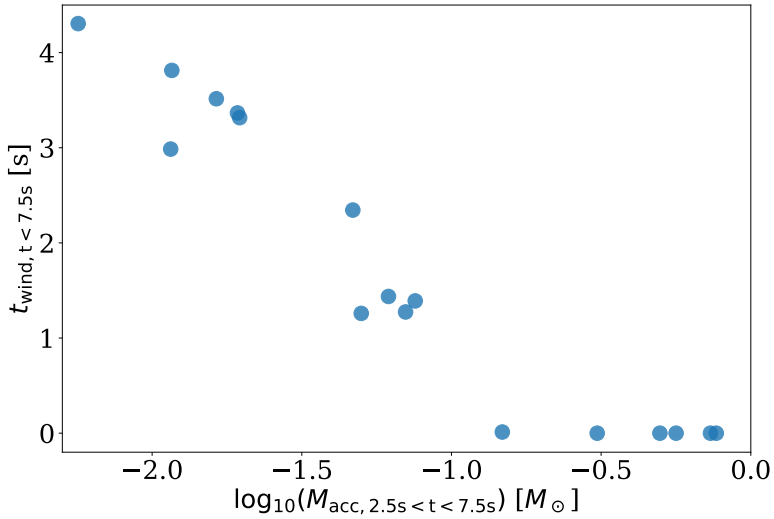

Figure 5.13.: Total time spent in a NDW (up to $t = 7.5$ s) vs. the accreted mass in the time interval $2.5\ \mathrm{s} < t < 7.5\ \mathrm{s}$.

$M_{\mathrm{acc,2.5s<t<7.5s}}$ − $t_{\mathrm{wind,t<7.5s}}$ plane in Fig. 5.13. The wind time has a nearly linear dependence on the logarithm of the late-time accretion for all models that do feature a NDW during the simulation time. We can identify a threshold of $0.1\ M_\odot$ of accreted mass during this 5 s interval, above (below) which we never (always) see a NDW in a simulation. In simulations with $M_{\mathrm{acc,2.5s<t<7.5s}} < 0.03\ M_\odot$ (equivalent to a logarithmic value of -1.5), we find wind times of at least 3 s duration (40 % of the post-bounce time) consistently.

We note that since our study does not include magnetic fields and their effects on matter ejection and the spin-up of the PNS, these results can only provide a general trend. Strong magnetic fields can lead to a jet-like explosion [29, 129, 153, 154, 159, 160], which can change the amount and nature of both ejection and accretion. Furthermore, the results can be different in three dimensions, since the possible shock morphologies in 2D (and the available accretion/ejection directions) are limited by the assumed symmetry and can be different in 3D simulations [41, 129, 130]. However, our results provide a general trend and highlight that rotation plays an important role in the long-time evolution and influences not only the ejected matter and the PNS, but can also enhance the probability for developing a NDW, which in turn leads to an altered neutrino emission and explosion energy.

6. Tracer particle method

The core-collapse supernova (CCSN) simulations presented in the previous chapters 4 & 5 are performed on a mesh grid, where fluid quantities like the local matter density are evolved in each grid cell. This Eulerian description does not track the paths of individual fluid elements. However, in the context of CCSN, one is interested in the ejected matter and its properties, as this is an important observable that can connect simulations with observations. For example, a number of studies connect the ejecta nucleosynthesis and morphology of observed supernovae such as SN 1987A and Cassiopeia A with recent simulations [32, 38, 161, 162]. The transition from the Eulerian fluid description to a Lagrangian one, where individual fluid elements are tracked, is done by calculating the trajectories of representative tracer particles. These tracer particles are advected with the local matter velocity and log the temporal evolution of properties (e.g., density, temperature, electron fraction, ...) of individual fluid elements.

In this chapter, we present our tracer particle method (TPM) for post-processing the trajectories of fluid elements within our simulations. We give a detailed description of our tracer scheme and the subtleties of the calculation, with emphasis on the initial placement of tracers, the advection method and the resolution both in space and time. Furthermore, we analyze the accuracy of our TPM by comparing the ejected tracer mass in a simulation to the ejected mass of the hydrodynamic grid. We focus on the necessary number of tracer particles for a sufficient resolution and relate this to the numerical performance of the calculation. Finally, we calculate tracers for all our (successfully exploding) simulations from chapters 4 & 5 and provide useful properties of the ejected matter that are relevant for the nucleosynthesis.

The TPM code is written in Python 3. All interpolations are performed using the “RegularGridInterpolator” function of the “SciPy”-package [163]. Furthermore, the individual tracer calculations per time step are performed in parallel, using the “multiprocessing”-package of the Python standard library.

6.1. Scheme description

The principal method of evolving tracer particles based on a hydrodynamic simulation can be done in two fundamental ways. In the so-called in-situ method, tracers are evolved in the simulation code itself and advected with the same fluxes that are used for the hydrodynamic calculations. In contrast, the post-processed method uses the output of an already finished simulation and advects tracers based on the velocity fields that are stored in the respective output files. While FLASH features a tracer particle unit that allows for the in-situ calculation of tracers [164], we rely on the post-processed method for a number of reasons. The most obvious downside of having tracers in the simulation is that the initial tracer setup has to be fixed at the beginning of the simulation, and cannot be changed afterwards. This implies that if one was to use another tracer configuration, for example with a larger number of particles for better resolution, the whole simulation must be performed again. Furthermore, it is not possible to explore only specific parts of either the ejecta or the progenitor in the in-situ method, nor it is possible to only calculate tracers in a specific time interval. Finally, the computational method for in-situ tracers leaves not much room for adjustments and is not debug-friendly, as the particle unit is closely tied to the hydrodynamic equations and other units of the simulation code. On the other hand, in-situ tracers have a better time resolution as they are advected in each simulation step, while the output files that are used for the post-processed method are written only every 1 ms simulation time (in the setup used in chapters 4 & 5), which corresponds to a few hundred steps between each file.

The post-processed method uses the output files of the simulation (checkpoints) as an input. The simulation data in the checkpoints follows the grid structure of FLASH at the time the file is written. Because of the adaptive mesh refinement (AMR), data points can correspond to grid blocks of different sizes which can also change from file to file (see Fig. 3.2). We therefore interpolate the checkpoint data and map it onto a regular grid as a first step. All further calculations are done by using this regular grid structure, which is equal for all time steps. In order to have sufficient spatial resolution in the center, we divide our regular grid in two regions. The inner region extends up to $r = 5000$ km around the current PNS location, while the outer region covers the remaining simulation domain, $5000 \text{ km} < r < 160.000 \text{ km}$. During the advection calculations, the grid quantities used for each tracer are taken from either the inner or the outer regular grid, depending on the current position of the tracer.

6.1.1. Initial tracer placement

At the beginning of a TPM calculation, a given number of tracers needs to be initialized at starting positions. In our tracer scheme, the initial time step can be at any one of the simulation checkpoints, and the tracer positions are set with respect to the grid data at that time step. There are several different possibilities to initialize the tracer positions. In the study of Harris et al. (2017) [165] with CCSN models in four different progenitors, the initial positions are set at the beginning of the simulation, with tracers positioned in rows and columns, equidistant in the progenitor mass distribution. In that way, all particles represent fluid elements of the same mass. This method was already used in a similar fashion by Travaglio et al. (2004) [166] for 2D and 3D simulations of type Ia supernovae. However, it is only applicable at the beginning of the simulation, because it requires spherical symmetry at the time of tracer initialization. In contrast, Nishimura et al. (2015) [167] use a uniform distribution with fixed spatial distances between individual tracers. While this is a rather straight-forward method for the positions, it results in different masses for each tracer.

For our TPM, we use a distribution method that results in the same mass for each tracer as in Ref. [165, 166], but is also applicable post-bounce when the spherical symmetry is broken. We can assign the same mass to every tracer when the particle density is proportional to the mass density. This proportional-to-mass method is independent of the current state of the simulation, as it can be applied to any mass distribution. A similar distribution method is also available in the in-situ particle unit of FLASH [164].

We start our tracer distribution algorithm by defining a total number $N_{\mathrm{pt},0}$ of particles that we intend to place. The mass distribution on the grid is inferred from the density distribution, which is stored within the initial checkpoint, and the geometry of the grid. We assign the particle positions by employing a recursive function that divides the computational domain into four quadrants of equal size. For each of these quadrants, the enclosed mass m_{i} ($i \in \{1, 2, 3, 4\}$) is calculated via interpolation of the regular grid points. The amount of tracers for each quadrant is then proportional to the respective mass fraction,

$$N_{\mathrm{pt,i}} = N_{\mathrm{pt},0} \cdot \frac{m_{\mathrm{i}}}{\sum_{i=1}^{4} m_{\mathrm{i}}}\,, \tag{6.1}$$

where we round the resulting value to the nearest integer. For each of the quadrants we then proceed with the same calculation by dividing it into another four quadrants, and substituting $N_{\mathrm{pt},0}$ with $N_{\mathrm{pt,i}}$. In that way, we refine the total domain size to smaller areas and particle numbers. We stop the recursion when $N_{\mathrm{pt,j}} \leq 2$ is encountered for some

quadrant j. The remaining one or two particles are then placed at random positions within the current quadrant. For $N_{\mathrm{pt,j}} = 0$, no particle is placed.

We show an example of our recursive distribution algorithm in Fig. 6.1. We use the first checkpoint of one of the simulations from the previous chapters and choose $N_{\mathrm{pt},0} = 2000$. Because of the rounding performed in each recursion step, we obtain a total number of $N_{\mathrm{pt}}^{(\mathrm{tot})} = 2128$ particles from the algorithm, corresponding to an assigned mass of $1.76 \cdot 10^{-3}\ M_\odot$ per tracer. We show the individual tracers as black dots, with underlying rectangles of different color for the respective recursion level necessary to obtain $N_{\mathrm{pt,j}} \leq 2$ in the specific region. Consequently, each rectangle contains only one or two dots. White spaces are present where no tracer was set, i.e., where $N_{\mathrm{pt,j}} < 0.5$ was obtained after applying equation (6.1) to the quadrant of the previous recursion level. Because of the two-dimensional geometry in our simulations, the spatial volume near the cylindrical axis approaches zero, which translates to a smaller mass there. The most dense mass distribution therefore appears not in the coordinate origin, but at $r \approx 260$ km.

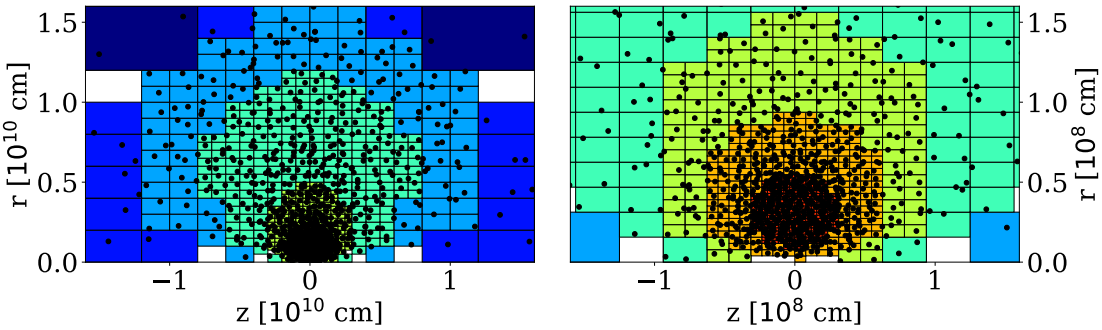

Figure 6.1.: Initial distribution of 2128 tracers at the beginning of the simulations described in chapter 4 & 5. The black dots mark the individual tracers. The colored squares indicate the highest refinement for a tracer to be set in that region, with recursion levels from 2 (dark blue) to 9 (red). The left panel shows the whole computational domain (160.000 km), the right panel a subset of the innermost 1600 km.

We verify that our tracer distribution accurately represents the mass distribution in the progenitor, by computing the enclosed mass as a function of the radius. Because all our tracers have the same mass, we simply need to count them into radial bins and multiply with the mass of one particle. In Fig. 6.2, we show the result as a comparison to the progenitor. We can see that even with only 2128 tracers, we can rather accurately map

the mass distribution, with a total deviation of ≈ 1 % for the whole domain. For the production runs in Sec. 6.3, we will further increase $N_{\mathrm{pt},0}$ by a factor 10, which results in an even better accuracy and mass resolution of our TPM.

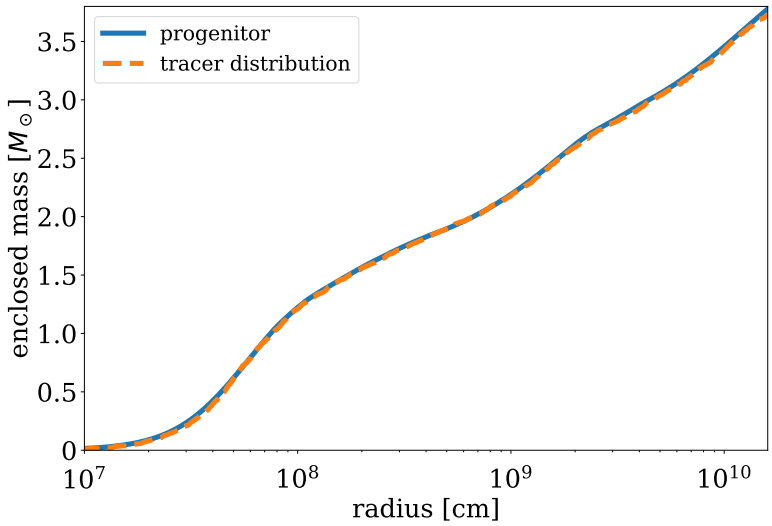

Figure 6.2.: Enclosed mass over radius for the progenitor (solid, blue) and the tracer distribution shown in Fig. 6.1 (dashed, orange).

We furthermore implement the possibility to restrict the available area for tracer placement. This area can be defined by any conditions based on the grid quantities in the simulation and is especially useful when placing tracers in the post-bounce phase. By default, we exclude all regions that correspond to the interior of the PNS, i.e., where $\rho > 10^{11}$ g/cm^3. For example, it is possible to place tracers only in nucleosynthesis-relevant areas, by combining the density condition with another one based on the local temperature. Another application can be the distribution of tracers within persistent downflows, so that one can follow the paths of accreted matter at late times. Our TPM advection method also works backwards in time, so that another possibility includes placing tracers at the end of the simulation in regions of ejected matter ($e_{\mathrm{tot}} > 0$), and following the history of these fluid elements back to their origin.

6.1.2. Advection method

Tracer particles are passively advected with the local fluid velocity. In each advection step, the grid quantities from the checkpoint are interpolated to the tracer position. The quantities that are of interest for the final trajectories are then stored in a string variable that is written every 50 steps to a trajectory output file. Our TPM outputs the following quantities to the trajectory file by default:

- t - current simulation time (including pre-bounce time),
- r - distance from PNS,
- ρ - density,
- T - temperature,
- Y_e - electron fraction,
- s - entropy,
- $\vec{v}$ - velocity in x and y-direction,
- $\vec{x}$ - position in x and y-coordinates, relative to the PNS,
- "ejected" - boolean flag $(0/1)$ if tracer is energetically unbound ($e_\mathrm{tot} > 0$).

Similarly, we calculate the relevant quantities of the neutrino flux at the tracer position and likewise output them every 50 steps into a "luminosity"-file. For this, we define rays with 2° spacing outgoing from the PNS. We integrate the local emissivities and absorptivities stored in the checkpoints along these rays to obtain the neutrino luminosities. For tracers that are close to the PNS, we consider the local luminosity at the respective radius r and angle θ. For particle positions $r \geq 400$ km, this is approximated with the value at infinity along the angle θ. The neutrinosphere radii are defined analogously to the previous chapters, where $\tau_\nu = 2/3$, and the neutrino energies are given from the local values at the neutrinosphere. In the luminosity output files we then write the following quantities:

- t - current simulation time (including pre-bounce time),
- r_ν - neutrinosphere radii,
- L_ν - neutrino luminosities,
- E_ν - neutrino energies.

We distinguish between electron neutrinos and antineutrinos and give separate values of them for each quantity. For compatibility reasons with the nuclear reaction network WinNET [119], we also add luminosity and energy columns for muon neutrinos and antineutrinos, but leave them filled with zeros.

The tracers are advanced using a simple Euler scheme, similarly to Ref. [165]. We use the local velocities in x and y-direction to advance the particle from step n to $n+1$:

$$\begin{aligned} x^{(\mathrm{n}+1)} &= x^{(\mathrm{n})} + v_{\mathrm{x}}^{(\mathrm{n})} \cdot \Delta t \,, \\ y^{(\mathrm{n}+1)} &= y^{(\mathrm{n})} + v_{\mathrm{y}}^{(\mathrm{n})} \cdot \Delta t \,, \end{aligned} \tag{6.2}$$

with $\Delta t = t^{(\mathrm{n}+1)} - t^{(\mathrm{n})}$. Equations (6.2) also allow for a backwards calculation, the time difference between two steps will then be $\Delta t < 0$. The checkpoints from our simulations are written every 1 ms. With typical velocities encountered in the simulations of up to 30 % the speed of light, a tracer can advance up to 90 km in a single step. In the case of strong downflows near the PNS, this can lead to an advection step where the tracer skips into or through the PNS in an unphysical way. We therefore use a sub-stepping method that advances the particle for several smaller steps within a single time step. In the vicinity of the PNS, we use ten sub-steps for each 1 ms, which eliminates the risk of tracers passing through the PNS. For particles at a larger radius ($r > 5000$ km), we perform five sub-steps instead. This interpolation in time is performed with the same checkpoint, i.e., assuming a slowly changing configuration relative to the 1 ms time steps.

We illustrate the necessity of the sub-stepping method with an example trajectory in Fig. 6.3. Here, we choose one of the simulations discussed in the previous chapters at a time where a strong downflow from one polar direction occurs. We set a starting point for an example tracer within the downflow and advance it using equations (6.2). The blue line shows the trajectory for a time step of 1 ms. As the radial velocity at the starting position is $v_{\mathrm{r}} \approx -76$ km/ms, the tracer directly ends up within the PNS after only one step. However, if we choose time steps of 0.1 ms instead (corresponding to ten sub-steps), the tracer gradually moves around the PNS and is eventually ejected in the equatorial direction (green line).

The PNS as a comparably small but massive object requires a careful treatment in the TPM calculation. In our simulations, its mass can become roughly half of the total mass within the computational domain, which is equivalent to half of the tracers being concentrated within a fraction of $\approx 2 \cdot 10^{-8}$ (assuming $R_{\mathrm{PNS}} \approx 25$ km) of the total area. In most cases, the PNS mass saturates and does not contribute to ejected matter. It is therefore not necessary to further advance particles, once they are accreted onto the PNS. Furthermore,

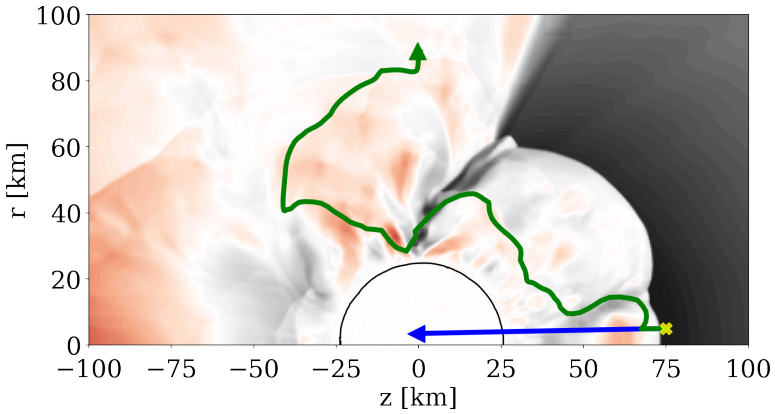

Figure 6.3.: Example trajectories of a tracer starting within a downflow at the yellow cross, advanced with (green) and without sub-stepping (blue). The snapshot is taken from the F120_R000 simulation at 1.81 s post-bounce and shows the radial velocity, with positive values in red (outflows) and negative values in black (downflows). The black line marks the PNS contour. For this example, the green trajectory is calculated for more than 1 ms.

test runs have shown that occasionally high velocities can appear within the PNS, leading to an unphysical amount of tracers leaking out of the PNS again. We therefore define a critical density of $\rho_{\mathrm{crit}} = 10^{14}\ \mathrm{g/cm^3}$, above which we consider a tracer to be part of the PNS. Once the density in a trajectory exceeds ρ_{crit}, the TPM does not advance the tracer any further. We choose a higher value for the critical density than the commonly assumed $10^{11}\ \mathrm{g/cm^3}$ for the PNS boundary, because individual fluid elements can still be ejected if they are close to the neutrinosphere, which usually lies within the PNS boundary. Test runs have shown that the exact value for ρ_{crit}, if it lies in the range of $10^{11} - 10^{14}\ \mathrm{g/cm^3}$, results in only minor differences ($\lesssim 2$ %) for the amount of ejected tracers.

The implementation of ρ_{crit} is advantageous for the numerical performance of the TPM, both in the tracer calculation and the I/O part. Furthermore, we can infer the PNS mass by counting all tracers where the trajectories end before the final simulation time. We will use this, together with the ejected mass by tracers, to test the accuracy of the TPM in the next section. We note that this method excludes the tracer representation of ejected matter by neutrino-driven winds (NDW) in our calculation, because the PNS mass as inferred from the amount of tracers can only increase and saturate, but not decrease. However, since only small amounts of matter are ejected in a NDW (corresponding to

very few tracers in total), a much larger amount of total particles would be necessary to accurately capture wind ejecta. We therefore propose the method of placing tracers only close to the PNS at a starting time during a wind phase, if one was to study the wind ejecta with the TPM presented here.

6.2. Accuracy and performance

We test the accuracy of our TPM scheme by comparing the ejected mass within the simulation with the ejected mass as represented by tracers. The condition for ejected matter is the same in both cases, i.e., a positive total energy of the simulation cells or tracers. Because all our tracer particles have the same mass, we can infer the mass of ejected matter at a given time by counting all tracers with $e_{\rm tot} > 0$ and multiplying this with the individual tracer mass. As a reference, we use the F130_R000 model which has a total ejected mass of $1.42\ M_\odot$ at the end of the simulation. We vary the number of placed tracers $N_{\rm pt,0}$ from 200 to 20.000 (note that the actual number of placed tracers can deviate from that as explained in Sec. 6.1.1) and perform a TPM calculation for each value. The resulting mass resolutions (mass per particle) then lie in the range between $1.88 \cdot 10^{-2}\ M_\odot$ and $1.76 \cdot 10^{-4}\ M_\odot$.

The total ejected mass over time for model F130_R000 and the various tracer configurations is shown in the top panel of Fig. 6.4. We see that the TPM is able to reproduce the general trend even for the smallest amount of set tracers. For this N200 case ($N_{\rm pt}^{\rm (tot)} = 199$ actually placed tracers), 76 tracers are considered ejected at the final simulation time. This comparably small amount explains the coarse increase of the ejected mass. Because all configurations are in good agreement with the simulation output, we show the deviation $\Delta M_{\rm ej}$ over time in the bottom panel of Fig. 6.4, to make the differences better visible. From this plot we can see that the smallest number of tracers deviates the most from the simulation output, first by overestimating (first three seconds), and later by underestimating the ejected mass. The approximation improves with increasing values for $N_{\rm pt,0}$. The total ejected mass by the end of the simulation is represented with $< 1\ \%$ error for all cases with $N_{\rm pt,0} \geq 2000$.

We furthermore compare the PNS mass as represented by tracers with a final trajectory time $t < t_{\rm end}$, with the simulation output for $M_{\rm PNS}$. The latter is given by the sum over all cells with $\rho \geq \rho_{\rm PNS} = 10^{11}\ {\rm g/cm^3}$. We show the result in Fig. 6.5. In general, the TPM underestimates the PNS mass for all configurations. We attribute this to a consequence of the stricter criterion for tracers to be counted as part of the PNS, than for simulation

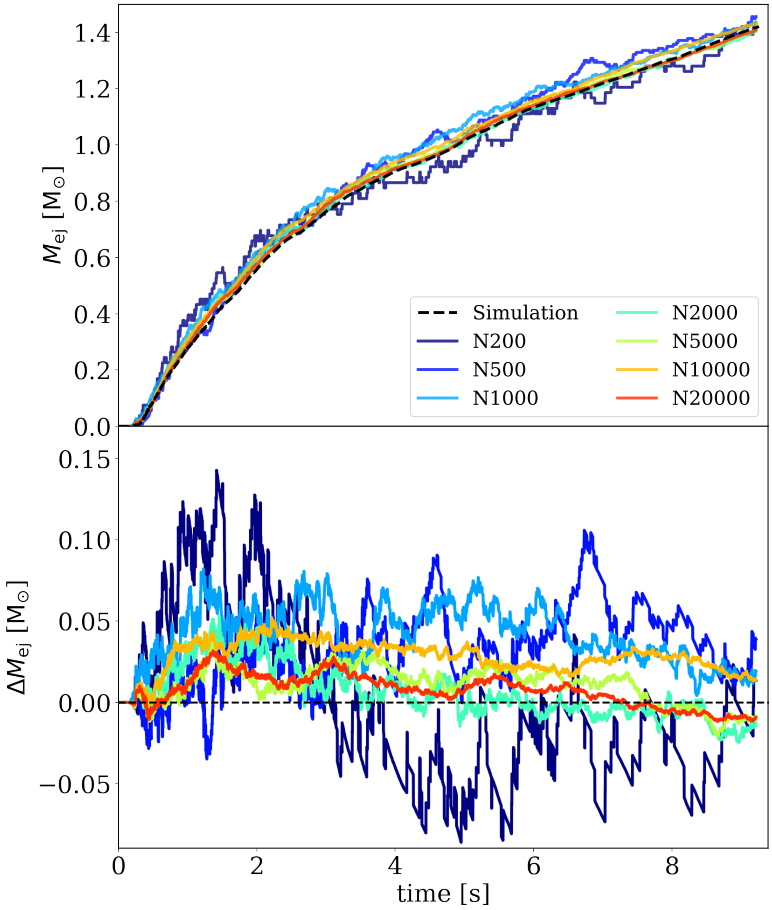

Figure 6.4.: Top panel: Ejected mass in the simulation F130_R000 (dashed black line) and ejected mass by tracers with different values for $N_{\mathrm{pt},0}$. Bottom panel: Deviation in the ejected mass over time.

cells, i.e., $\rho_{\mathrm{crit}} > \rho_{\mathrm{PNS}}$. The convergence for higher values of $N_{\mathrm{pt},0}$ is not as prominent as for the ejected mass. However, we see that configurations with $N_{\mathrm{pt},0} \geq 2000$ capture the PNS mass better, with exception of the N10000 case. Finally, from Fig. 6.5 it becomes clear that the TPM does not capture possible mass loss of the PNS. As already discussed above, the PNS mass as inferred from tracers can only increase monotonically.

The main purpose of the TPM is to provide trajectories of ejected matter for nucleosyn-

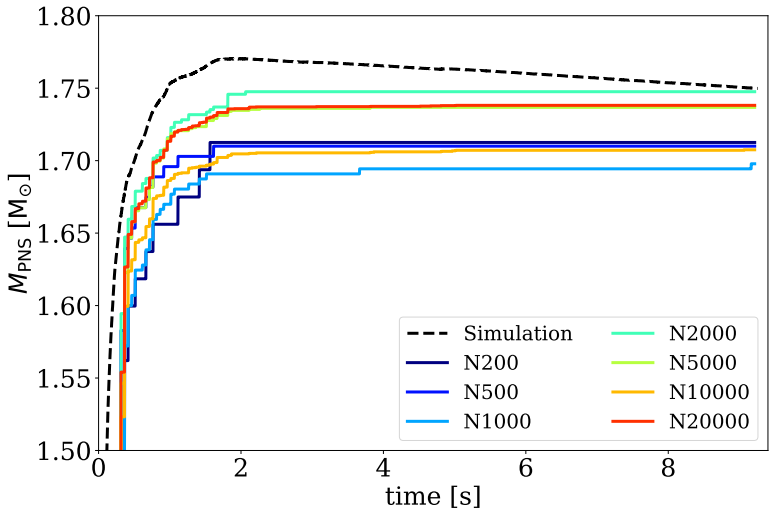

Figure 6.5.: Proto-neutron star mass in the simulation F130_R000 (dashed black line) and its equivalent as inferred from the TPM with different values for $N_{\mathrm{pt},0}$.

thesis calculations. From the accuracy discussion based on Fig. 6.4, we therefore rely on the N20000 configuration for subsequent calculations. This configuration has the lowest mean error over the whole simulation time and never deviates more than $0.03\ M_\odot$ from the ejected mass in the simulation in the test case model F130_R000. With a total number of $N_{\mathrm{pt}}^{(\mathrm{tot})} = 21.281$ placed tracers for our progenitor model, its mass resolution is $1.76 \cdot 10^{-4}\ M_\odot$, which is comparable to the "medium resolution" case in Ref. [167].

We conclude this section by quantifying the numerical performance of the TPM scheme. In general, the wall-clock time of a TPM run depends on two parameters, the number of placed tracers and the number of calculated checkpoints. Some applications (e.g., full CCSN simulation, focus on specific region, focus on NDW ejecta, ...) can require different amounts of tracers or simulation steps. We evaluate the performance and give an approximate formula for the wall-clock time based on these two parameters. Note that the actual numbers are machine-dependent.

At the beginning of each simulation step, the corresponding FLASH output file is read in and interpolated. We also evaluate the neutrino quantities at this point and store them in a radius and angle-dependent array. For a given tracer, the respective quantities will then be read from this array, depending on its radius and angle. The tracers are advanced independently, which makes it possible to parallelize this calculation step. The required

memory depends on the amount of tracers and steps between each output phase, as well as the number of parallel processes. In our default setup with $N_{\mathrm{pt}}^{(\mathrm{tot})} = 21.281$ and the output phase in every 50 steps, we use 12 parallel processes. The total required memory then amounts to roughly 50 GB, or 4.2 GB per process. Parallel processes are realized with the "multiprocessing"-package of the Python standard library. For our default setup, the output files consist of a trajectory file and a luminosity file for each tracer, as well as two log files, of which one tracks the required time for each calculation step. The file sizes vary, as the trajectories for particles trapped in the PNS are shorter. The total required disk space for a TPM calculation for one of the previously shown simulations is ≈ 25 GB.

We track the required wall-clock time in each simulation step and distinguish two major calculation parts. The first one includes the checkpoint file read-in, interpolation, and neutrino quantity calculation. The second part involves the advancing of the individual tracers and, every 50 steps, the output phase. We label the two parts as "read" and "calc", respectively. The wall-clock time for both parts per step is shown in Fig. 6.6, for the example of the TPM calculation of model F130_R000. As the simulation checkpoints are spaced 1 ms apart, the "steps" are identical with the simulation time in ms, plus the pre-bounce time of 286 ms. The performance of the "read" part strongly depends on the calculation of the neutrino quantities. In the pre-bounce phase, all quantities are set to zero, as we use the deleptonization scheme of Ref. [125] there. After bounce, the required wall-clock time depends on the extent of the PNS and the gain radius, since we integrate the luminosities from the center outwards and evaluate R_ν and E_ν at the neutrinosphere. The "calc" part wall-clock time decreases after bounce, when a large fraction of tracers becomes part of the PNS and is not advanced further. The vertical spikes correspond to the output phase every 50 steps. We see that the I/O phases cause large differences between individual steps, both in the checkpoint read-in and in the writing process during the output phase, as can be seen from the height of the individual spikes there. However, this is a machine-dependent parameter.

The average wall-clock times of the two calculation parts allow for an estimate of the total required time for a TPM run as a function of the calculation steps and number of tracers. The total time for the "read" part depends only on the calculation steps, while the "calc" part is assumed to depend equally on the calculation steps and amount of tracers. We therefore estimate the total required wall-clock time for a TPM run with number of steps N_{steps} and number of tracers N_{tracer} as

$$t_{\mathrm{tot}} = \tau_{\mathrm{read}} \cdot N_{\mathrm{steps}} + \tau_{\mathrm{calc}} \cdot \frac{N_{\mathrm{steps}}\, N_{\mathrm{tracer}}}{N_{\mathrm{pt}}^{(\mathrm{tot})}}\,, \tag{6.3}$$

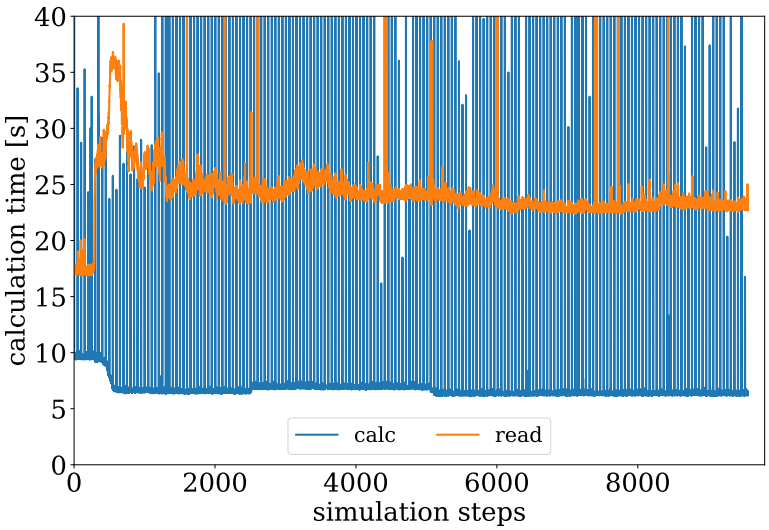

Figure 6.6.: Wall-clock time for the “read” (orange) and “calc” (blue) parts in a TPM run of the F130_R000 simulation per calculation step.

where $\tau_{\mathrm{read}} \approx 25.5\,\mathrm{s}$ and $\tau_{\mathrm{calc}} \approx 8.4\,\mathrm{s}$ are the mean values of each part, taken as an average over all TPM runs performed for the exploding simulation models. The denominator $N_{\mathrm{pt}}^{(\mathrm{tot})} = 21.281$ corresponds to the total number of tracers used in these runs.

We use equation (6.3) to show the wall-clock time estimates in Fig. 6.7. The white contour lines mark 24 hours calculation times. The black line corresponds to 1000 core-hours for our setup with 12 parallel processes. In the case of model F130_R000 (black cross), the total TPM calculation took 89.3 hours and required 1072 core-hours. As we can see from Fig. 6.6, the wall-clock time depends more on the number of simulation steps than the amount of tracers. For twice the amount of tracers, the required time would increase by only ≈ 25 % (however, this would also require more memory and hard-disk space).

6.3. Simulation results

We perform TPM calculations for all 21 exploding simulations from chapters 4 & 5. The general setup is the same for all simulations, distributing the tracers at the first checkpoint with $N_{\mathrm{pt},0} = 20.000$ (21.281 actually placed tracers) within a sphere with a radius equal to

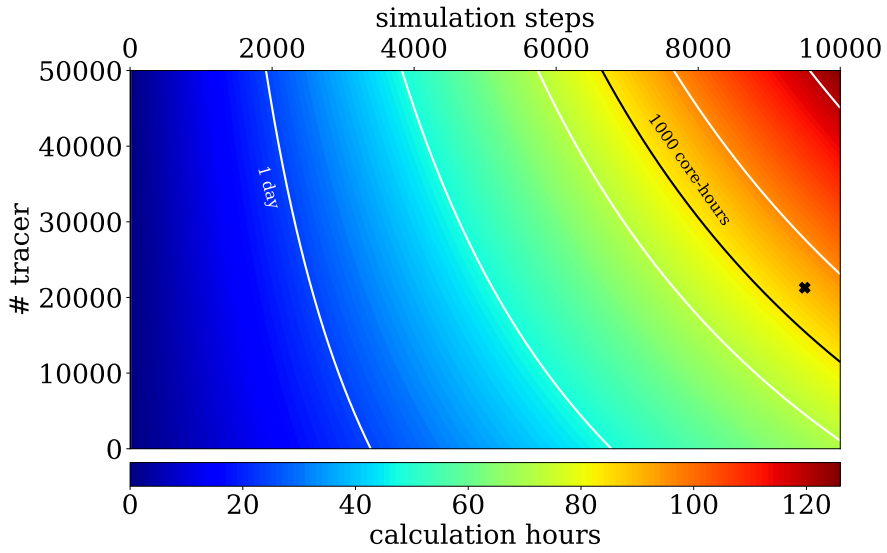

Figure 6.7.: Wall-clock time estimates in hours according to equation (6.3) for a given number of calculation steps (vertical axis) and tracers (horizontal axis). The white lines correspond to contours of 1 day $= 24$ hours, while the black line shows the 1000 core-hours contour (for 12 parallel processes). The black cross marks the example case of model F130_R000, with $t_{\mathrm{tot}} \approx 89.3$ hours.

the domain size of $1.6 \cdot 10^{10}$ cm. Therefore, the mass of each individual particle is always the same, $m = 1.76 \cdot 10^{-4}\, M_{\odot}$. In the following, we show a subset of the performed calculations and selected results that can be achieved using Lagrangian tracer particles.

We only show results based on tracers that are considered ejected at the end of the simulation. These ejected tracer are furthermore grouped into two categories, which we label “neutrino-processed” and “shock-processed”. Neutrino-processed particles are assumed to have experienced a considerably higher neutrino flux than shock-processed ones. They typically show a different nucleosynthesis pattern than particles which are ejected with the shock, as they come closer to the PNS and reach higher peak temperatures. In the CCSN simulations shown in this study, neutrino interactions are the only source for changes in the electron fraction Y_{e} after bounce. We therefore use a Y_{e}-criterion to distinguish the two groups. Tracers are considered neutrino-processed, when their electron fraction changes by $|\Delta Y_{\mathrm{e}}| > 0.01$ compared to their starting value. Particles that retain their original electron fraction fall in the shock-processed category.

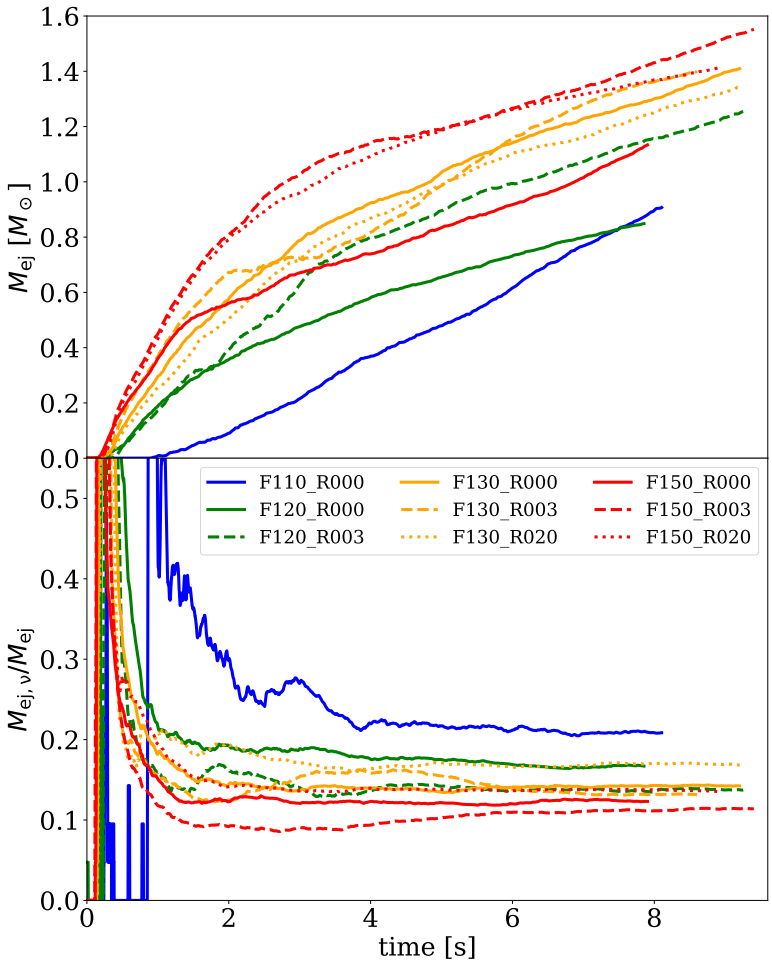

Figure 6.8.: Top panel: Ejected matter for simulations with heating factors 1.10 (blue), 1.20 (green), 1.30 (orange) and 1.50 (red) with no rotation (solid), moderate rotation (dashed) and rapid rotation (dotted). Bottom panel: Fraction of neutrino-processed tracers. The curves are smoothed with running averages of 10 ms.

We show the total ejected matter and its fraction of neutrino-processed ejecta for a subset of simulations in Fig. 6.8. The late and comparably weak explosion in model F110_R000 results in a slow increase of ejected matter. At late times, it still surpasses the F120_R000

model which shows a strongly monopolar shock expansion and therefore pushes matter away only in one half of the domain. With the exception of the F130 cases, rotation seems to enhance matter ejection in our simulations, which can be attributed to the more spherical shock expansion (see Sec. 5.4). The fraction of neutrino-processed tracers follows a similar pattern for all models. Matter ejected at shock revival has an altered electron fraction, because neutrino interactions are necessary to push the stalled shock outwards. As the shock expands, matter at larger radii, which did not come close to the PNS, is also pushed away, contributing to an increasing fraction of shock-processed tracers. The fraction of neutrino-processed tracers saturates after about 2 s after shock revival at values between $10 - 25$ %. We identify an approximate correlation of the amount of neutrino-processed tracers with the heating factor, as lower heating factor models show persistent downflows for longer time, thus having a higher contribution of neutrino-processed tracers at later times.

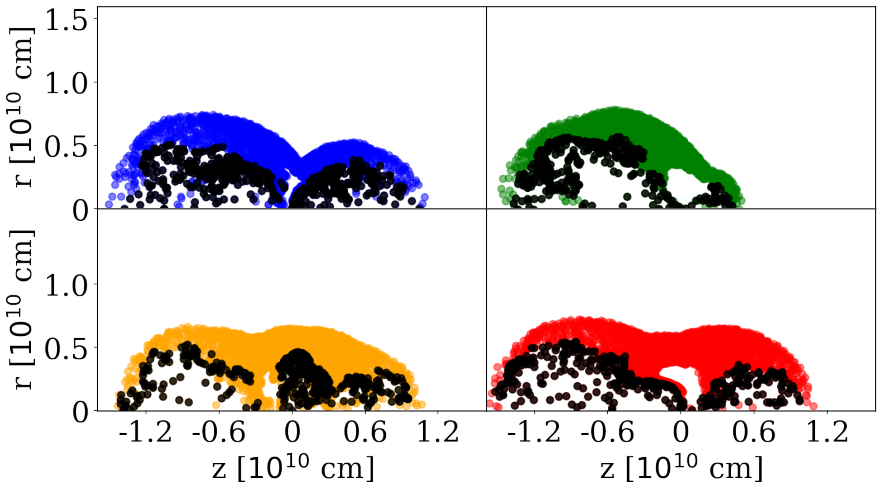

Figure 6.9.: Final tracer positions in the 2D domain. The color code follows Fig. 6.8, black dots represent neutrino-processed tracers. We show only every second tracer for better visibility.

In the following, we focus on the non-rotating models in Fig. 6.8 and investigate differences in the tracer evolution. Figures showing individual tracers or trajectories follow the color code in Fig. 6.8, with blue (F110_R000), green (F120_R000), orange (F130_R000) and red (F150_R000). In multipanel plots, black dots and lines are used for neutrino-processed tracers of the specific model, while shock-processed tracers are shown in the

respective model color. Figure 6.9 depicts the final positions at the end of the simulation for all models. The plot shows every second tracer to avoid a messy picture. White areas correspond to non-ejected matter and downflows, or a region of low density (i.e., few tracers) in an outflow stream. We can identify the shock contour as the outer layer of ejected tracers. In model F120_R000, the strongly monopolar shock expansion to the left side is clearly visible. Here, 76 % of all ejected tracers are in the left half of the domain ($z < 0$) at the end of the simulation, compared to values between $48 - 59$ % for the other models. Neutrino-processed tracers, even though being ejected from the vicinity of the PNS, end up at large radii close to the shock front, which implies that they are accelerated to high velocities. In model F150_R000, the white region just above the PNS ($z \approx 0$ and $0 < r < 0.4 \cdot 10^{10}$ cm) corresponds to a downflow with bound matter, while the white spaces towards positive and negative z-coordinates are low-density regions of ejected matter.

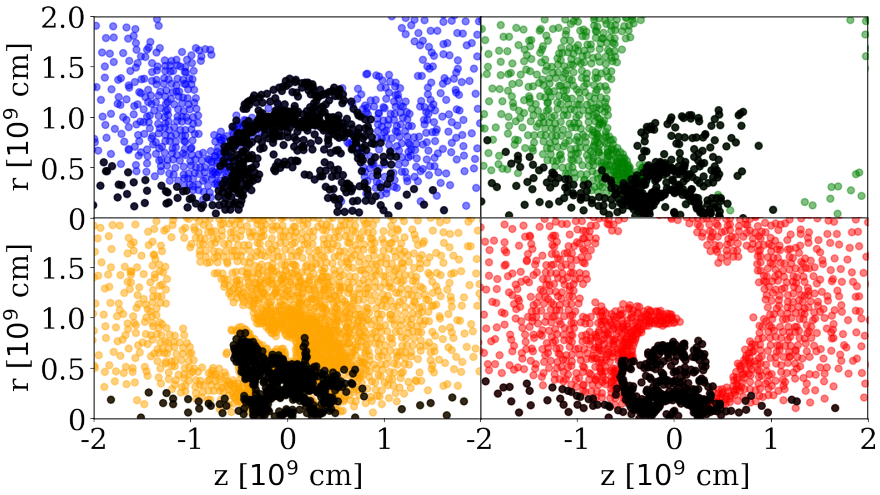

Figure 6.10.: Initial tracer positions in the center of the 2D domain. The color code follows Fig. 6.8, black dots represent neutrino-processed tracers. We show only every second tracer for better visibility.

We can trace the particle trajectories back to their origin in the progenitor. This gives an idea of the relevant starting regions for tracers. The initial positions of ejected tracers are shown in Fig. 6.10. As this is a pre-collapse snapshot, all white areas correspond to regions that will not be ejected. We focus on the innermost $2 \cdot 10^9$ cm in the plot to highlight the impact of different heating factors on the PNS formation. The main difference of the two

lower heating factors models F110_R000 and F120_R000, compared to F130_R000 and F150_R000, is the larger white regions around the center, i.e., a bigger fraction of tracers that will end up in the PNS. This is in agreement with the larger final PNS masses in these models, which are $2.10\ M_\odot$ (F110_R000) and $2.03\ M_\odot$ (F120_R000), compared to $1.75\ M_\odot$ (F130_R000) and $1.87\ M_\odot$ (F150_R000). In model F110_R000, almost no tracers starting within a sphere of $0.5 \cdot 10^9$ cm around the center are ejected. This is due to the long explosion delay ($t_{\rm exp} = 0.93$ s), during which matter near the center is accreted onto the PNS. The majority of tracers that are later in the simulation neutrino-processed and ejected, start within a sphere of 10^9 cm around the center. However, some of them start also at larger radii, from which they are first accreted towards the PNS and then later re-ejected. This highlights the importance of a sufficiently large simulation domain size for nucleosynthesis calculations.

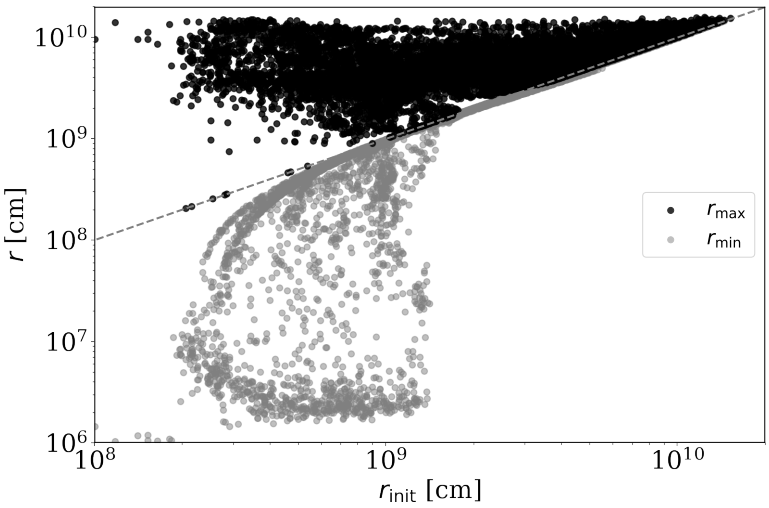

Figure 6.11.: Minimum (gray) and maximum (black) radii of tracers versus their initial radii. This plot contains tracers from all simulations shown in Fig. 6.9 and 6.10. The dashed line corresponds to $r = r_{\rm init}$. We show only every second tracer for better visibility.

The tracer dynamics can be visualized by relating the minimum and maximum radii of each particle. The minimum and maximum radii are shown as a function of the initial radius in Fig. 6.11. We use ejected tracers of all simulations of Fig. 6.9 and 6.10, gray and black dots are used for $r_{\rm min}$ and $r_{\rm max}$, respectively. Particles starting at $r_{\rm init} \lesssim 1.5 \cdot 10^9$ cm can be accreted to small minimum radii close to the PNS. Further out, tracers do not

significantly change their position until the shock moves through their area, because the progenitor infall velocities are lower and the gravitational pull of the center decreases with r^{-2}. The maximum radii do not depend as much on the initial position, because tracers that start close to the center are usually accelerated to high velocities.

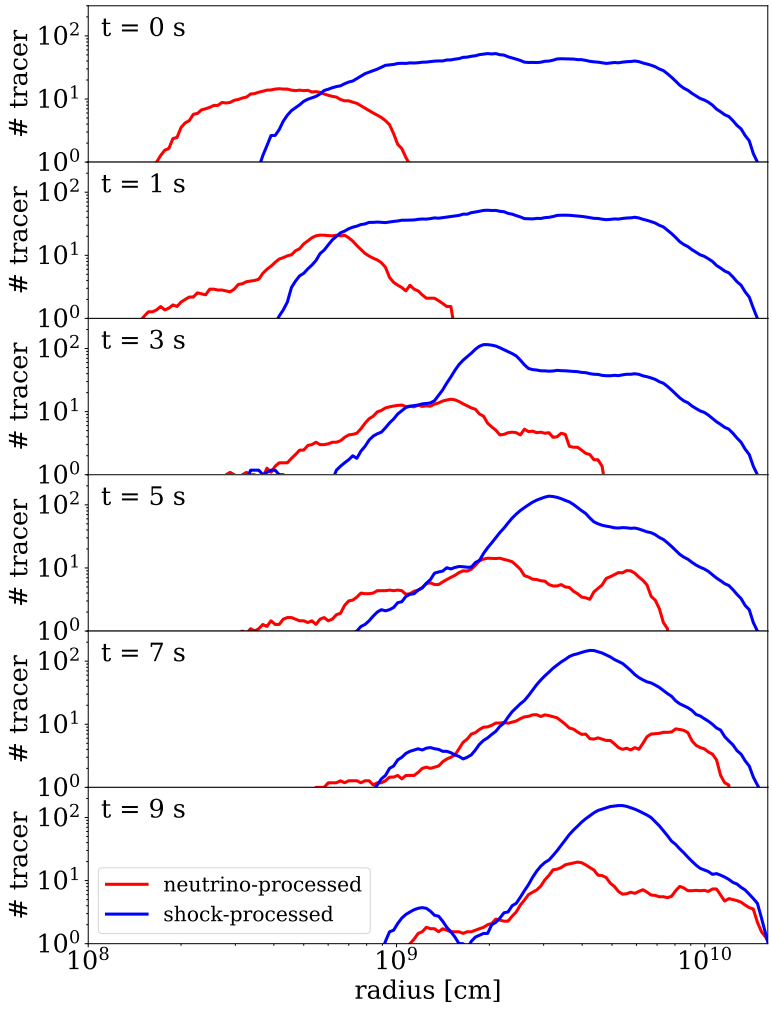

Figure 6.12.: Evolution of the radial distribution of neutrino-processed (red) and shock-processed (blue) tracers for model F130_R000.

The two groups of neutrino-processed and shock-processed tracers mix over time, as seen by their final positions in Fig. 6.9. We can follow this mixing over time when we show the radial distribution of the two groups for different simulation times. Figure 6.12 depicts the evolution of the radial distributions, starting at bounce-time, for model F130_R000. The two groups are near-uniformly distributed before the shock forms, with an overlapping region in-between $3 \cdot 10^8 < r < 10^9$ cm. As the shock moves outwards, it compresses both distributions from smaller radii towards larger ones. The higher velocity of neutrino-processed tracers results in a growing overlap, until at $t = 9$ s both distributions reach out to the domain boundary. The apparent lack of tracers below $9 \cdot 10^8$ cm towards the end of the simulation is a result of a low-density region there, after a neutrino-driven wind phase (see Fig. 5.10), and is consistent with the total mass between the PNS and this radius at the time. At $t = 9$ s, the local maximum around $r = 10^9$ cm corresponds to a wind termination shock that has remained from the earlier NDW.

We further investigate how the starting position of a tracer affects its trajectory and possible nucleosynthesis outcomes, i.e., which progenitor regions are most likely to contribute to heavy-element formation. The peak temperature of a trajectory is an important parameter for nucleosynthesis. Matter enters the nuclear statistical equilibrium (NSE) for high temperatures. In this phase, photo-dissociation processes are in equilibrium with nuclear reactions [168]. Although the exact temperature at which NSE breaks down (freezeout) depends also on the matter density and composition, we use an approximate value of $T = 0.5\,\mathrm{MeV} \approx 5.8$ GK for simplicity. For a tracer heated above this threshold, the previous composition is not relevant anymore, and further nucleosynthesis is independent of its starting point in the progenitor. At low temperatures, nucleosynthesis processes occur with reduced strength and heavy-element formation becomes less probable. We assume a simplified criterion that trajectories with a peak temperature lower than $T = 1$ GK mostly retain the original composition. This original composition depends on the starting point of the tracer in the progenitor. The value of 1 GK is comparable with the study of Eichler et al. (2018) [169], which used $T < 0.8$ GK for the lowest temperature group of tracer particles.

We show the peak temperatures of ejected tracers as a function of their initial radii in Fig. 6.13. In order to distinguish different simulations, neutrino-processed tracers are shown here in the same color as shock-processed ones. In agreement with Fig. 6.10, we see that ejected tracers for the F110_R000 model start at radii greater than $5 \cdot 10^8$ cm, while particles at smaller initial radii are also ejected for higher heating factors. For these simulations, tracers that start within $3 \cdot 10^8$ cm around the center will always reach NSE. For up to $r_{\mathrm{init}} \approx 1.4 \cdot 10^9$ cm, it is possible for a tracer to reach NSE during the simulation. On the other hand, there are also tracers at this initial radius that always stay

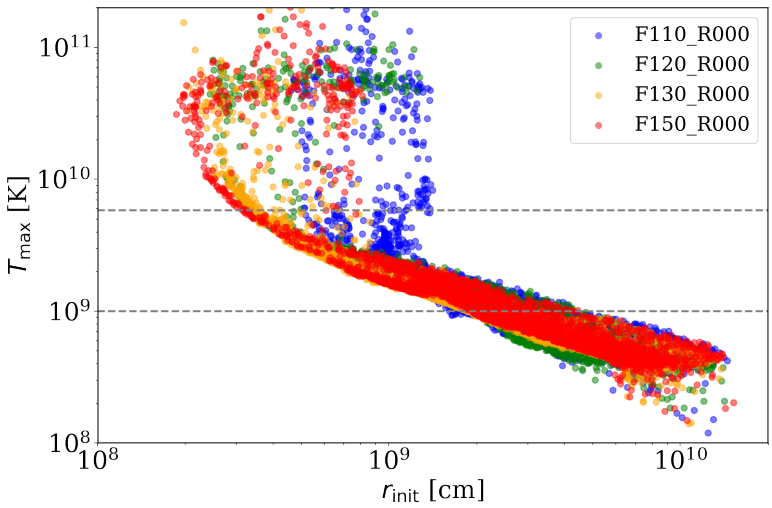

Figure 6.13.: Initial tracer radii and their peak temperatures. The gray dashed lines correspond to peak temperatures of $T = 1$ GK and $T = 5.8$ GK. We show only every second tracer for better visibility.

below $T = 1$ GK. In our simulations, the shock reaches this radius at $0.7 - 1.3$ s after the explosion time t_{exp} (up to 2 s after bounce). Matter situated beyond $r_{\mathrm{init}} \approx 4.4 \cdot 10^9$ cm generally never gets heated above this threshold. Model F130_R000 is an exception here, where this holds already for all tracers starting at $r_{\mathrm{init}} > 3.3 \cdot 10^9$ cm. This is due to the more spherical explosion of this model and less accretion, which prevents particles from coming close to the PNS.

The direction in which a tracer is ejected can have significant impact on its nucleosynthesis. We quantify this by grouping the ejected tracers into three angular bins of equal size (each $60°$ wide), into which they are ejected. The tracers are assigned to the angular bins based on their final positions. For every timestep, we can then calculate the mean temperature of each angular bin. Figure 6.14 shows this mean temperature as a function of the time for the different models. Note that for this plot we only include tracers that start within 10.000 km around the center, because the outer layers generally show a different temperature pattern as they do not come as close to the PNS. We also include only ejected tracers with a final radius of at least 10.000 km, because those further inside could only be temporarily unbound at the final simulation time, but have a big impact due to their high temperatures near the PNS.

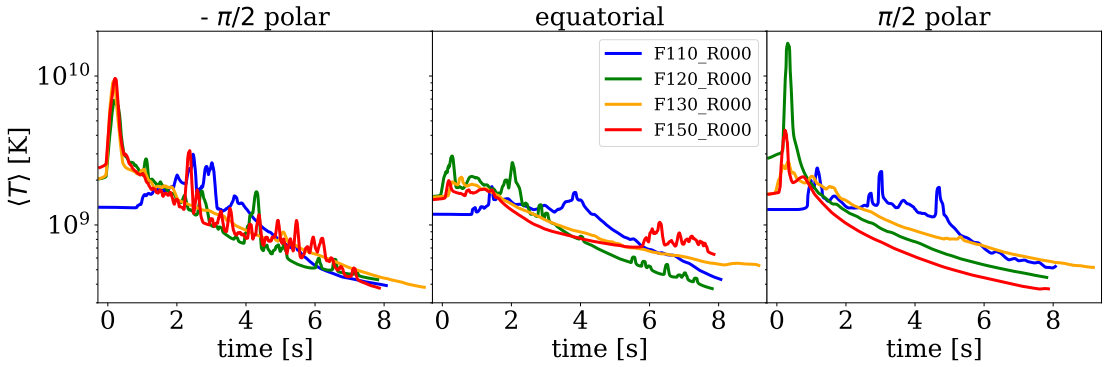

Figure 6.14.: Mean temperatures over time of tracers that are ejected into different directions. The tracers are binned based on their final positions.

For the F120_R000, F130_R000 and F150_R000 models, the impact of shock revival can be seen in the local maxima in both polar directions, into which the shock expands primarily. With time, the shock and the tracers therein cool, as they reach larger radii and cooler regions. The shock revival peak is the highest for the F120_R000 case in the polar direction where the dominant downflow (see Fig. 6.3) originates from. Tracers can come very close to the PNS because of the downflow, which results in higher mean temperatures. The bipolar shock expansion decreases the shock revival peak for tracers ejected in the equatorial plane. This is in agreement with Fig. 6.9, where we can see that neutrino-processed tracers (i.e., those that come close to the PNS and reach higher temperatures) are preferably ejected in the polar directions. For the late exploding model F110_R000, we see a different behavior. Initially, the mean temperatures are lower because this model lacks ejected tracers starting close to the center, as seen in Fig. 6.10. Shock revival occurs later and the weaker explosion does not heat matter as strongly as the more energetic explosions for higher heating factors. As a consequence, the difference between different angular bins is not as pronounced. Continued downflows lead to a constant supply of hot tracers in the subsequent seconds, which increase the mean temperatures to comparably high values. Around $t = 4$ s, the ejected tracers of model F110_R000 have the highest mean temperature in all directions.

The following two plots show trajectories of individual tracers over time. The radius evolution is shown in Fig. 6.15, where we again highlight neutrino-processed tracers with black colors. Here, we only show every 50th trajectory to avoid a messy picture. We can identify the collapse of the center by the inwards directed trajectories of the

innermost tracers around bounce. Later on, the expanding shock takes the majority of shock-processed particles with it towards larger radii. Individual tracers also approach the PNS at late times with a typical infall-outflow radius evolution. Especially in model F110_R000, continued downflows bring tracer near the PNS at later times, in agreement with the larger mean temperatures as seen in Fig. 6.14. We can furthermore identify the mixing of neutrino-processed and shock-processed tracers (compare to Fig. 6.12) in all simulations. The individual trajectories of neutrino-processed tracers can have very different patterns. While some particles come closer than 100 km to the PNS, others have minimum radii of more than 1000 km. Likewise, the ejection velocities and final radii can differ greatly, which is in agreement with the smeared out radial distribution at late times as shown in Fig. 6.12 for model F130_R000.

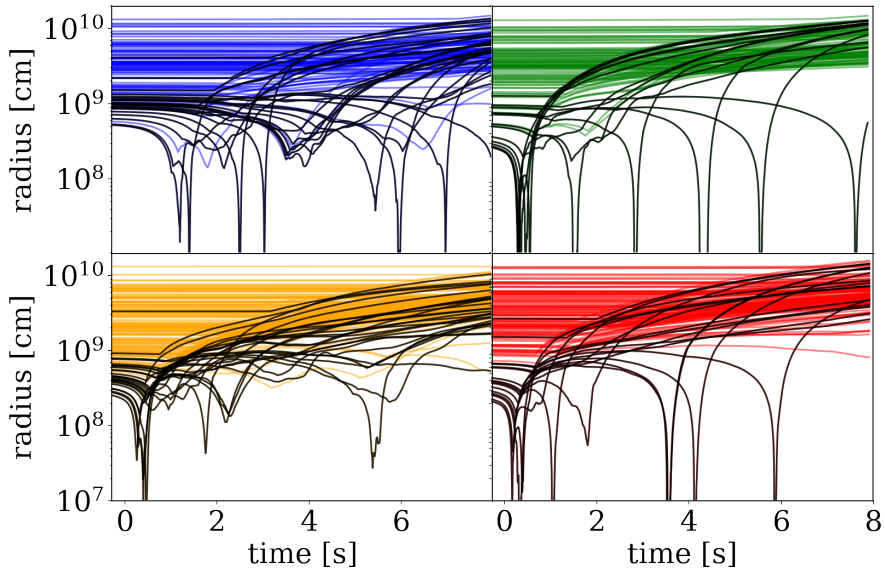

Figure 6.15.: Radius vs. time for tracers. The color code follows Fig. 6.8, black lines represent neutrino-processed tracers. We show only every 50th tracer for better visibility.

We also show the temperature evolution of each trajectory, in Fig. 6.16. The impact of the shock on tracers in the outer region results in a sudden temperature increase when the shock arrives at their position. The temperature evolution of all tracers in a simulation also follows the decreasing shock temperature to values below 1 GK. As also seen in the radius evolution, individual trajectories within the group of neutrino-processed tracers

can be very different. Particles with minimum radii of less than 100 km are heated to more than 10 GK, while those who do not come as near to the PNS have peak temperatures of only a few GK. We conclude that the group of neutrino-processed tracers is likely a very heterogenous one in the nucleosynthesis outcome. However, it can still be distinguished from the shock-processed group, where no tracer reaches the NSE-temperature of $T = 5.8$ GK.

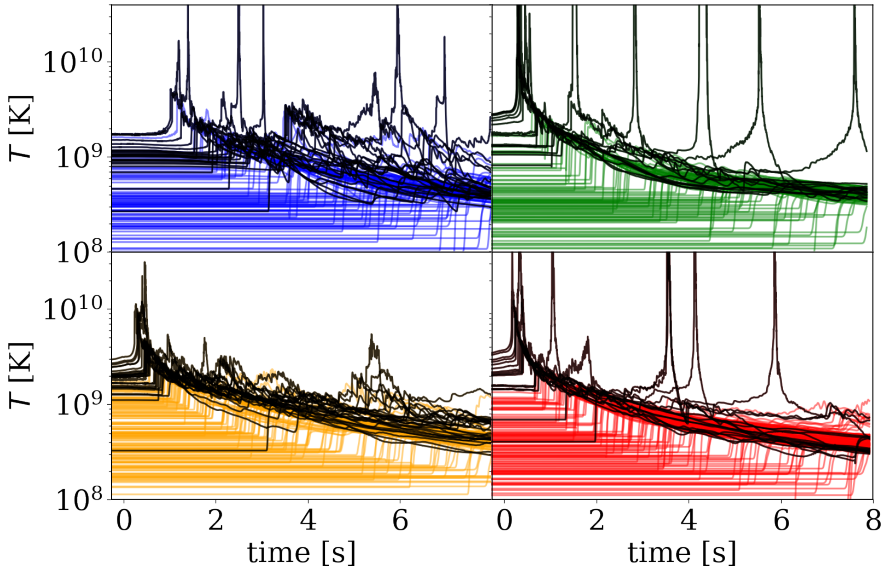

Figure 6.16.: Temperature vs. time for tracers. The color code follows Fig. 6.8, black lines represent neutrino-processed tracers. We show only every 50th tracer for better visibility.

Finally, we aim to give predictions for the nucleosynthesis outcome in our simulations. Because the use of the gray neutrino leakage scheme results in inaccurate neutrino energies and luminosities, thus also electron fractions (see Sec. 4.2.1), we do not perform nuclear reaction network calculations for the models presented here. However, we can still make general assumptions based on the dynamic behavior of tracers. Besides the electron fraction, two other parameters are suitable for the prediction of heavy-element formation, namely the entropy and the dynamic timescale at NSE-freezeout ($T = 5.8$ GK). For the latter one, we use the definition already mentioned in chapter 5, taking the ratio of radius and velocity at $T = 5.8$ GK. Naturally, for these calculations we only include tracers with $T_{\max} \geq 5.8$ GK, which are between $5-8$ % of all ejected tracers, depending on the model.

We show the time t_{NSE}, at which tracers experience NSE-freezeout and the current radius at that time, in the top panel of Fig. 6.17. In the bottom panel we show the entropy at $T = 5.8$ GK, while the dynamic timescale is color-coded. Some tracers that dwell in the vicinity of the PNS for a long time can have dynamic timescales of $\tau_{\mathrm{dyn}} \gg 100$ ms, but we neglect them in this figure. For a more comprehensive image, we include particles from all simulations shown in Fig. 6.8.

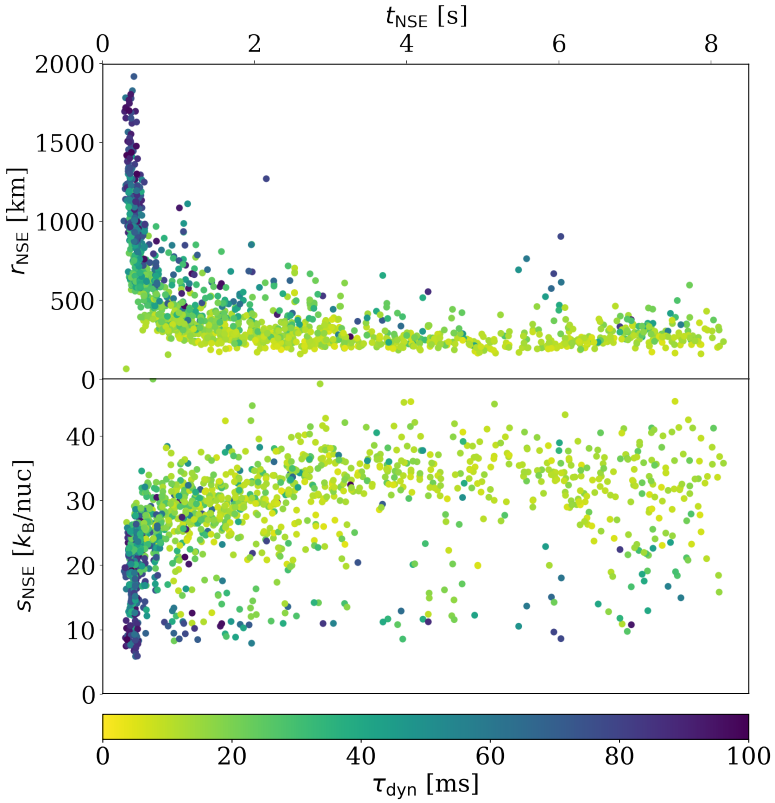

Figure 6.17.: Simulation time at NSE-freezeout for tracers vs. the radius at NSE-freezeout (top panel) and the entropy at that time (bottom panel), with the dynamic timescale color-coded. This figure includes tracers from all simulations shown in Fig. 6.8.

We see that at the time of shock revival, during the first half second, the majority of tracers leave NSE at a comparably large radius of $r_{\mathrm{NSE}} > 1000$ km. These are the particles that are

carried away with the early shock expansion, leaving NSE when the shock temperature drops below $T = 5.8$ GK at a comparably large radius. The mean radius of NSE-freezeout decreases subsequently and saturates at a few hundred kilometers after about 1 s. The tracers ejected at this and later times are neutrino-processed, having come close to the PNS in downflows and ejected with high velocities. Consequently, the mean dynamic timescale also decreases in the later phases of the simulation. When comparing averages in the two time intervals $0 < t_{\mathrm{NSE}} < 1$ s and $3 < t_{\mathrm{NSE}} < 9$ s, we see a decrease in r_{NSE} from (806 ± 359) km to (283 ± 91) km. For the nucleosynthesis relevant parameters, the dynamic timescale τ_{dyn} decreases from (45 ± 25) ms to (17 ± 14) ms, while the entropy s_{NSE} increases from $(23 \pm 6)\ \mathrm{k_B/nuc}$ to $(31 \pm 8)\ \mathrm{k_B/nuc}$.

Large entropies and small timescales are beneficial for the formation of heavy elements. We can see from Fig. 6.17 that this is the case several seconds after bounce in our simulations. The majority of matter is ejected in the first second after shock revival. However, its potential for heavy-element formation, as estimated from the entropy and dynamic timescale, is considerably smaller than that of matter ejected at later times. For the whole picture of nucleosynthesis, it is therefore crucial to also include tracers that are ejected several seconds after bounce. Once again, this highlights the importance of long-time simulations for an accurate estimate of the nucleosynthesis outcome in CCSN.

7. Simulations of multiple progenitor stars

We conclude our study by applying our setup from chapters 4 & 5 to different progenitor stars. In addition to the $15\ M_\odot$ star from Woosley et al. (2002) [37], hereafter labeled s15.0, we choose one progenitor model with lower and one with higher mass from the same series. Specifically, we employ the s11.2 and s27.0 models (with masses of $11.2\ M_\odot$ and $27\ M_\odot$, respectively). These progenitors have also been studied in the literature (e.g., Ref. [41, 64, 136, 150] use the s11.2 and Ref. [137, 150] the s27.0 model), which allows for a comparison of general features with our setup. We first discuss differences in the individual progenitor structures with special focus on the compactness parameter. The performed simulations reveal similarities and differences to the s15.0 model, of which we highlight the impact of rotation and the growth rate of the explosion energy.

7.1. Progenitor properties and models

We give some general properties of the different progenitor models. We use the same simulation setup as before, with a domain size of $1.6{\cdot}10^{10}$ cm. The enclosed masses within the domain are then $2.06\ M_\odot$ and $8.89\ M_\odot$ for the s11.2 and s27.0 model, respectively, compared to $3.84\ M_\odot$ for the s15.0 progenitor. The mass coordinate of the Si/O interfaces (which we define analogous to Ref. [136]) is at $M_{\mathrm{Si/O,s11.2}} = 1.39\ M_\odot$ and $M_{\mathrm{Si/O,s27.0}} = 1.85\ M_\odot$, compared to $M_{\mathrm{Si/O,s15.0}} = 1.72\ M_\odot$. We also use the same setup for the angular momentum profile as before, with a characteristic radius of $r_A = 3000$ km. Although this radius is positioned at different shells within different progenitors, we use the same value for a meaningful comparison. The total angular momentum within the domain is then calculated to be $J_{\mathrm{tot,s11.2}} = \Omega_0 \cdot 0.83 \cdot 10^{50}\,\mathrm{g\,cm^2}$ and $J_{\mathrm{tot,s27.0}} = \Omega_0 \cdot 8.45 \cdot 10^{50}\,\mathrm{g\,cm^2}$, compared to $J_{\mathrm{tot,s15.0}} = \Omega_0 \cdot 2.55 \cdot 10^{50}\,\mathrm{g\,cm^2}$. We use three different variations of the angular momentum, which include one moderately ($\Omega_0 = 0.03{\cdot}2\pi$ rad/s) and one rapidly rotating case ($\Omega_0 = 0.20 \cdot 2\pi$ rad/s), in addition to the default, non-rotating progenitor models.

The compactness parameter introduced by O'Connor & Ott (2011) [58] is a suitable measure for the explodability of progenitor models. It has been used in numerous multi-progenitor studies (e.g., see Ref. [58–60, 68, 170]) to make systematic assumptions about general explosion features and the progenitor-remnant connection across the progenitor mass range. However, other studies call for more refined approaches than just a single-parameter criterion [61, 62]. For a given mass coordinate M, located at a radius $R(M)$ in the spherically-symmetric progenitor model, the compactness parameter is given by

$$\xi_M = \frac{M/M_\odot}{R(M)/1000\ \mathrm{km}}\,. \tag{7.1}$$

We use the definition of the compactness parameter at a mass coordinate of $1.75\ M_\odot$, evaluated before collapse. It has a value of $\xi_{1.75} = 0.07$ for the s11.2 progenitor, while the other models have compactnesses of 0.54 and 0.53 for s15.0 and s27.0, respectively [137, 150]. The latter ones can be classified as high-compactness models, while s11.2 is a low-compactness case [68]. From this criterion, we expect a similar explodability of the s27.0 model as in our previous s15.0 simulations, while the s11.2 progenitor is supposed to explode much easier.

In agreement with this assumption, we see successful and comparably early shock revival in the s11.2 already for $f_\mathrm{heat} = 1$, while the explosion threshold for the s27.0 progenitor lies at $f_\mathrm{heat} = 1.05$. We thus conduct only F100 cases for the low-mass progenitor, while for the high-mass model we calculate F105, F110, F120 and F130 series. In the following, we extend the previously used labels by a preceding "s11_" for the s11.2 progenitor, and a preceding "s27_" for the s27.0 progenitor.

7.2. Explosion phase

We show the explosion times of the different models in Fig. 7.1. In total, we now have eleven more exploding simulations, in addition to those in chapter 5. We see that progenitor s11.2 is easily explodable without artificially increased neutrino heating, in agreement with the prediction from its compactness parameter. The non-rotating model has an explosion time of $t_\mathrm{exp} = 0.16$ s, which is the smallest for all simulations performed in this study. With increasing rotation we see a delayed shock revival, which agrees with the results of chapter 5, but even the rapidly rotating case explodes comparably fast. In contrast, the s27.0 progenitor shows a similar explosion behavior than the s15.0 one (compare to Fig. 5.4). The correlation of the heating factor with the explosion time is again

monotonic. We can identify one late exploding model, s27_F105_R000, which revives the shock after the passing of the Si/O shell interface, the other heating factors belong to the early exploding group. However, caution must be exercised for the late exploding model. The very late shock revival at $t = 1.41$ s could be a result of our use of Newtonian gravity. In a general relativistic treatment, neutrino luminosities can be higher and lead to earlier explosions [171], but it is also possible that by that time a black hole would have had formed, as the PNS mass is already $M_{\rm PNS}(t = t_{\rm exp}) \approx 2.0\ M_\odot$. We see that rotation has a similar effect on the explodability than before for the s15.0 progenitor. In the late exploding case, moderate rotation is enough to suppress shock revival altogether, while for the F110 and F120 models, the R003 variation explodes, while the R020 one does not. Only for $f_{\rm heat} = 1.30$, all models explode.

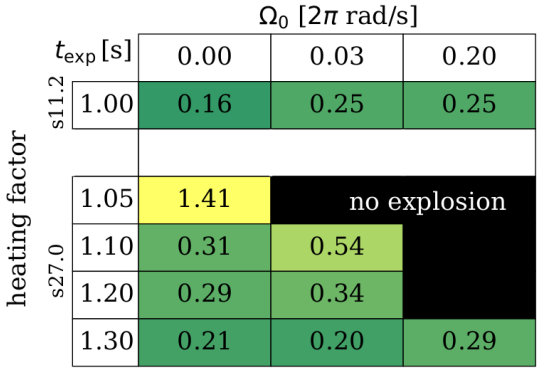

Figure 7.1.: Table with the explosion time in seconds for all models with progenitors s11.2 (upper row) and s27.0 (lower rows). The different heating factors are displayed vertically and the rotation strengths (Ω_0 in units of 2π rad/s) horizontally. Black cells indicate a failed shock revival in these models.

We can compare our results to literature values. In particular, the studies of Müller (2015) [41] and Pan et al. (2016) [137] are suitable for a comparison of s11.2 and s27.0 models, respectively. Differences to our setup include the use of a general relativistic gravity and the fast multigroup neutrino transport scheme [172] for the study in Ref. [41], and a different equation of state and the use of the isotropic diffusion source approximation [110] for neutrinos in Ref. [137]. We use the "s11.2_2Db" model of the first study for a comparison with our simulations. By applying the $R_{\rm shock,max} = 600$ km criterion for determining the explosion time, we infer values of $t_{\rm exp} \approx 0.22$ s (s11.2) and $t_{\rm exp} \approx 0.20$ s (s27.0) from these studies. These values are not too far from the ones shown in Fig. 7.1.

The delayed or failed shock revival in rotating models is in agreement with our previous results. It suggests that the reduction of the neutrino luminosity because of centrifugal forces, and the subsequent density redistribution, is a robust mechanism in our setup. Based on Fig. 5.3, we show the angle dependence of the electron antineutrino luminosity for the s11_F100 models and the s27_F130 models (Fig. 7.2), of which all are exploding. In agreement with our previous results, we see a systematically decreased luminosity in the polar directions of rotating models. The neutrino flux is generally smaller for the s11.2 models compared to both other progenitors, which have similar total luminosities. The positive correlation of the neutrino luminosity with the compactness has also been found in other studies [136, 150]. In the equatorial direction, the luminosities are not as strongly affected by rotation, which again follows the same arguments made in Sec. 5.3.

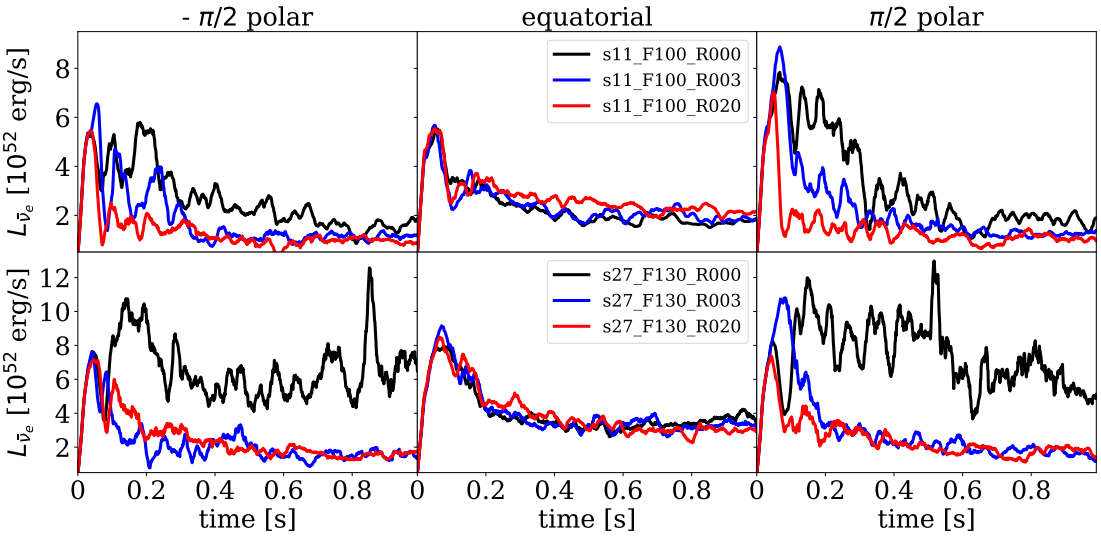

Figure 7.2.: Electron antineutrino luminosities for non-rotating (black), moderately (blue) and rapidly rotating (red) models for the s11_F100 series (top row) and the s27_F130 (bottom row) series as seen from an observer in the direction of the poles (left and right panel) or the equatorial plane (center panel). Note the different scalings on the y-axes.

Other simulation key quantities at early times show a similar trend to those of the previously calculated s15.0 models. The accumulated explosion energy at 100 ms after shock revival (compare to Tab. 4.1) for the non-rotating models is $E_{\mathrm{dia,100ms}} = 0.04$ B for the

s11.2 and $E_{\mathrm{dia},100\mathrm{ms}} = 0.05 - 0.07$ B (depending on the heating factor) for the s27.0 progenitor. At this time, we can also see the significant effect that rotation has on the shock morphology. The average shock deformation parameter for non-rotating s27 models at that time is $d_{\mathrm{shock},100\mathrm{ms}} = 0.65 \pm 0.16$ (the statistical uncertainty is due to the four different heating factors) and reduces to $d_{\mathrm{shock},100\mathrm{ms}} = 0.35 \pm 0.06$ with moderate rotation. The only rapidly rotating, successfully exploding model s27_F130_R020, even has a slightly oblate deformation shortly after shock revival, with $d_{\mathrm{shock},100\mathrm{ms}} = -0.09$. However, in the case of the s11.2 progenitor, this tight correlation does not hold and the rapidly rotating case actually has the most prolate shock morphology shortly after shock revival. We attribute this to the earlier explosion time and the overall smaller angular momentum in this progenitor. Another contribution to this difference is the shorter collapse time of only 186 ms (compared to 286 ms for the s15.0 and 296 ms for the s27.0 progenitor), which allows for less accretion of angular momentum during the formation of the proto-neutron star (PNS).

7.3. Long-time evolution

We continue the simulations up to a few seconds after bounce. According to our results in chapter 6, the majority of matter is ejected in the first seconds. We show the evolution of the shock radius in Fig. 7.3. All models of the s11.2 progenitor show a similar evolution up to $t \approx 2$ s, after which some differences between the individual rotation rates occur, leading to the rapidly rotating case to have the largest shock radius at the end of the simulation. Meanwhile, the s27_F130 models show an inverse correlation with the rotation rate, where the non-rotating case has the largest shock radius at the end. The general shock radius evolution of the s27.0 models is similar to that of the s15.0 cases.

7.3.1. Impact of rotation

We argue that since the explosion in the s11.2 progenitor occurs very early, rotation has a smaller impact than in heavier progenitors. We investigate the presumably minor impact of rotation on the explosion behavior of the s11.2 progenitor by comparing the early shock morphology of all three progenitors for selected models. In Fig. 7.4, we show the shock deformation parameter d_{shock} (see Sec. 5.4) for all s11.2 models and for the s15.0 and s27.0 models with $f_{\mathrm{heat}} = 1.30$ and the same rotation as in the lower-mass progenitor. Similar to Fig. 5.5, we see that rapidly rotating models of both the s15.0 and s27.0 series

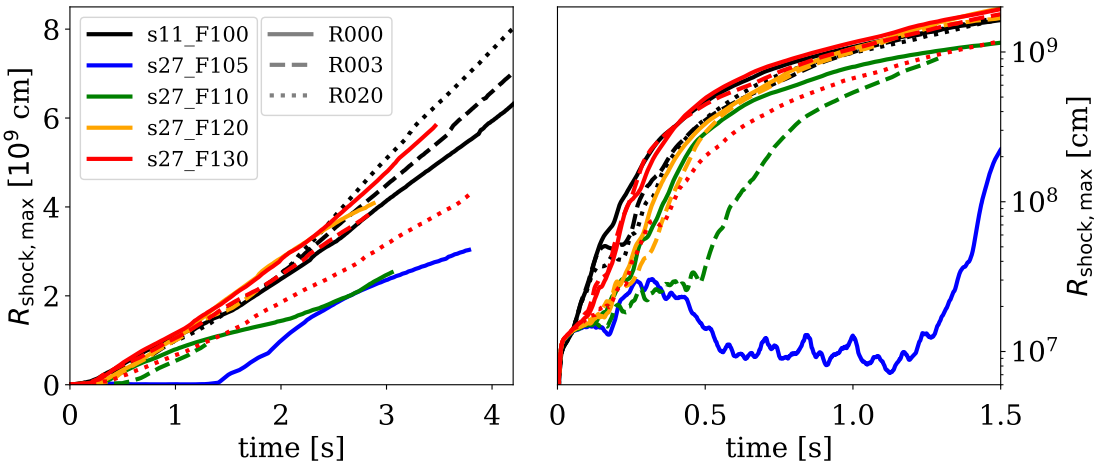

Figure 7.3.: Maximum shock radius over time for models of the s11.2 (black lines) and s27.0 (colored lines) progenitors. The right panel shows the first 1.5 s in detail with a logarithmic scale.

show a more spherical shock expansion. However, in the case of the s11.2 models, this does not hold anymore. While the non-rotating case still has the most prolate shock morphology, the difference to the rotating cases is not as pronounced and the hierarchy between the R003 and R020 rotation rates is inverted up to $t \approx 0.8$ s.

The impact of the initial rotation strength on the post-bounce evolution can be measured with the resulting spin period of the PNS. We calculate the angular velocity of the PNS as the ratio of its angular momentum and its moment of inertia, i.e., $\omega_{\mathrm{PNS}} = J_{\mathrm{PNS}}/I_{\mathrm{PNS}}$. The spin period is then the inverse of the angular velocity. We show its evolution for the different rotation rates of all progenitors in in Fig. 7.5. The initially non-rotating simulations develop no PNS spin, because of angular momentum conservation and our cylindrical geometry. We see that the two different rotation strengths, R003 and R020, can be easily distinguished. The rapidly rotating models form a PNS spinning at sub-millisecond periods within a few seconds. Efficient spin-down mechanisms to explain the observed pulsar frequencies of $\gg 1$ ms, such as magnetic braking, are still under discussion [36].

From Fig. 7.5, we can also distinguish the different progenitors. During the first second after bounce, the s15.0 and s27.0 models show a very similar spin evolution, while the period of the s11.2 progenitor is significantly higher. By the end of the simulation, the

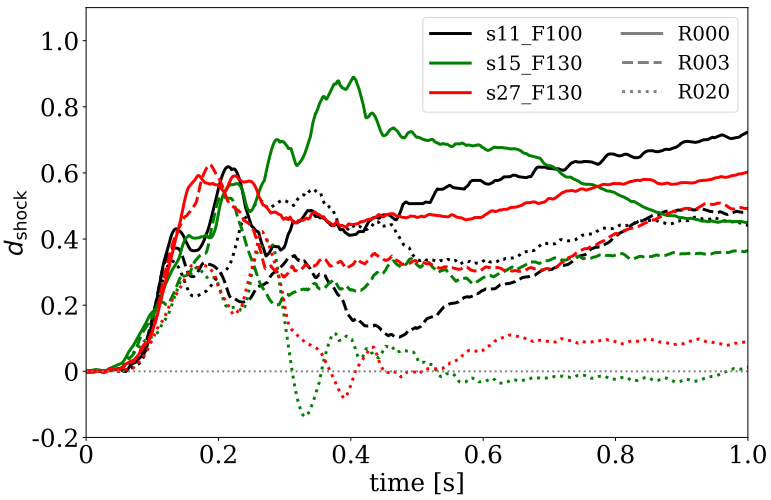

Figure 7.4.: Shock deformation parameter according to equation (5.1) for selected models of all progenitors. The dotted gray line indicates where a spherical shock morphology can be found.

s27.0 model, which also carries the most angular momentum, comes out with the fastest spinning PNS. The difference of the s11.2 progenitor to the two heavier ones also explains the less pronounced impact on the PNS surroundings, neutrino luminosities, and shock morphology.

7.3.2. Proto-neutron star mass and explosion energy

We further investigate differences in the PNS evolution from different progenitors. We show the PNS masses of different models and the corresponding mass accretion rates in Fig. 7.6. The PNS masses from the s11.2 progenitor saturate shortly after shock revival at $M_{\mathrm{PNS}} \approx 1.3 - 1.4\ M_{\odot}$, which can easily be explained by the comparably small mass accretion rate. In the s15.0 models, the saturation is reached at slightly later times with final masses of $M_{\mathrm{PNS}} \approx 1.7 - 1.8\ M_{\odot}$ (note that these values can still change later on due to ejection of matter in neutrino-driven winds, as outlined in Sec. 4.2.2). In contrast, the s27.0 progenitor cases show no signs of saturation until the end of the simulation. This is in line with the significantly higher mass accretion rate which mostly stays above $0.1\ M_{\odot}$/s. The rotating simulations show a smaller mass accretion rate, which

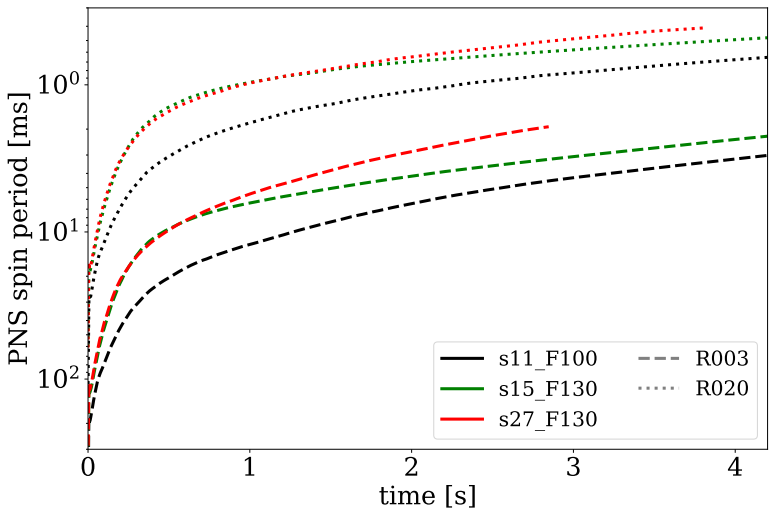

Figure 7.5.: Spin period of the PNS over time for selected models of all progenitors.

is in line with the findings in Sec. 5.5, but even the rapidly rotating s27_F130_R020 model still has enough accretion to increase the PNS mass at an almost constant rate of $\dot{M}_{\rm PNS} \approx 0.07\ M_\odot$/s. We see no neutrino-driven wind phases, i.e., where $\dot{M}_{\rm acc,500km} = 0$, in the new models.

From the studies in Ref. [41, 137], we infer PNS masses of $M_{\rm PNS} \approx 1.43\ M_\odot$ at $t = 4$ s for the s11.2 progenitor, and $M_{\rm PNS} \approx 1.70\ M_\odot$ at $t = 0.48$ s for the s27.0 progenitor. The PNS masses in our s11.2 simulations are lower than the literature value. However, in the study of Ref. [41], the PNS masses also do not saturate even after several seconds post-bounce. This feature, which appears to be a trade-off with generally low explosion energies, is also discussed in that publication. On the other hand, the inferred PNS mass at early times for the s27.0 progenitor agrees very well with our results.

The origin of the continuously higher mass accretion in the s27.0 models can be understood from the progenitor structure. We compare the density profile of the three non-rotating models in Fig. 7.6 at bounce and at $t = 3$ s, in Fig. 7.7. At bounce, the densities within the innermost 500 km are similar for all progenitors. The density then drops in the s11.2 progenitor for larger radii compared to the s15.0 and s27.0 models. Beyond $r \approx 5000$ km, the s27.0 progenitor has a substantially higher density than the other two models. This bulk of additional matter density is then accreted towards the center in the subsequent seconds. At $t = 3$ s, the density around $r = 500$ km (where we evaluate

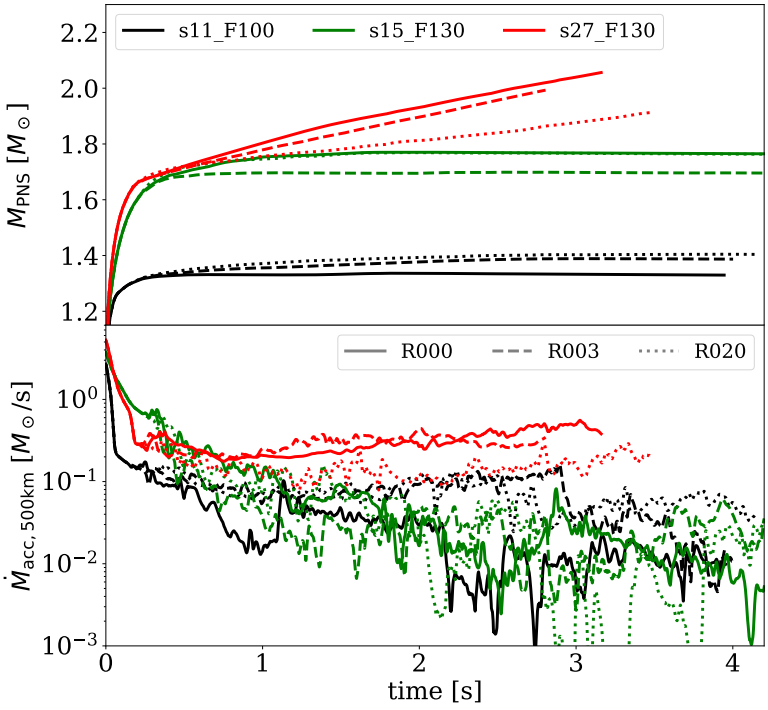

Figure 7.6.: Top panel: Evolution of PNS masses from different progenitors. Bottom panel: Corresponding mass accretion rates at $r = 500$ km.

the mass accretion rate) is almost two orders of magnitude larger than in the lower-mass progenitors. As the mass accretion rate is proportional to the density at this radius, this explains the higher values for $\dot{M}_{\rm acc,500km}$ in the s27.0 simulations. The density is also higher for larger radii, and we therefore do not expect a significant drop in the mass accretion rate soon in this model.

High mass accretion rates and persistent downflows power the supernova engine and increase the explosion energy, as we saw for simulations of the s15.0 progenitor in chapters 4 & 5. We compare the evolution of the explosion energy for all three progenitors in Fig. 7.8. Here, the green lines are identical with the solid lines in Fig. 5.7. The explosion energy of models with the lighter s11.2 progenitor is generally smaller, which results from the overall smaller gravitational binding energy that is available for the explosion. The non-rotating model accumulates the smallest explosion energy, which is in accordance with its smaller mass accretion rate (Fig. 7.6). In contast, the s27.0 progen-

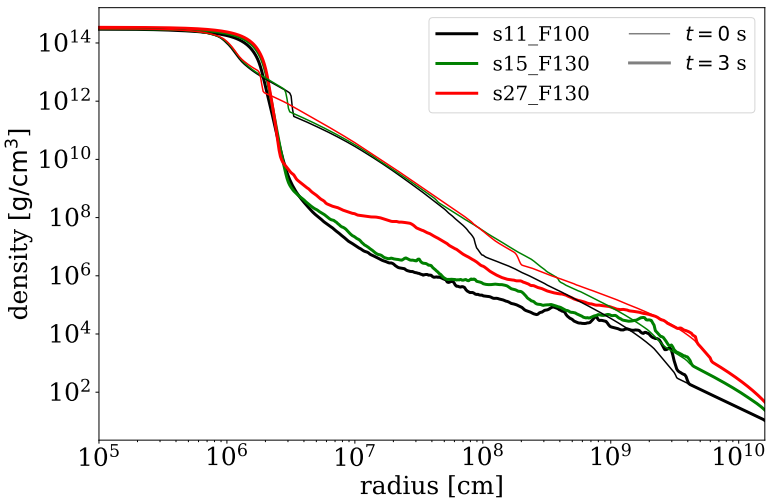

Figure 7.7.: Density profile of non-rotating models from the three different progenitors at bounce (thin lines) and at $t = 3$ s (thick lines). The radial profile is calculated from an average over all angles.

itor simulations, specifically the R000 and R003 ones, build up much more energy at a considerably higher rate. This is also in agreement with the higher mass accretion rates in these models.

We again compare these values to the studies in Ref. [41, 137]. In the case of the s11.2 progenitor, the explosion energy in our models is considerably larger than the value of $E_{\mathrm{dia}} \approx 0.07$ B (at $t = 4$ s) given in the literature. However, the definition in Ref. [41] also includes a positive radial velocity as criterion for matter to be unbound. Furthermore, the unusually smaller explosion energies and larger PNS masses are discussed there. The literature value for the explosion energy of the s27.0 progenitor is $E_{\mathrm{dia}} = 0.157$ B at $t = 0.48$ s. This is in excellent agreement with our s27_F130_R000 model, which has an explosion energy of $E_{\mathrm{dia}} = 0.154$ B at that time.

We compare the explosion energy growth rate in relation to the mass accretion rate to confirm our results from Sec. 5.4.2 also for other progenitors. The similar slopes in the explosion energy for the s11.2 and s15.0 models suggest a robust dependence on the mass accretion rate. We therefore revisit the relation that we found in Fig. 5.8. In Fig. 7.9, we show the same averaged line with $0.675\,\sigma$ confidence interval. We omit the individual dots from the s15.0 progenitor series to avoid a messy image and extend the axes to larger

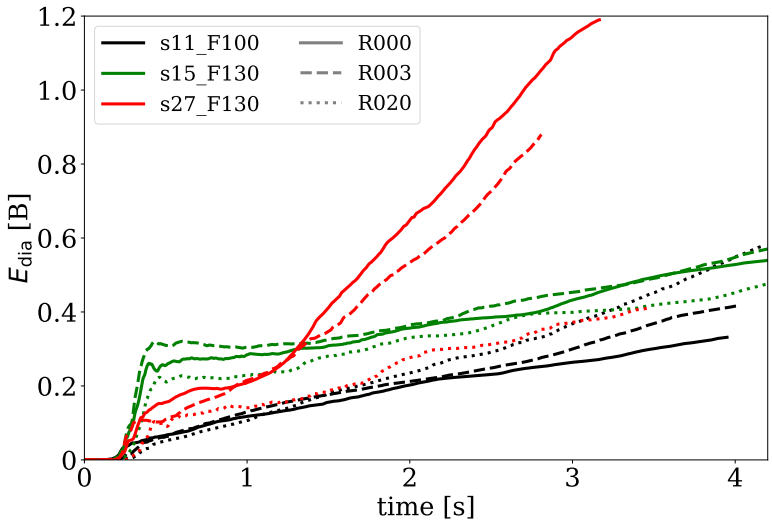

Figure 7.8.: Explosion energy evolution for selected models of all progenitors.

values of $\dot{M}_{\rm acc,500km}$ and $\dot{E}_{\rm dia}$, because the s27.0 simulations have $\dot{M}_{\rm acc,500km} > 0.1\ M_\odot$/s at most times. We then continue to overplot the average values for $\dot{M}_{\rm acc,500km}$ and $\dot{E}_{\rm dia}$ during the last second of each of the new exploding simulations. This allows us to see if they fit in the relation predicted by the s15.0 models.

The black crosses mark the last-second average values of the s11.2 models, and the red crosses the same of the s27.0 models. In agreement with our previous results, we see that the average mass accretion rate is higher in all s27.0 simulations, compared to the s11.2 ones. Furthermore, a high mass accretion rate leads to a significantly higher explosion energy growth, and the s27.0 average values represent the trend predicted before rather well. For phases of less accretion, the s11.2 average values are also in very good agreement with our previous results. This shows that the relation of mass accretion rate and explosion energy growth in our simulation setup is not progenitor-specific, but holds also for other choices than the s15.0 case.

We conclude that there are similar trends for different progenitors. The explodability of the non-rotating models follows predictions from the compactness parameter and is similar for the s15.0 and s27.0 models. The detrimental effect of rotation on shock revival follows the same trend, with the characteristically smaller neutrino luminosities at the poles. For the s11.2 progenitor, the explodability and effects from rotation show dif-

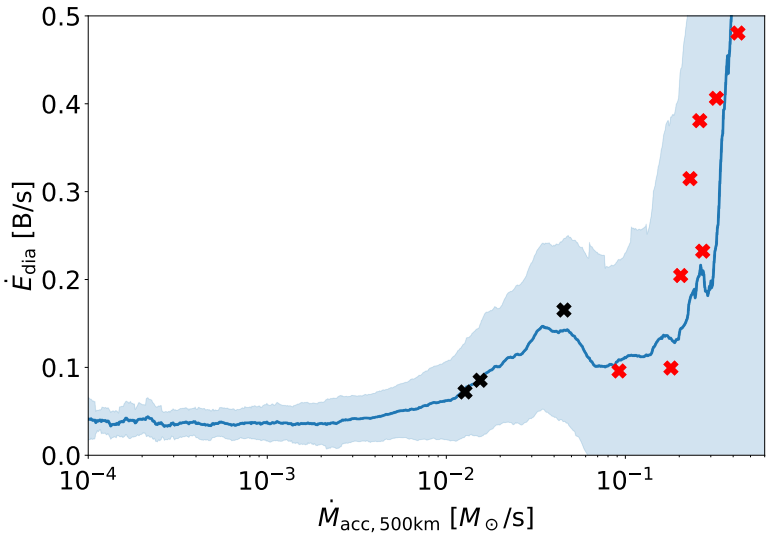

Figure 7.9.: The same plot as in Fig. 5.8, but with extended axes and omitting the individual data points for a clearer picture. The black and red crosses show the mean values during the last second of the simulations of the exploding s11.2 and s27.0 models, respectively.

ferences, but these are in agreement with the different compactness and collapse time. We found the reason for the large PNS masses, explosion energies, and mass accretion rates of the s27.0 models in the progenitor structure. The impact of mass accretion on the explosion energy growth is in agreement with our previous results. However, further studies with state-of-the-art setups, including a sophisticated neutrino transport scheme, a three-dimensional geometry and general relativistic gravity, need to be conducted in the future for a more comprehensive image of the progenitor dependence on the CCSN long-time evolution.

8. Summary & Outlook

There remain many open questions in the research on core-collapse supernovae (CCSN). Significant improvements of models, theory, and observations have increased our understanding in the recent decades. The collapse of the inner core of a progenitor star and the subsequent bounce, shock stalling, and shock revival can now be investigated in multi-dimensional simulations. However, a comprehensive study of the first several seconds after bounce in three dimensions and with state-of-the-art neutrino transport and general relativity is not feasible yet [36]. Sensible simplifications allow for broader parameter studies, which in turn contribute to our knowledge of the long-time evolution of CCSN.

In this study, we presented a series of long-time simulations of CCSN in an axisymmetric geometry. We chose a simplified setup that allowed us to calculate up to ten seconds after bounce for a variety of different models. We used the built-in heating factor in the neutrino leakage scheme in FLASH [70–73] to systematically investigate the impact of the neutrino heating rate on the explosion. For our goal of long-time simulations, we had to consider changes to the original implementation in Sec. 4.1. As a first step, we restricted the effect of f_{heat} to the gain region. This minimized its artificial impact on the proto-neutron star (PNS) and removed the bias of the original implementation on the neutrino luminosities. Secondly, we implemented a linear decrease to the default value of $f_{\mathrm{heat}} = 1$ after successful shock revival. The artificially high growth rate of the explosion energy due to the additional heating was thus removed.

With this fixed and tested setup at hand, we continued to conduct long-time simulations for different initial heating factors in Sec. 4.2. We obtained successful explosions for six out of eight models, which we could separate in two distinct groups of early and late exploding cases. An investigation of the progenitor structure and the infalling mass shells revealed the importance of the Si/O interface for shock revival. The decrease in density and pressure that follows this shell interface results in a drop of the ram pressure, which allows the shock to expand. In the long-time evolution, we highlighted the differences that arise from different explosion morphologies. Monopolar explosions suffer

from strong and long-lasting downflows and a high mass accretion rate. This higher mass accretion rate increases the neutrino luminosities and can lead to a considerable growth of the explosion energy at late times.

We continued to investigate the impact of rotation on a CCSN in chapter 5. We expanded our parameter space by considering six additional models with different rotation strengths for each of the successfully exploding heating factor variations. The effect of an additional angular momentum was already prominent at bounce. Centrifugal forces lead to a shift of the local matter density towards the equatorial plane. This results in a reduced neutrino luminosity at the poles and thus less support for the stalled shock. We found that rotation can prevent or delay shock revival, with only 15 of the 36 new models successfully exploding. The long-time evolution revealed differences in the shock and PNS morphology due to centrifugal forces. With now a total of 21 exploding simulations at hand, we were able to quantify the impact of mass accretion on the explosion energy growth and found a robust value of $\dot{E}_{\mathrm{dia}} \approx 0.04$ B/s in the absence of accretion. Finally, we investigated the impact of rotation on the formation of neutrino-driven winds (NDW) in Sec. 5.5. We could quantify the correlation of the rotation strength with the mass accretion and the time spent in a NDW phase. One of our main results is that although rotation weakens the explosion early on, it leads to a higher probability for a neutrino-driven wind at late times.

The ejecta properties of a CCSN were our main focus in chapter 6. We developed a tracer particle method (TPM) that allowed us to track individual fluid elements over the course of the simulation. We gave a detailed description of our procedure in Sec. 6.1. The TPM includes a tracer placement method which is also applicable post-bounce and can be restricted to specific regions of interest. Our proportional-to-mass algorithm results in an equal mass for each tracer, which later proved to be useful for the analysis of the simulation results. We carefully tested our tracer scheme in Sec. 6.2. We investigated its accuracy, its convergence for different numbers of particles, and the numerical performance of the TPM. Results for our exploding simulations of the preceding chapters were given in Sec. 6.3. We distinguished two groups of ejected tracers, namely shock-processed and neutrino-processed ones, throughout our discussion. The dependence of the long-time evolution on the initial tracer position was highlighted, with differences emerging from models with different heating factors. The peak temperature, an important parameter for the estimate of nucleosynthesis, crucially depends on the initial radius of a fluid element, and matter situated beyond a certain radius is unlikely to contribute to heavy-element formation. We saw that ejecta in different directions experience different temperatures throughout their trajectories, which links to the shock morphologies discussed before. Finally, we estimated the potential for heavy-element formation based on the dynamic

behavior of tracers. We found that tracers ejected several seconds after shock revival have a higher entropy and a smaller dynamic timescale on average. This highlights the importance of the long-time evolution and the late ejected matter for nucleosynthesis.

In the final episode of our results, we conducted long-time simulations with two different progenitor stars than before. We performed a total of 15 new simulations, of which 11 successfully exploded, in chapter 7. We confirmed our previous result that rotation has a detrimental effect on shock revival and alters the neutrino luminosities at the poles of the PNS. The effect of rotation on the lighter-mass progenitor was found to be smaller, as a consequence of the shorter collapse time and reduced mass accretion at late times. In contrast, the higher-mass progenitor showed a comparably large mass accretion rate even seconds after shock revival, and a consequently increased explosion energy. We could identify differences in the progenitor structure as a reason for this behavior. The relation of the mass accretion rate with the explosion energy growth was revisited and we found that our previous results also hold in different progenitor stars.

For this study, we performed a total of 59 two-dimensional CCSN simulations. We followed the 32 successfully exploding models for several seconds after bounce and studied the long-time evolution in detail. Although we use a simplified setup compared to current state-of-the-art simulations, we could study general trends and explore fundamental correlations. Our tracer scheme can be a useful tool for future studies by providing realistic trajectories for nucleosynthesis calculations. The main goal for the upcoming research on the long-time evolution of CCSN should be an improved performance of more sophisticated setups. With a new generation of computational resources, it will be interesting to see if the current results can be confirmed by three-dimensional simulations with accurate neutrino physics and general relativity. The focus on ejecta properties as provided by tracer particles can also open the window to broader comparison studies with observations, and thus shed more light on the accuracy of current models. The recent years have brought significant improvements in all areas of CCSN simulations, and we are on a good track to finally solve the supernova puzzle and explore the origin of the elements.

A. Simulation setup

FLASH 4.2.2

git repository nuc-astro - branch: setup_MaxW - commit: 41ab445

FLASH setup line:

```
./setup CoreCollapse/Tracer -auto -2d +cylindrical -objdir "${
    simulationDirName}/source" -nxb=16 -nyb=16 -site max.tu-
    darmstadt.de threadBlockList=False +pm4dev threadWithinBlock
    =False +newMpole +uhd \
--with-unit=physics/RadTrans/RadTransMain/NeutrinoLeakage \
--with-unit=physics/sourceTerms/Deleptonize \
--with-unit=physics/Eos/EosMain/Hybrid \
```

compiler flags:

```
f compiler flags:
/home/aj19ugij/tools/mpich/bin/mpifort -c -g -r8 -i4 -O3 -
    real_size 64 -diag-di
sable 10120 -mcmodel medium -shared-intel -I /home/aj19ugij/
    tools/hdf5/include
-DH5_USE_16_API -DMAXBLOCKS=1000 -DNXB=16 -DNYB=16 -DNZB=1 -
    DN_DIM=2
c compiler flags:
/home/aj19ugij/tools/mpich/bin/mpicc -I/home/aj19ugij/tools/
    hdf5/include -DH5_U
SE_16_API -I/home/aj19ugij/tools/mpich/include64 -c -O3 -g -
    D_LARGEFILE64_SOURC
E -D_FORTIFY_SOURCE=2 -diag-disable 10120 -DMAXBLOCKS=1000 -
    DNXB=16 -DNYB=16 -D
NZB=1 -DN_DIM=2
```

The following is an example FLASH parameter file for the s15_F130_R020 simulation with the standard setup, as used in chapter 5. Note that there are linebreaks in long strings and comments.

```
# Parameters file for core-collapse SN

# Simulation basics
basenm                          = "/work/projects/Project00350/
   runs/F130_R020/ccsn2d_"
restart                         = .true.
checkpointFileNumber            = 9297
plotFileNumber                  = 0
run_comment                     = "CoreCollapse 2D with leakage"


# IO
checkpointFileIntervalStep      = 0
checkpointFileIntervalTime      = 0.001
plotFileIntervalStep            = 0
plotFileIntervalTime            = 0.000
wall_clock_time_limit           = 21000000.

plot_var_1  = "dens"
plot_var_2  = "temp"
plot_var_3  = "ye  "
plot_var_4  = "sumy"
plot_var_5  = "velx"
plot_var_6  = "vely"
plot_var_7  = "velz"
plot_var_8  = "eint"
plot_var_9  = "gpot"
plot_var_10 = "entr"
plot_var_11 = "ener"
plot_var_12 = "pres"
plot_var_13 = "gamc"
plot_var_14 = "lun1"
plot_var_15 = "lun2"
plot_var_16 = "lun3"
```

```
plot_var_17 = "lue1"
plot_var_18 = "lue2"
plot_var_19 = "lue3"
plot_var_20 = "tau1"
plot_var_21 = "tau2"

# Time
tinitial                        = 0.0
tmax                            = 10.0
nend                            = 10000000
tstep_change_factor             = 1.5
dtinit                          = 1.E-7
dtmax                           = 1.E5
dtmin                           = 1.E-20

# Domain
geometry          = "cylindrical"
xmax              = 16.e9
xmin              = 0.0
ymin                    = -16.e9
ymax                    =  16.e9
xl_boundary_type = "reflect"
xr_boundary_type = "outflow"
yl_boundary_type = "outflow"
yr_boundary_type = "outflow"

# Grid/Refinement
nblockx                     = 20 #def: 5
nblocky                     = 40 #def: 10
nblockz                     = 1

gr_lrefineMaxRedDoByLogR    = .true.
gr_lrefineMaxRedDoByTime    = .FALSE.
gr_lrefineMaxRedLogBase     = 10.0
gr_lrefineMaxRedRadiusFact  = 0.15
gr_lrefineMaxRedTRef        = 2.0
gr_lrefineMaxRedTimeScale   = 0.5
```

```
lrefine_max                   = 11 #def: 9
nrefs                         = 2
lrefine_min                   = 1
refine_var_1                  = "dens"
refine_var_2                  = "pres"
refine_var_3                  = "entr"
refine_var_4                  = "none"
refine_cutoff_1                   = 0.8
refine_cutoff_2                   = 0.8
refine_cutoff_3                   = 0.8
refine_cutoff_4                   = 0.8

# Simulation
model_file   = "progenitors/s15_whw02_ye.1d"
nsub         = 4
conserveAngMom = .false.
# Additional rotation profile
rot_omega = 0.20
rot_a = 3e8

# Hydro
useHydro                      = .TRUE.
cfl                           = 0.5
interpol_order                = 1
updateHydroFluxes             = .TRUE.
eintSwitch                            = 0.0 # Always use Etot
convertToConsvdForMeshCalls   = .false.
converttoconsvdinmeshinterp   = .false.
hole_radius = 80.e5

##  SWITCHES SPECIFIC TO THE UNSPLIT HYDRO SOLVER
                ##
#       I. INTERPOLATION SCHEME:
order                 = 3         # Interpolation order (first/
   second/third/fifth order)
slopeLimiter          = "hybrid"  # Slope limiters (minmod, mc,
   vanLeer, hybrid, limited)
LimitedSlopeBeta      = 1.        # Slope parameter for the "
```

```
   limited" slope by Toro
charLimiting          = .true.    # Characteristic limiting vs.
   Primitive limiting

use_avisc             = .true.    # use artificial viscosity (
   originally for PPM)
cvisc                 = 0.1       # coefficient for artificial
   viscosity
use_flattening        = .true.    # use flattening (dissipative)
    (originally for PPM)
use_steepening        = .false.   # use contact steepening (
   originally for PPM)
use_upwindTVD         = .false.   # use upwind biased TVD slope
   for PPM (need nguard=6)
flux_correct          = .true.
EOSforRiemann         = .false.
transOrder            = 1
use_auxEintEqn        = .TRUE.
hydroComputeDtOption = -1

#       II. RIEMANN SOLVERS:
RiemannSolver    = "hybrid"    # Roe, HLL, HLLC, LLF, Marquina
entropy          = .false.     # Entropy fix for the Roe solver

#       III. STRONG SHOCK HANDELING SCHEME:
shockDetect      = .true.      # Shock Detect for numerical
   stability
##
   ------------------------------------------------------------------##


# Gravity
useGravity                    = .true.
updateGravity                 = .TRUE.
grav_boundary_type            = "isolated"
mpole_3daxisymmetry           = .false.
mpole_dumpMoments             = .FALSE.
mpole_PrintRadialInfo         = .false.
```

```
mpole_IgnoreInnerZone         = .false.
mpole_lmax                    = 16
mpole_ZoneRadiusFraction_1    = 1.0
mpole_ZoneExponent_1          = 0.005
mpole_ZoneScalar_1                = 0.5
mpole_ZoneType_1                  = "logarithmic"
point_mass                    = 0.0
point_mass_rsoft              = 0.e0
use_gravHalfUpdate            = .TRUE.
use_gravConsv                     = .FALSE.
use_gravPotUpdate                 = .FALSE.
mpole_MultiThreading          = .false.


# EOS
eos_file = "eos_tables/LS220.h5"

eosMode      = "dens_ie"
eosModeInit  = "dens_temp"
eos_nseTemp  = 0.e9

#eos_hybTransition  = 5.e4
#eos_hybLow         = 1.e4
#eos_hybDecrease    = 1.e-2

# Deleptonization
useDeleptonize   = .true.
delep_Enu                 = 10.0 # MeV
delep_rhoOne     = 3.0e7 #3.0e7
delep_rhoTwo     = 2.0e13 #2.0e13
delep_yOne                = 0.5
delep_yTwo                = 0.278 #0.278
delep_yc                  = 0.035 #0.035
bounceTime                = 0.0 #0.248
postBounce                = .false.
useEntr                   = .true.
```

```
# RadTrans/Leakage
useRadTrans                 = .true.
leak_doHeat                 = .true.
leak_heatFac        = 1.30
rt_decreaseHeatFac  = .true.
rt_decreaseHeatFac_radius = 1e8
leak_radMax                 = 3.e8
leak_radLog                 = 1.5e7
leak_dx                     = 0.5e5
leak_thtMax                 = 1.
leak_numRad                 = 1000
leak_numTht                 = 37
leak_reducedTime    = 0.020
leak_reducedSteps   = 4


# Nuclear Burning
useBurn          = .false.
nuclearDensMax   = 1.0E15
odeStepper       = 2
algebra          = 1
useEnergy        = .false.
bn_nseTemp       = 5.e9

## flags for the allAprox network
bn_useWeakReactions          = .false.
bn_usePPchain                = .false.
bn_useCNOcycle               = .false.
bn_useFePhotodisintegration  = .false.
bn_useHePhotodisintegration  = .false.
bn_useAlphaChain             = .false.
bn_useAppg                   = .false.

# Neutrino Heating/Cooling
useHeat                 = .false.
Lneut                   = 2.2e52
Tneut                   = 4.0 #MeV
heatTimeFac             = 1.0e4
```

```
useHalfState    = .false.

# Tracer particles (in-situ)
useParticles = .false.
pt_resetTag = .false.
        # WithDensity implementation
pt_numParticlesWanted = 0 #1e5 #9e5
pt_pRand = 1
        # Add From File
AddParticlesFromFile = .false.
NumNewParticles = 0 #2e4
ParticlePositions_file = ParticlePositions.txt

pt_maxPerProc = 0 #1e4
max_particles_per_blk = 0 #1e4
refine_on_particle_count = .true.
gr_ptRemove = .true.
gr_ptRemoveDensHigh = 1e12
gr_ptRemoveDensLow = 0 #1e6
particle_attribute_1 = "mass"
particle_attribute_2 = "dens"
particle_attribute_3 = "temp"
particle_attribute_4 = "pres"
particle_attribute_5 = "entr"
particle_attribute_6 = "ye"
particle_attribute_7 = "gamc"
particle_attribute_8 = "ener"
particle_attribute_9 = "gpot"

# Small numbers
smallt  = 1.2e5 #1.e-10 #1.2e5 #1.2e4
smlrho  = 1.e-5 # HYBRID EOS
smallp  = 1.E-20
smalle  = 1.E1
smallu  = 1.E-10
smallx  = 1.E-50
small   = 1.E-100
```

Bibliography

[1] Image Credit: Peter Jurik, https://cdn.now.howstuffworks.com/media-content/f0b29158-3f7f-4511-a2b2-5bfded63253f-1920-1080.jpg, accessed March 23, 2020.

[2] D. A. Green, *Highlights of Astronomy* **12**, 350 (2002).

[3] O. Krause, S. M. Birkmann, T. Usuda, *et al.*, *Science* **320**, 1195 (2008).

[4] N. Panagia, *Chinese J. Astron. Astrophys. Suppl.* **8**, 155 (2008).

[5] Image Credit: J. Hester et al. / NASA, https://hubblesite.org/contents/media/images/2002/24/1248-Image.html, accessed August 2, 2019.

[6] W. Baade and F. Zwicky, *Phys. Rev.* **46**, 76 (1934).

[7] J. Chadwick, *Nature* **129**, 312 (1932).

[8] E. M. Burbidge, G. R. Burbidge, W. A. Fowler, and F. Hoyle, *Rev. Mod. Phys.* **29**, 547 (1957).

[9] S. A. Colgate and R. H. White, *Astrophys. J.* **143**, 626 (1966).

[10] H.-T. Janka, *Supernovae und kosmische Gammablitze: Ursachen und Folgen von Sternexplosionen, ISBN 978-3-8274-2072-5. Spektrum Akademischer Verlag Heidelberg* (2017).

[11] A. S. Eddington, *The Observatory* **43**, 341 (1920).

[12] D. Branch and J. C. Wheeler, *Supernova Explosions, ISBN 978-3-662-55052-6. Springer-Verlag GmbH Germany* (2017).

[13] M. P. Fewell, *Am. J. Phys.* **63**, 653 (1995).

[14] F. Käppeler, R. Gallino, S. Bisterzo, and W. Aoki, *Rev. Mod. Phys.* **83**, 157 (2011).

[15] B. S. Meyer, *Annu. Rev. Astron. Astrophys.* **32**, 153 (1994).

[16] A. Arcones and F. K. Thielemann, *J. Phys. G Nucl. Part. Phys.* **40**, 013201 (2013).

[17] C. J. Horowitz, A. Arcones, B. Côté, *et al.*, *J. Phys. G Nucl. Part. Phys.* **46**, 083001 (2019).

[18] R. Barbon, F. Ciatti, and L. Rosino, *Astron. Astrophys.* **72**, 287 (1979).

[19] I. Tamborra, G. Raffelt, F. Hanke, H.-T. Janka, and B. Müller, *Phys. Rev. D* **90**, 045032 (2014).

[20] J. Powell, S. E. Gossan, J. Logue, and I. S. Heng, *Phys. Rev. D* **94**, 123012 (2016).

[21] M. Oertel, M. Hempel, T. Klähn, and S. Typel, *Rev. Mod. Phys.* **89**, 015007 (2017).

[22] W. D. Arnett, *Annu. Rev. Astron. Astrophys.* **11**, 73 (1973).

[23] K. Langanke and G. Martínez-Pinedo, *Rev. Mod. Phys.* **75**, 819 (2003).

[24] H. A. Bethe and J. R. Wilson, *Astrophys. J.* **295**, 14 (1985).

[25] H.-T. Janka, *Ann. Rev. Nucl. Part. Sci.* **62**, 407 (2012).

[26] H.-T. Janka, T. Melson, and A. Summa, *Ann. Rev. Nucl. Part. Sci.* **66**, 341 (2016).

[27] K. Kotake, T. Takiwaki, T. Fischer, K. Nakamura, and G. Martínez-Pinedo, *Astrophys. J.* **853**, 170 (2018).

[28] K.-C. Pan, C. Mattes, E. P. O'Connor, *et al.*, *J. Phys. G Nucl. Part. Phys.* **46**, 014001 (2019).

[29] H. Sawai and S. Yamada, *Astrophys. J. Lett.* **784**, L10 (2014).

[30] K. Fujisawa, H. Okawa, Y. Yamamoto, and S. Yamada, *Astrophys. J.* **872**, 155 (2019).

[31] S. M. Couch and C. D. Ott, *Astrophys. J.* **799**, 5 (2015).

[32] A. Wongwathanarat, H.-T. Janka, E. Müller, E. Pllumbi, and S. Wanajo, *Astrophys. J.* **842**, 13 (2017).

[33] K. Ebinger, S. Curtis, C. Fröhlich, *et al.*, *Astrophys. J.* **870**, 1 (2019).

[34] K. Ebinger, S. Curtis, S. Ghosh, *et al.*, *Astrophys. J.* **888**, 91 (2020).

[35] B. Müller, *Publ. Astron. Soc. Aust.* **33**, e048 (2016).

[36] A. W. Alsabti and P. Murdin, *Handbook of Supernovae, ISBN 978-3-319-21845-8. Springer International Publishing AG* (2017).

[37] S. E. Woosley, A. Heger, and T. A. Weaver, *Rev. Mod. Phys.* **74**, 1015 (2002).

[38] A. Wongwathanarat, E. Müller, and H.-T. Janka, *Astron. Astrophys.* **577**, A48 (2015).

[39] B. Müller, D. W. Gay, A. Heger, T. M. Tauris, and S. A. Sim, *Mon. Not. Roy. Astron. Soc.* **479**, 3675 (2018).

[40] A. Arcones, H.-T. Janka, and L. Scheck, *Astron. Astrophys.* **467**, 1227 (2007).

[41] B. Müller, *Mon. Not. Roy. Astron. Soc.* **453**, 287 (2015).

[42] S. Woosley and H.-T. Janka, *Nature Phys.* **1**, 147 (2005).

[43] H.-T. Janka, K. Langanke, A. Marek, G. Martínez-Pinedo, and B. Müller, *Phys. Rep.* **442**, 38 (2007).

[44] J. M. Blondin, A. Mezzacappa, and C. DeMarino, *Astrophys. J.* **584**, 971 (2003).

[45] L. Scheck, H.-T. Janka, T. Foglizzo, and K. Kifonidis, *Astron. Astrophys.* **477**, 931 (2008).

[46] H.-T. Janka, *Astrophys. J.* **837**, 84 (2017).

[47] R. C. Duncan, S. L. Shapiro, and I. Wasserman, *Astrophys. J.* **309**, 141 (1986).

[48] A. Burrows, J. Hayes, and B. A. Fryxell, *Astrophys. J.* **450**, 830 (1995).

[49] Y. Z. Qian and S. E. Woosley, *Astrophys. J.* **471**, 331 (1996).

[50] R. D. Hoffman, S. E. Woosley, and Y. Z. Qian, *Astrophys. J.* **482**, 951 (1997).

[51] T. A. Thompson, A. Burrows, and B. S. Meyer, *Astrophys. J.* **562**, 887 (2001).

[52] T. Fischer, S. C. Whitehouse, A. Mezzacappa, F. K. Thielemann, and M. Liebendörfer, *Astron. Astrophys.* **517**, A80 (2010).

[53] L. Hüdepohl, B. Müller, H.-T. Janka, A. Marek, and G. G. Raffelt, *Phys. Rev. Lett.* **104**, 251101 (2010).

[54] A. Arcones and H.-T. Janka, *Astron. Astrophys.* **526**, A160 (2011).

[55] K. Otsuki, H. Tagoshi, T. Kajino, and S.-y. Wanajo, *Astrophys. J.* **533**, 424 (2000).

[56] J. Bliss, M. Witt, A. Arcones, F. Montes, and J. Pereira, *Astrophys. J.* **855**, 135 (2018).

[57] Z. Xiong, M.-R. Wu, and Y.-Z. Qian, *Astrophys. J.* **880**, 81 (2019).

[58] E. O'Connor and C. D. Ott, *Astrophys. J.* **730**, 70 (2011).

[59] M. Ugliano, H.-T. Janka, A. Marek, and A. Arcones, *Astrophys. J.* **757**, 69 (2012).

[60] O. Pejcha and T. A. Thompson, *Astrophys. J.* **801**, 90 (2015).

[61] T. Ertl, H.-T. Janka, S. E. Woosley, T. Sukhbold, and M. Ugliano, *Astrophys. J.* **818**, 124 (2016).

[62] B. Müller, A. Heger, D. Liptai, and J. B. Cameron, *Mon. Not. Roy. Astron. Soc.* **460**, 742 (2016).

[63] D. Radice, A. Burrows, D. Vartanyan, M. A. Skinner, and J. C. Dolence, *Astrophys. J.* **850**, 43 (2017).

[64] R. Buras, M. Rampp, H.-T. Janka, and K. Kifonidis, *Phys. Rev. Lett.* **90**, 241101 (2003).

[65] S. E. Woosley and T. A. Weaver, *Astrophys. J., Suppl. Ser.* **101**, 181 (1995).

[66] F.-K. Thielemann, K. Nomoto, and M.-A. Hashimoto, *Astrophys. J.* **460**, 408 (1996).

[67] S. Nagataki, T. M. Shimizu, and K. Sato, *Astrophys. J.* **495**, 413 (1998).

[68] A. Perego, M. Hempel, C. Fröhlich, *et al.*, *Astrophys. J.* **806**, 275 (2015).

[69] S. Curtis, K. Ebinger, C. Fröhlich, *et al.*, *Astrophys. J.* **870**, 2 (2019).

[70] E. O'Connor and C. D. Ott, *Class. Quantum Gravity* **27**, 114103 (2010).

[71] S. M. Couch and E. O'Connor, *Astrophys. J.* **785**, 123 (2014).

[72] B. Fryxell, K. Olson, P. Ricker, *et al.*, *Astrophys. J., Suppl. Ser.* **131**, 273 (2000).

[73] A. Dubey, L. B. Reid, K. Weide, *et al.*, *Parallel Computing* **35**, 512 (2009).

[74] J. Larsson, C. Fransson, G. Östlin, *et al.*, *Nature* **474**, 484 (2011).

[75] P. MacNeice, K. M. Olson, C. Mobarry, R. de Fainchtein, and C. Packer, *Comput. Phys. Commun.* **126**, 330 (2000).

[76] A. Burrows, D. Radice, and D. Vartanyan, *Mon. Not. Roy. Astron. Soc.* **485**, 3153 (2019).

[77] B. Müller, T. M. Tauris, A. Heger, *et al.*, *Mon. Not. Roy. Astron. Soc.* **484**, 3307 (2019).

[78] H. Nagakura, A. Burrows, D. Radice, and D. Vartanyan, *Mon. Not. Roy. Astron. Soc.* **490**, 4622 (2019).

[79] H. Yasin, S. Schäfer, A. Arcones, and A. Schwenk, *Phys. Rev. Lett.* **124**, 092701 (2020).

[80] A. S. Schneider, L. F. Roberts, C. D. Ott, and E. O'Connor, *Phys. Rev. C* **100**, 055802 (2019).

[81] T. Melson, H.-T. Janka, R. Bollig, *et al.*, *Astrophys. J. Lett.* **808**, L42 (2015).

[82] C. J. Stapleford, C. Fröhlich, and J. P. Kneller, arXiv:1910.04172 (2019).

[83] S. M. Couch, E. Chatzopoulos, W. D. Arnett, and F. X. Timmes, *Astrophys. J. Lett.* **808**, L21 (2015).

[84] B. Müller, M. Viallet, A. Heger, and H.-T. Janka, *Astrophys. J.* **833**, 124 (2016).

[85] B. Müller, T. Melson, A. Heger, and H.-T. Janka, *Mon. Not. Roy. Astron. Soc.* **472**, 491 (2017).

[86] S. A. Colgate and M. H. Johnson, *Phys. Rev. Lett.* **5**, 235 (1960).

[87] W. D. Arnett, *Can. J. Phys.* **44**, 2553 (1966).

[88] W. Hillebrandt, in *Supernovae: A Survey of Current Research*, Nato Science Series C, Vol. 90, edited by M. Rees and R. Stoneham (1982) p. 123.

[89] Weinberg, D. H., *Radiative Gas Dynamics*, `http://www.astronomy.ohio-state.edu/~dhw/A825/notes2.pdf`, (Lecture notes, Ohio State University, 2007), accessed September 17, 2019.

[90] Ryden, B., *Radiative Gas Dynamics*, `http://www.astronomy.ohio-state.edu/~ryden/ast825/ch1-3.pdf`, (Lecture notes, Ohio State University, 2011), accessed September 17, 2019.

[91] Springel, V. and Dullemond, C. P., *Numerical Fluid Dynamics*, `http://www.ita.uni-heidelberg.de/~dullemond/lectures/num_fluid_2011/`, (Lecture notes, Ruprecht-Karls-Universität Heidelberg, 2011), accessed September 18, 2019.

[92] Käppeli, R. and Mishra, S., *Astron. Astrophys.* **587**, A94 (2016).

[93] M. Lieberman and A. Lichtenberg, *Principles of Plasma Discharges and Materials Processing, 2nd Edition, ISBN 0-471-72001-1. Wiley-VCH*, Vol. 30 (2003).

[94] L. Euler, *Mémoires de l'académie des sciences de Berlin* **11**, 274 (1757).

[95] E. Müller and M. Steinmetz, *Comput. Phys. Comm.* **89**, 45 (1995).

[96] S. M. Couch, C. Graziani, and N. Flocke, *Astrophys. J.* **778**, 181 (2013).

[97] S. Chandrasekhar, *Astrophys. J.* **74**, 81 (1931).

[98] A. W. Steiner, J. M. Lattimer, and E. F. Brown, *Eur. Phys. J. A* **52**, 18 (2016).

[99] F. X. Timmes and D. Arnett, *Astrophys. J., Suppl. Ser.* **125**, 277 (1999).

[100] F. X. Timmes and F. D. Swesty, *Astrophys. J., Suppl. Ser.* **126**, 501 (2000).

[101] K. Takahashi, M. F. El Eid, and W. Hillebrandt, *Astron. Astrophys.* **67**, 185 (1978).

[102] J. M. Lattimer and D. F. Swesty, *Nucl. Phys. A* **535**, 331 (1991).

[103] H. Yasin, *Core-collapse supernovae and the equation of state*, Ph.D. thesis, Technische Universität Darmstadt (2018).

[104] M. Aker and Katrin Collaboration, *Phys. Rev. Lett.* **123**, 221802 (2019).

[105] R. A. Battye and A. Moss, *Phys. Rev. Lett.* **112** (2014).

[106] S. Vagnozzi, S. Dhawan, M. Gerbino, *et al.*, *Phys. Rev. D* **98** (2018).

[107] R. W. Lindquist, *Ann. Phys.* **37**, 487 (1966).

[108] E. O'Connor, *Astrophys. J., Suppl. Ser.* **219**, 24 (2015).

[109] H. Nagakura, W. Iwakami, S. Furusawa, *et al.*, *Astrophys. J.* **854**, 136 (2018).

[110] M. Liebendörfer, S. C. Whitehouse, and T. Fischer, *Astrophys. J.* **698**, 1174 (2009).

[111] M. Shibata, K. Kiuchi, Y. Sekiguchi, and Y. Suwa, *Prog. Theor. Phys.* **125**, 1255 (2011).

[112] C. Y. Cardall, E. Endeve, and A. Mezzacappa, *Phys. Rev. D* **87**, 103004 (2013).

[113] M. Obergaulinger, H.-T. Janka, and M. A. Aloy, *Mon. Not. Roy. Astron. Soc.* **445**, 3169 (2014).

[114] T. Kuroda, T. Takiwaki, and K. Kotake, *Astrophys. J., Suppl. Ser.* **222**, 20 (2016).

[115] R. Glas, O. Just, H.-T. Janka, and M. Obergaulinger, *Astrophys. J.* **873**, 45 (2019).

[116] A. Perego, R. M. Cabezón, and R. Käppeli, *Astrophys. J., Suppl. Ser.* **223**, 22 (2016).

[117] K. Kotake, S. Yamada, and K. Sato, *Astrophys. J.* **618**, 474 (2005).

[118] Y. Suwa, T. Takiwaki, K. Kotake, and K. Sato, *Astrophys. J. Lett.* **665**, L43 (2007).

[119] C. Winteler, *Light element production in the big bang and the synthesis of heavy elements in 3D MHD jets from core-collapse supernovae*, Ph.D. thesis, University of Basel (2011).

[120] S. M. Couch and C. D. Ott, *Astrophys. J. Lett.* **778**, L7 (2013).

[121] S. Rosswog, T. Piran, and E. Nakar, *Mon. Not. Roy. Astron. Soc.* **430**, 2585 (2013).

[122] L. Dessart, C. D. Ott, A. Burrows, S. Rosswog, and E. Livne, *Astrophys. J.* **690**, 1681 (2009).

[123] M. Ruffert, H.-T. Janka, and G. Schaefer, *Astron. Astrophys.* **311**, 532 (1996).

[124] S. Rosswog and M. Liebendörfer, *Mon. Not. Roy. Astron. Soc.* **342**, 673 (2003).

[125] M. Liebendörfer, *Astrophys. J.* **633**, 1042 (2005).

[126] J. M. LeBlanc and J. R. Wilson, *Astrophys. J.* **161**, 541 (1970).

[127] C. L. Fryer and A. Heger, *Astrophys. J.* **541**, 1033 (2000).

[128] T. A. Thompson, E. Quataert, and A. Burrows, *Astrophys. J.* **620**, 861 (2005).

[129] P. Mösta, S. Richers, C. D. Ott, *et al.*, *Astrophys. J. Lett.* **785**, L29 (2014).

[130] A. Summa, H.-T. Janka, T. Melson, and A. Marek, *Astrophys. J.* **852**, 28 (2018).

[131] T. Takiwaki, K. Kotake, and Y. Suwa, *Mon. Not. Roy. Astron. Soc.* **461**, L112 (2016).

[132] A. Heger, N. Langer, and S. E. Woosley, *Astrophys. J.* **528**, 368 (2000).

[133] C. A. Meakin and D. Arnett, *Astrophys. J.* **667**, 448 (2007).

[134] J. Fuller, M. Cantiello, D. Lecoanet, and E. Quataert, *Astrophys. J.* **810**, 101 (2015).

[135] P. Colella and P. R. Woodward, *J. Comput. Phys.* **54**, 174 (1984).

[136] K. Nakamura, T. Takiwaki, T. Kuroda, and K. Kotake, *Publ. Astron. Soc. Jpn.* **67**, 107 (2015).

[137] K.-C. Pan, M. Liebendörfer, M. Hempel, and F.-K. Thielemann, *Astrophys. J.* **817**, 72 (2016).

[138] R. Buras, H.-T. Janka, M. Rampp, and K. Kifonidis, *Astron. Astrophys.* **457**, 281 (2006).

[139] A. Marek and H.-T. Janka, *Astrophys. J.* **694**, 664 (2009).

[140] J. W. Murphy and A. Burrows, *Astrophys. J.* **688**, 1159 (2008).

[141] F. Hanke, B. Müller, A. Wongwathanarat, A. Marek, and H.-T. Janka, *Astrophys. J.* **770**, 66 (2013).

[142] Y. Suwa, S. Yamada, T. Takiwaki, and K. Kotake, *Astrophys. J.* **816**, 43 (2016).

[143] A. Summa, H.-T. Janka, F. Hanke, *et al.*, in *The Lives and Death-Throes of Massive Stars*, IAU Symposium, Vol. 329, edited by J. J. Eldridge, J. C. Bray, L. A. S. McClelland, and L. Xiao (2017) p. 449.

[144] C. D. Ott, L. F. Roberts, A. da Silva Schneider, *et al.*, *Astrophys. J. Lett.* **855**, L3 (2018).

[145] D. Vartanyan, A. Burrows, D. Radice, M. A. Skinner, and J. Dolence, *Mon. Not. Roy. Astron. Soc.* **477**, 3091 (2018).

[146] E. P. O'Connor and S. M. Couch, *Astrophys. J.* **854**, 63 (2018).

[147] S. E. Woosley and A. Heger, *Phys. Rep.* **442**, 269 (2007).

[148] S. W. Bruenn, A. Mezzacappa, W. R. Hix, *et al.*, *Astrophys. J. Lett.* **767**, L6 (2013).

[149] S. W. Bruenn, E. J. Lentz, W. R. Hix, *et al.*, *Astrophys. J.* **818**, 123 (2016).

[150] A. Summa, F. Hanke, H.-T. Janka, *et al.*, *Astrophys. J.* **825**, 6 (2016).

[151] E. Mueller and W. Hillebrandt, *Astron. Astrophys.* **103**, 358 (1981).

[152] T. A. Thompson, P. Chang, and E. Quataert, *Astrophys. J.* **611**, 380 (2004).

[153] A. Burrows, L. Dessart, E. Livne, C. D. Ott, and J. Murphy, *Astrophys. J.* **664**, 416 (2007).

[154] T. Takiwaki and K. Kotake, *Astrophys. J.* **743**, 30 (2011).

[155] A. Heger, S. E. Woosley, and H. C. Spruit, *Astrophys. J.* **626**, 350 (2005).

[156] C. D. Ott, A. Burrows, T. A. Thompson, E. Livne, and R. Walder, *Astrophys. J. Lett.* **164**, 130 (2006).

[157] L. Scheck, K. Kifonidis, H.-T. Janka, and E. Müller, *Astron. Astrophys.* **457**, 963 (2006).

[158] D. Vartanyan, A. Burrows, D. Radice, M. A. Skinner, and J. Dolence, *Mon. Not. Roy. Astron. Soc.* **482**, 351 (2019).

[159] M. Obergaulinger and M. Á. Aloy, *Mon. Not. Roy. Astron. Soc.* **469**, L43 (2017).

[160] M. Obergaulinger and M. Á. Aloy, *Mon. Not. Roy. Astron. Soc.* **492**, 4613 (2020).

[161] V. P. Utrobin, N. N. Chugai, and A. A. Andronova, *Astron. Astrophys.* **295**, 129 (1995).

[162] V. P. Utrobin, A. Wongwathanarat, H.-T. Janka, and E. Müller, *Astron. Astrophys.* **581**, A40 (2015).

[163] P. Virtanen, R. Gommers, T. E. Oliphant, *et al.*, *Nature Methods* **17**, 261 (2020).

[164] A. Dubey, C. Daley, J. ZuHone, *et al.*, *Astrophys. J., Suppl. Ser.* **201**, 27 (2012).

[165] J. A. Harris, W. R. Hix, M. A. Chertkow, *et al.*, *Astrophys. J.* **843**, 2 (2017).

[166] C. Travaglio, W. Hillebrandt, M. Reinecke, and F. K. Thielemann, *Astron. Astrophys.* **425**, 1029 (2004).

[167] N. Nishimura, T. Takiwaki, and F.-K. Thielemann, *Astrophys. J.* **810**, 109 (2015).

[168] S. E. Woosley, W. D. Arnett, and D. D. Clayton, *Astrophys. J., Suppl. Ser.* **26**, 231 (1973).

[169] M. Eichler, K. Nakamura, T. Takiwaki, *et al.*, *J. Phys. G Nucl. Part. Phys.* **45**, 014001 (2018).

[170] E. O'Connor and C. D. Ott, *Astrophys. J.* **762**, 126 (2013).

[171] B. Müller, H.-T. Janka, and A. Marek, *Astrophys. J.* **756**, 84 (2012).

[172] B. Müller and H.-T. Janka, *Mon. Not. Roy. Astron. Soc.* **448**, 2141 (2015).

Acknowledgements

Vielen Dank an all die Menschen, die mich auf dem Weg hierher unterstützt haben. Allen voran natürlich an Almudena Arcones, in deren Arbeitsgruppe ich sowohl meine Masterarbeit, als auch meine Dissertation verfassen durfte. Des Weiteren bedanke ich mich herzlich bei Martin Obergaulinger und Takami Kuroda für hilfreiche Kommentare zu früheren Versionen dieser Thesis. Besonderer Dank für wissenschaftliche (und weniger wissenschaftliche) Diskussionen geht an Hannah, Carlos, Max J., und Moritz. Die letzten Jahre werden mir immer in Erinnerung bleiben, und damit auch meine (Ex-)Kollegen Marius, Julia, Dirk, Albino, Federico, Jonas, Wida, Simon, und Gerard.

An meine ganze Familie geht ein Riesendank für die uneingeschränkte Unterstützung in den letzten Jahren. Nicht unerwähnt sollen auch all meine Freunde bleiben, die mich auch mal an andere Sachen neben der Astrophysik denken ließen. Insbesondere der Bardenbart-Bernd und die Jungs (und Mädels) von The Space Between... auf dass bald jeder Tag der Woche zum Samstag wird!

Diese Arbeit wurde durch den European Research Council Grant No. 677912 (EUROPIUM) und von der Deutschen Forschungsgemeinschaft durch den SFB 1245 (Projektnummer 279384907) unterstützt. Die Berechnungen für diese Arbeit wurden auf dem Lichtenberg-Hochleistungsrechner der TU Darmstadt (Projekt-IDs: 172, 267, 350, 646, 723, 952, 996, 1043) durchgeführt.

Curriculum Vitae

Maximilian Rudolf Witt

10.05.1992	Born in Regensburg
2011	Abitur in Wiesbaden
2011 - 2014	Bachelor studies, TU Darmstadt
2014	Bachelor's degree, thesis title: "Untersuchungen zu Neutronensternen mit einfach parametrisierten Zustandsgleichungen", Adviser: M. Buballa
2014 - 2016	Master studies, TU Darmstadt
2016	Master's degree, thesis title: "The neutrino-driven wind: From steady-state models to hydrodynamic simulations", Adviser: A. Arcones
2016 - 2020	Doctoral studies, TU Darmstadt

Erklärungen laut Promotionsordnung

§8 Abs. 1 lit. c PromO

Ich versichere hiermit, dass die elektronische Version meiner Dissertation mit der schriftlichen Version übereinstimmt.

§8 Abs. 1 lit. d PromO

Ich versichere hiermit, dass zu einem vorherigen Zeitpunkt noch keine Promotion versucht wurde. In diesem Fall sind nähere Angaben über Zeitpunkt, Hochschule, Dissertationsthema und Ergebnis dieses Versuchs mitzuteilen.

§9 Abs. 1 PromO

Ich versichere hiermit, dass die vorliegende Dissertation selbstständig und nur unter Verwendung der angegebenen Quellen verfasst wurde.

§9 Abs. 2 PromO

Die Arbeit hat bisher noch nicht zu Prüfungszwecken gedient.

Darmstadt, den 08.04.2020

Maximilian Rudolf Witt